



### 저작자표시-비영리-변경금지 2.0 대한민국

이용자는 아래의 조건을 따르는 경우에 한하여 자유롭게

- 이 저작물을 복제, 배포, 전송, 전시, 공연 및 방송할 수 있습니다.

다음과 같은 조건을 따라야 합니다:



저작자표시. 귀하는 원 저작자를 표시하여야 합니다.



비영리. 귀하는 이 저작물을 영리 목적으로 이용할 수 없습니다.



변경금지. 귀하는 이 저작물을 개작, 변형 또는 가공할 수 없습니다.

- 귀하는, 이 저작물의 재이용이나 배포의 경우, 이 저작물에 적용된 이용허락조건을 명확하게 나타내어야 합니다.
- 저작권자로부터 별도의 허가를 받으면 이러한 조건들은 적용되지 않습니다.

저작권법에 따른 이용자의 권리와 책임은 위의 내용에 의하여 영향을 받지 않습니다.

이것은 [이용허락규약\(Legal Code\)](#)을 이해하기 쉽게 요약한 것입니다.

[Disclaimer](#)



Ph.D. DISSERTATION

Theoretical study on  
supercontinuum generation and  
pulse dynamics in gain-embedded  
nonlinear optical media

광학적 이득이 포함된 비선형 광학적 매질에서의  
초연속체 생성 및 펄스 역학에 관한 이론적 연구

By  
KYOUNG YOON PARK

FEBRUARY 2020

DEPARTMENT OF ELECTRICAL AND  
COMPUTER ENGINEERING  
COLLEGE OF ENGINEERING  
SEOUL NATIONAL UNIVERSITY

# Theoretical study on supercontinuum generation and pulse dynamics in gain– embedded nonlinear optical media

# 광학적 이득이 포함된 비선형 광학적 매질에서의 초연속체 생성 및 펠스 역학에 관한 이론적 연구

지도 교수      정 윤 찬

이 논문을 공학박사 학위논문으로 제출함  
2020년 2월

서울대학교 대학원  
전기정보공학부  
박 경 윤

박경윤의 공학박사 학위 논문을 인준함  
2020년 2월

위 원 장 \_\_\_\_\_ (인)  
부위원장 \_\_\_\_\_ (인)  
위 원 \_\_\_\_\_ (인)  
위 원 \_\_\_\_\_ (인)  
위 원 \_\_\_\_\_ (인)

# Abstract

## Theoretical study on supercontinuum generation and pulse dynamics in gain-embedded nonlinear optical media

KYOUNGYOON PARK  
DEPARTMENT OF ELECTRICAL AND  
COMPUTER ENGINEERING  
COLLEGE OF ENGINEERING  
SEOUL NATIONAL UNIVERSITY

In this dissertation, supercontinuum generation (SCG) and related soliton dynamics in gain-embedded highly nonlinear photonic crystal fibers (HNL-PCFs) are numerically and theoretically analyzed in anomalous dispersion (AD) and flattened all-normal dispersion (FAND).

The first part of the dissertation introduces the fundamental of fiber optics, fiber lasers, and nonlinear fiber optics. Based on the background knowledge on fiber optics, fiber lasers, and nonlinear fiber optics, the fundamental principle of SCG is briefly overviewed, which is a key basis for this dissertation.

Then, a numerical model of dynamics of ultrafast pulses under dispersive, nonlinear, and optical gain effects. First, the well-

known numerical model on evolution of ultrafast pulses in HNL–PCFs, nonlinear Schrödinger equation (NLSE), is discussed. Moreover, optical bright solitons (BSs) and dark solitons (DSs), the key elements of the SCG, are introduced briefly. Then, a numerical model of optical gain effects on sub–fs ultrafast pulses is suggested. Especially, a semi–classical numerical model based on the generalized complex Ginzburg–Landau equation (GCGLE) is suggested in order to take account of ultrafast interactions between gain ions and ultrafast solitons.

Based on the GCGLE, SCG in a rare–earth doped HNL–PCF with AD in the sub–ps pulse regime is numerically investigated. The SCG characteristics of an active HNL–PCF is compared with a passive–type counterpart, unveiling novel optical gain effects. Moreover, gain–induced soliton dynamics, such as soliton–cascade–like behaviors, soliton–quasi–soliton collisions, and phase–matched dispersive wave generation, is rigorously analyzed, which eventually contributes to enhancement of energy scaling of SC radiation without incurring considerable degradation of its spectral flatness.

As a counterpart of SCG in a rare–earth doped HNL–PCF with AD, SCG in a rare–earth doped HNL–PCF with FAND in the sub–picosecond pulse regime is also numerically investigated. In particular, spontaneous generation of DSs in FAND regime and its physical mechanism of the DS generation is discussed. By the combined effect of the optical gain and Raman scattering, Raman–

induced oscillatory structure (RIOS) is emitted at the outermost blue-shifted SPM peak, and it develops dark solitons under the optical gain effect. The emitted dark solitons significantly affect SCG characteristics such as spectral bandwidth and shot-to-shot coherence. Consequently, it is proven that the utilization of active fibers for SCG yields bandwidth- or coherence-controllable SCG system.

Therefore, this study suggests the possibility of further improvement of SCG by exploiting the novel active-type HNL-PCFs, which is all-in-one structure of a passive-type HNL-PCF and a rare-earth doped fiber. Furthermore, soliton dynamics related to SCG in active HNL-PCFs is drastically different to the conventional soliton dynamics of SCG in passive fibers. The reason is that in active HNL-PCFs, the soliton dynamics correlated with SCG is actually the soliton dynamics in open systems where external energy inflows are present. The energy inflow causes various soliton dynamics, which have not been observed in soliton dynamics in a closed system. For example, soliton clusters, collisions of a soliton and a quasi-soliton, spontaneous and eruptive generation of DSs, and DS-based coherence collapse. Such novel soliton dynamics in an open system will open up new possibilities for extended power-scaling, controlled spectral broadening and shot-to-shot coherence of SCG.

**Keyword :** Fiber laser, Nonlinear fiber optics, Optical soliton,

Supercontinuum, Ultrafast optics, Quantum optics

**Student Number :** 2013–20789

# Table of contents

Abstract .....	i
List of Figures .....	iii
List of Tables .....	x
Nameclature .....	xi
1. Introduction .....	1
1.1 Fiber optics .....	1
1.2 Fiber laser .....	9
1.3 Nonlinear fiber optics .....	13
1.4 Supercontinuum generation .....	14
1.5 Motivation .....	17
1.6 Scope of the study .....	21
2. Numerical model of ultrafast optics active and nonlinear media .....	22
2.1 Numerical model of ultrafast optics .....	22
2.2 Semiclassical model of light–matter interactions ....	30
2.3 Gain saturation effect by an ultrafast pulse train ....	44
3. Superconitnuum generation and bright soliton dynamics in gain–embedded highly nonlinear photonic crystal fibers with anomalous dispersion .....	50
3.1 Background of the study .....	50
3.2 Numerical model and methods .....	54

3.3 Gain effects and soliton dynamics on SCG in the AD regime.....	61
3.4 Comparative analysis of energy-scaling scheme for SCG .....	72
3.5 Direct amplification of SC radiation.....	76
4. Superconitnuum generation and dark soliton dynamics in gain embedded highly nonlinear photonic crystal fibers with flattend all-normal dispersion.....	79
4.1 Background of the study.....	79
4.2 Numerical model.....	84
4.3 Review of SCG in active FAND-PCFs in low gain regime.....	87
4.4 Eruptive generation of Dss on SCG in active FAND-PCFs .....	91
4.5 Raman-induced oscillatory structure .....	100
4.6 DS dynamics and its impact on SCG in active FAND-PCFs .....	109
5. Concluding remarks .....	120
Appendix A. Derivation of Maxwell-Bloch equation in two-level and the saturation energy .....	125
Bibliography .....	131
Abstract in Korean.....	141

# List of Figures

Fig. 1.1.1. Attenuation spectrum of typical silica fibers .....	3
Fig. 1.1.2. Transverse mode profiles that multi-mode fibers can support.....	4
Fig. 1.1.3. A typical example of GVD profile of optical fiber... .....	7
Fig. 1.1.4 (a) SEM micrographs of a PCF, (b) Graphics of a PCF with a index profile .....	9
Fig. 1.2.1 Schematic diagram of a fiber amplifier made using rare-earth doped fibers .....	11
Fig. 1.2.2 Wavelength range of fiber laser according to the type of rare-earth ion .....	12
Fig. 1.4.1 Scheme of SCG via highly nonlinear PCF .....	15
Fig. 1.4.2. SCG via highly nonlinear PCF .....	16
Fig. 1.5.1. Concpet of the amplification system of brandband SC radiations .....	17
Fig. 1.5.2. Concpet of the amplification system of brandband SC radiations: (a) SCG system without any amplifier stages and its output spectrum as a reference, (b) SCG system with an ampflier stage after the HNL-PCF and output spectrum,	

(c) SCG system with a pre-amplifier stage before the HNL-PCF and its output spectrum, (d) SCG system made of an active HNL-PCF which is an all-in-one system of the HNL-PCF and the fiber amplifier, and the resultant output spectrum	19
.....	
Fig. 2.1.1. Temporal variation of SPM-induced phase shift and frequency chirp for Gaussian (dashed curve) and super-Gaussian (solid curve) pulses .....	26
Fig. 2.1.2. (a) Raman gain spectrum and (b) phase response obtained by Eq. (2.1.9) .....	27
Fig. 2.1.3. Three dimensional visualization of propagation of (a) BS and (b) DS. Intensity profile of (c) BS and (d) DS. Phase profile of (e) BS and (d) DS. From this figure, one can find that BS is symmetric, whereas DS is anti-symmetric.....	
.....	29
Fig. 2.2.1. (a) State diagram of two states in classical physics, (b) State diagram of two states in quantum physics called as Bloch vector representation .....	30
Fig. 2.2.2. Electric field induces microscopic dipole moment according to the laws of quantum mechanics. These moments are then summed to yield the macroscopic polarization of the medium, which acts as a source in Maxwell's equations. The condition of self-consistency then requires that the assume field equal to the reaction field .....	33
Fig. 2.2.3. Interaction of multiple pulses with the fixed repetition rate and atoms where quantum coherence is negligible, and the condition of gain saturation.....	36

Fig. 2.2.4. Er <sup>3+</sup> energy level.....	38
Fig. 2.2.5. Yb <sup>3+</sup> energy level .....	41
Fig. 2.2.6. A pulse train with a fixed repetition rate.....	45
Fig. 2.2.7. Change of the population inversion during amplification of supercontinuum pulse and validity of Eq. (2.3.14) .....	49
Fig. 3.2.1. Conceptual schematic of SCG in an Yb-doped active HNL-PCF. LD: Laser diode, OSA: Optical spectrum analyzer. ....	55
Fig. 3.3.1. Evolutions of SC radiation in passive and active HNL-PCFs. (a) and (b): Spectral evolutions in the passive HNL-PCF ( $g_{us} = 0$ dB/m) and in the active HNL-PCF ( $g_{us} = 40$ dB/m), respectively. (c) and (d): Temporal evolutions in the passive case and in the active case, respectively. (e) and (f): Evolutions of 20-dB BW and AESD in the passive case and in the active case, respectively. Note that the output spectra and temporal traces are put on top of the figures of (a)-(d), respectively. ....	64
Fig. 3.3.2. Detailed soliton formation and dynamics in the active HNL-PCF. (a) Zoomed-in image of the part enclosed by the rectangle in a white-dashed line in Fig. 2(e). (b) Formation of solitons and QSs, and their collision dynamics. The inset is the zoomed-in image of the part enclosed by the rectangle in a white-solid line in (b). (c) Spectrograms and the linear-scale intensity profiles corresponding to Stage I, Stage II, and Stage III. S: Soliton; QS: Quasi-soliton. (d)	

Dispersion relations of the corresponding soliton, QS, and the HNL–PCF ..... 68

Fig. 3.3.3. Output spectrograms for the passive and active HNL–PCFs. (a) Passive HNL–PCF case ( $g_{us} = 0$  dB/m). (b) Active HNL–PCF case ( $g_{us} = 40$  dB/m) ..... 71

Fig. 3.4.1. Characteristics of the passive HNL–PCF case combined with initially energy–boosted input and the active HNL–PCF case. (a) and (b): Spectral evolutions in the passive HNL–PCF case with initially energy–boosted input and in the active HNL–PCF case, respectively. (c) and (d): Evolutions of 20–dB BW (blue) and AESD (red) in the passive HNL–PCF case with initially energy–boosted input and in the active HNL–PCF case. (e) and (f): Total numbers of solitons generated in the passive HNL–PCF case with initially energy–boosted input and in the active HNL–PCF case, respectively. ..... 74

Fig. 3.5.1. Characteristics of the passive HNL–PCF case combined with a conventional amplifier based on a low–nonlinearity YDF and the active HNL–PCF case. (a) and (b): Spectral evolutions in the passive HNL–PCF case combined with a conventional amplifier based on a low–nonlinearity YDF and in the active HNL–PCF, respectively. (c) and (d): Evolutions of 20–dB BW (blue) and SFM (red) within the 20–dB BW in the passive HNL–PCF case combined with a conventional amplifier based on a low–nonlinearity YDF and in the active HNL–PCF, respectively ..... 78

Fig. 4.3.1. spectral evolution of a 1–nJ input pulse through the HNL–PCF with (a) zero–gain or (b) 20–dB/m gain ( $L$ : length

of the HNL-PCF). Lower: 20-dB BW (blue) and AESD (green) of the signal pulse with respect to the fiber length for (c) zero-gain or (d) 20-dB/m gain..... 88

Fig. 4.3.2. Temporal evolution of a 1-nJ input pulse through the HNL-PCF with (a) zero-gain or (b) 20-dB/m gain. FWHM width (blue) and peak power (green) of the signal pulse with respect to the fiber length for (c) zero-gain or (d) 20-dB/m gain..... 89

Fig. 4.3.4. Upper: spectral evolution of a 1-nJ SC input pulse through (a) the YDF of 1.9 m or (b) the active HNL-PCF of 3.4 m. Lower: 20-dB BW (blue) and SFM (green) of the signal pulse with respect to the fiber length for (c) the YDF PCF of 1.9 m or (d) the active HNL-PCF of 3.4 m..... 90

Fig. 4.4.1. Spectral and temporal evolution of SCG seeded by a 1.0-nJ sub-ps pulse with four different gain coefficients: 0-dB/m for (a) and (b), 10-dB/m for (c) and (d), 20-dB/m for (e) and (f), and 30-dB/m for (g) and (h). ..... 95

Fig. 4.4.2 Dark pulses atop the SC pulse with 30-dB/m gain coefficient, which are zoomed-in pictures of Fig. 1(h). (a) Dark pulses in a range of 0.35 ~ 0.39 ps, (b) Dark pulses in a range of 2.11 ~ 2.15 ps. (c) Curve fitting of the white-circled dark pulse in (a) with a  $\tanh^2$  curve and its phase profile, (d) Curve fitting of the white-circled dark pulse in (b) with a  $\tanh^2$  curve and its phase profile ..... 96

Fig. 4.4.3. Output temporal intensity profile for four cases: (a) output temporal intensity profiles of Case I (with 0-dB/m gain coefficient and without IRS) and Case III (with 0-dB/m gain coefficient and with IRS), (b) output temporal intensity

profiles of Case II (with 30-dB/m gain coefficient and without IRS) and Case IV (with 30-dB/m gain coefficient and with IRS). Temporal evolution of SC pulses for four cases: (c) Case I, (d) Case II, (e) Case III, and (f) Case IV.....	98
Fig. 4.4.4. (a) Temporal intensity profiles and (b) corresponding spectra of Case II and IV for a given distance.	101
Fig. 4.5.1. Two dynamics regime in FWM-SRS coupled dynamics: (a) SRS-dominant regime and (b) FWM-dominant regime. (c) continuous energy transfer belonging to both (a) or (b). Stokes and anti-Stokes power with respect to the distance when (d) $P_p = 47$ W and $g_0 = 0$ dB/m, (f) $P_p = 47$ W and $g_0 = 4$ dB/m, (h) $P_p = 4700$ W and $g_0 = 0$ dB/m, and (j) $P_p = 4700$ W and $g_0 = 4$ dB/m. (e)-(k) are phase evolutions corresponding to (d)-(j), respectively. ....	107
Fig. 4.5.2. Evolution of (a) 20-dB BW and (b) peak power of the SC pulse for four cases .....	108
Fig. 4.5.3. (a) DS generation by RIOS in a cascading way. (b) Repulsive collision of DSs. A: Collision of two DSs, B: Collision of multiple DSs .....	109
Fig. 4.6.1. Spectrograms of SC lights in an active FAND-PCF with 30-dB/m gain with respect to four different distances: (a) 1.0 m (State I), (b) 1.3 m (State II), (c) 1.5 m (State III), and (d) 2.2 m (State IV).....	113
Fig. 4.6.2. Output spectrograms for (a) Case II and (b) IV....	114
Fig. 4.6.3. (a) Temporal evolution of SCG with 20-dB/m gain coefficient and one-photon-per-mode noise. (b) Normalized	

autocorrelation traces for the input and two output pulses: passive and active FAND–PCFs .....	116
---	-----

Fig. 4.6.4. (a) Spectrally averaged coherence value, (b) 20– dB BW, and AESD of SC pulses generated via an active FAND–PCF with respect to gain coefficient. (c) Output coherence spectra and (d) ensemble–averaged output spectral intensities corresponding to (a) and (b), respectively.	118
---	-----

Fig. 4.6.5. (a) Spectrally averaged coherence value, (b) 20– dB BW, and (c) AESD of SC pulses generated via an active FAND–PCF for various fiber lengths and gain coefficients....	119
--	-----

# List of Tables

Table 3.2.1. Simulation parameters..... 60

Table 4.2.1. Simulation parameters..... 87

# Nomenclature

## Acronyms / Abbreviations

AD	Anomalous dispersion
AESD	Averaged energy spectral density
BS	Bright soliton
BW	Bandwidth
CW	Continuous wave
DS	Dark soliton
DW	Dispersive wave
FAND	Flattened all-normal dispersion
FWM	Four-wave mixing
GCGLE	Generalized complex Ginzburg–Landau equation
GVD	Group velocity dispersion
HNL	Highly–nonlinear
IRS	Intrapulse Raman scattering
IST	Inverse scattering transform
KdVBE	Korteweg–deVries–Burgers equation
MBE	Maxwell–Bloch equation
ND	Normal dispersion
NLSE	Nonlinear Schrödinger equation
OWB	Optical wave breaking
PCF	Photonic crystal fiber

QS	Quasi-soliton
RIOS	Raman-induced oscillatory structure
RISW	Roman-induced shock wave
RSSFS	Raman soliton self-frequency shift
SC	Supercontinuum
SCG	Supercontinuum generation
SFM	Spectral flatness measurement
SPM	Self-phase modulation
SRS	Stimulated Raman scattering
XPM	Cross-phase modulation
YDF	Ytterbium-doped fiber
ZDW	Zero-dispersion wavelength

# Chapter 1

## Introduction

### 1.1. Fiber optics

#### 1.1.1. Overview on fiber optics

Optical fiber is a transparent cylindrical dielectric waveguide, consisting of a high index core and a low index cladding [1, 2]. Light waves entering the optical fiber are guided by the principle of total internal reflection caused by the index difference between the core and cladding [1]. The waveguide structure using total reflection in silica was proposed in 1960, but the optical loss in the initial optical fiber was very lossy to over 1000 dB/km [2]. However, after continuous technical advances, silica-based optical fibers with low losses of 0.2 dB/km in the 1550-nm wavelength band were developed in 1979, which led to a major breakthrough in optical communications [3]. In addition, low loss silica fibers have enabled waveguides of high-power lasers as well as optical communications, creating the field of nonlinear fiber optics [1, 4]. In 1972, the results of Raman scattering and Brillouin scattering,

which are representative phonon–photon interactions, could be observed in optical fibers [5, 6]. Moreover, optical bright soliton (BS) and dark soliton (DS) were theoretically predicted by Hasegawa and Tappert [7] and experimentally observed in 1980 [8]. In addition, various nonlinear optical phenomena have been studied, including self–phase modulation (SFM), four–wave mixing (FWM), and optical parametric amplification (OPA) in optical fibers [1]. In particular, nonlinear optical phenomena easily occur when high–peak power pulses are launched through optical fibers, so that various pulse light sources exploiting nonlinear phenomena have been studied. Representative examples include mode–locked soliton laser [9], dissipative soliton laser [10], Kerr cavity soliton [11], supercontinuum (SC) generation (SCG) [12], etc. Among them, SCG, the main topic of this paper, is a phenomenon in which various kinds of nonlinear optical effects such as optical soliton, Raman scattering, SFM, and FWM simultaneously occur and interact each other, thereby generating optical spectrum extends up to several hundred or thousand nanometers [12]. Such ultra–wideband light sources can be applied to various research fields, including optical communication, optical sensors, and optical imaging. The emergence of optical fibers has caused remarkable advances in laser optics, not only in optical communication, but also in the generation of various light sources exploiting nonlinear optical effects.

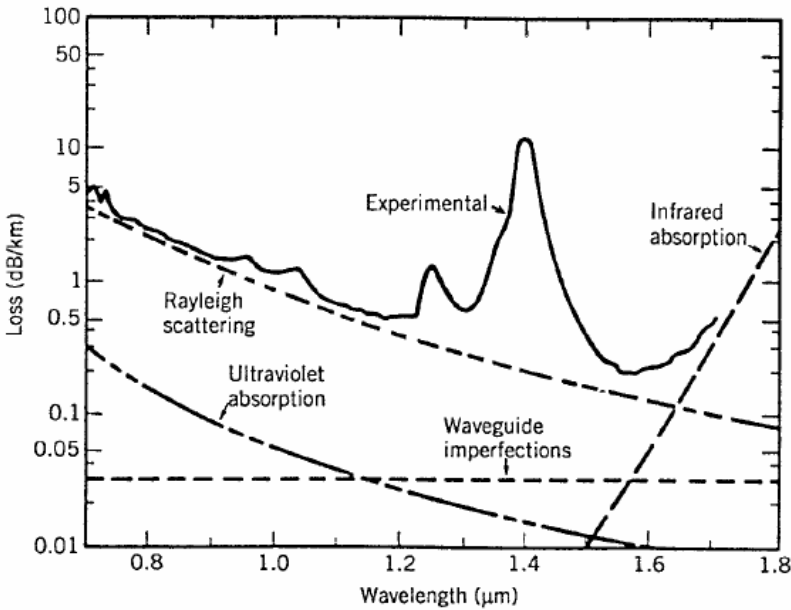


Fig. 1.1.1. Attenuation spectrum of typical silica fibers (Ref. [13])

### 1.1.2. Fiber mode

In this dissertation, I will deal with nonlinear optics based on optical fiber, so I will discuss basic properties of optical fiber. In general, a fiber in which the constant core index and the constant cladding index are clearly distinguished is called a step-index fiber, which is currently widely used in optical communication or fiber laser research [14]. This step-index fiber supports a transverse mode due to the boundary condition of the core and cladding [14]. The number of modes that an optical fiber can support depends on the  $V$ -number, and the  $V$ -number is calculated as follows.

$$V = k_0 a \left( n_{core}^2 - n_{clad}^2 \right)^{1/2} \quad (1.1.1)$$

where  $k_0 = 2\pi/\lambda$ ,  $a$  is the core radius, and  $\lambda$  is the wavelength of light.

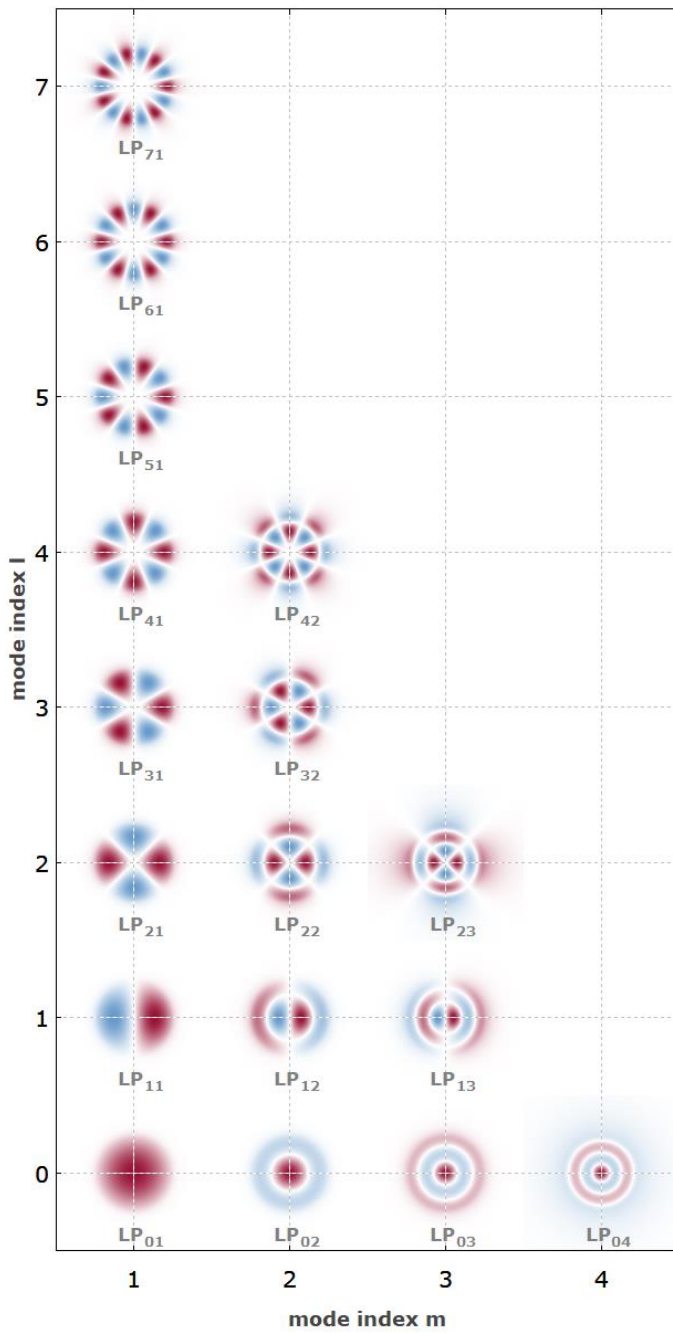


Fig. 1.1.2. Transverse mode profiles that multi-mode fibers can support (Ref. [15])

If  $V < 2.405$ , the step-index fiber supports single mode, and  $V > 2.405$  supports multi modes. The transverse intensity profile and effective propagation constant of the mode that a step-index fiber can be calculated by solving eigenvalue equations which is derived by applying boundary conditions to the Maxwell equations (See Ref. [14] for details of the calculation). Figure 1.1.2 shows the transverse intensity profiles of different modes of multi-mode fibers. In this paper, single mode condition (i.e.  $V < 2.405$ ) is assumed unless otherwise specified.

### 1.1.3. Fiber dispersion

When light is guided in a dielectric medium such as a silica fiber, the light interacts with bound electrons of the dielectric medium. Bound electrons can be assumed to be trapped by harmonic potentials generated by atoms, which can be used to model the interaction of light with bound electrons [16]. Since light acts as the driving force of bound electrons, the response of bound electrons varies with frequency of the light and has a resonance when the frequency of the light matches the resonant frequency of the bound electrons [17]. As a result, the susceptibility and refractive index change depending on the frequency of light, which is called as material dispersion, and usually described by the Drude–Lorentz model. According to the Drude–Lorentz model, the refractive index is approximated by the following equation.

$$n^2(\omega) = 1 + \sum_{k=1} \frac{B_k \omega_k^2}{\omega_k^2 - \omega^2}. \quad (1.1.2)$$

This equation is called the Sellmeier equation, which is mainly used to characterize the dispersion characteristics of optical fibers [1, 14, 16–18].

The derivative of refractive index with respect to frequency causes the propagation speed of the light to be guided in the optical fiber to vary with frequency. Therefore, the dispersion characteristics have significant influences on the propagation of non-monochromatic waves or multi-monochromatic waves in optical fibers. In general, dispersion in an optical fiber is expressed by a propagation constant, which is

$$\begin{aligned} \beta(\omega) &= n(\omega) \frac{\omega}{c} = \beta_0 + \beta_1 (\omega - \omega_0) + \frac{1}{2} \beta_2 (\omega - \omega_0)^2 + \dots \\ &= \sum_k \frac{\beta_k}{k!} (\omega - \omega_0)^k \end{aligned}, \quad (1.1.3)$$

where

$$\beta_k = \left. \frac{d^k \beta}{d\omega^k} \right|_{\omega=\omega_0} \quad (k = 0, 1, 2, \dots). \quad (1.1.4)$$

Each Taylor series of propagation constants has a different physical meaning.  $\beta_0$  is the propagation constant at the center frequency,  $\beta_1$  is the group index for a given frequency, and  $\beta_2$  is the change in group index with frequency (i.e. group velocity dispersion (GVD)), which are expressed as following [1]:

$$\beta_0 = \frac{n(\omega_0) \omega_0}{c}, \quad (1.1.5)$$

$$\beta_1 = \frac{n_g}{c} = \frac{1}{c} \left( n + \omega \frac{dn}{d\omega} \right), \quad (1.1.6)$$

$$\beta_2 = \frac{1}{c} \frac{dn_g}{d\omega}. \quad (1.1.6)$$

Figure 1.1.3 shows changes of  $\beta_2$  with respect to wavelength. In Fig. 1.1.3, one can see that there is a zero-dispersion wavelength (ZDW) in which  $\beta_2 = 0$ . Wavelengths lower than the ZDW have positive  $\beta_2$  values, which we say are in the normal dispersion (ND) region. Wavelengths higher than the ZDW have negative  $\beta_2$  values, which we say are in the anomalous dispersion (AD) region. In the ND region, the group index at the red wavelength is smaller than the group index at the blue wavelength, so the group velocity at the red wavelength is faster than the group velocity at the blue wavelength. On the other hand, in the AD region, exactly as opposed to the ND region, the group velocity at blue wavelength is faster than the group velocity at red wavelength. Although GVD is highly influenced by material dispersion, it is also affected by mode dispersion, so it is possible to control GVD to obtain desired GVD characteristics through fiber index engineering [1, 18].

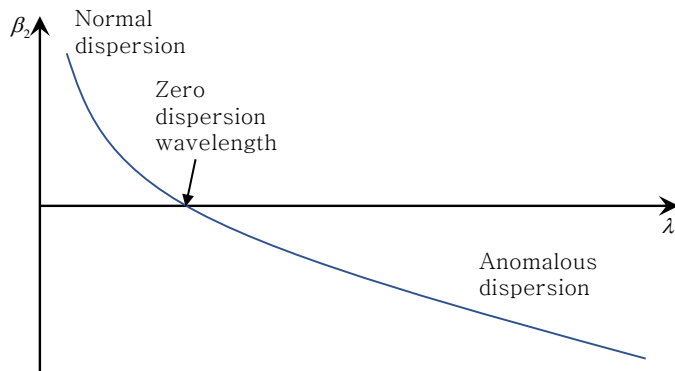


Fig. 1.1.3. A typical example of GVD profile of optical fiber

#### 1.1.4. Various types of optical fiber

In addition to the step index fiber, various optical fibers have been developed for various fiber-optic applications. For example, graded index optical fibers have been developed for reducing modal dispersion [19], dispersion-engineered dispersion shifted or compensated fibers have been implemented to obtain a desired GVD characteristics at a given wavelength range [20], large mode area fibers [15] and anti-resonant fibers [21] have extensively exploited for high-power fiber laser applications, and photonic crystal fibers (PCFs), in which light is guided by the photonic crystal structure, have attracted researchers' attentions in virtue of its unique waveguide properties [12]. PCF is divided into photonic-bandgap fiber where light is guided in bandgap due to photonic crystal structure, holey fiber guiding along hole, and hole-assisted fiber guiding to core by surrounding hole [18].

These fibers have been used for various purposes, depending on their dispersion and nonlinear properties. Low-linearity anti-resonant fibers, photonic bandgap fibers, and large mode area fibers can be used to deliver high-powered fiber lasers, and hole-assisted PCFs with high nonlinearity due to narrow core areas can convert wavelengths using nonlinearities.

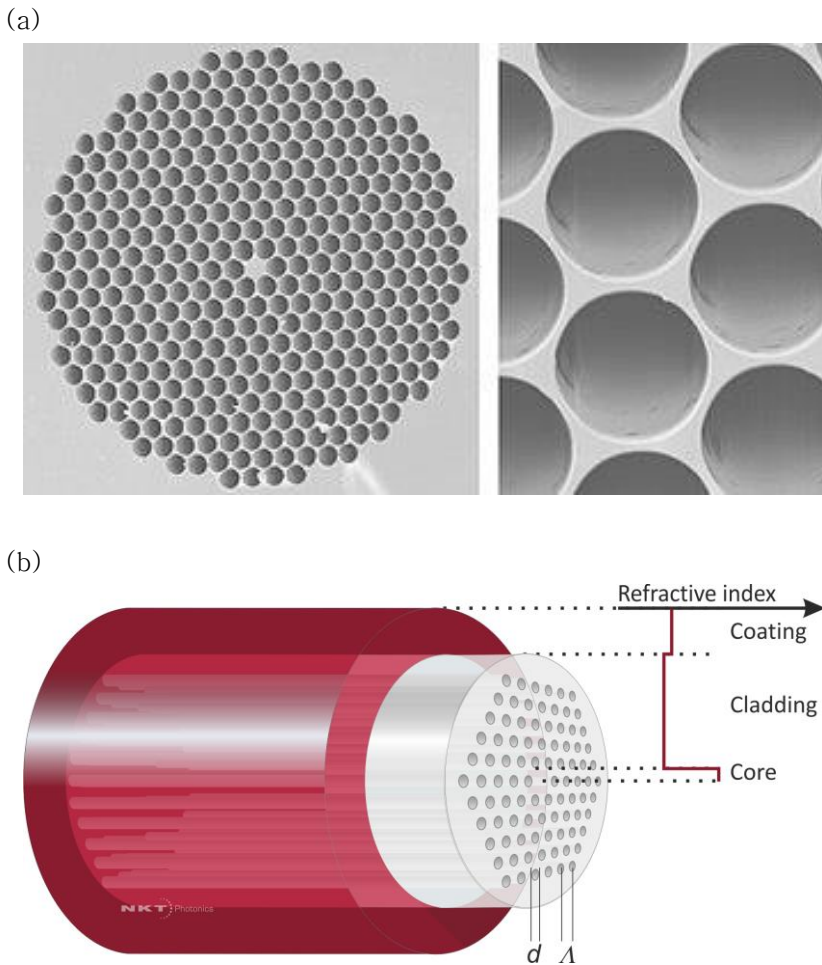


Fig. 1.1.4 (a) SEM micrographs of a PCF in Ref. [22, 23], (b) Graphics of a PCF with a index profile in Ref. [23].

## 1.2. Fiber laser

The optical fiber is a cylindrical low-loss waveguide, the cross-sectional width of which is as narrow as a few micrometers and which longitudinal length can range from a few meters to hundreds of kilometers. Such fiber geometry ensures excellent performance as fiber-based optical amplifiers as well as optical

transmission in optical communications [1]. Fiber-based optical amplifiers are made by doping rare-earth ions, such as Ytterbium (Yb), Erbium (Er), or Thulium (Tm), to core area of optical fibers [18, 24]. In fiber-based optical amplifiers, launched light is amplified by stimulated emission from excited rare-earth ions. The most distinctive feature of the fiber-based optical amplifier compared to other optical amplifiers is that it is a waveguide-type amplifier, which allows to maintain the transverse mode of light and keep the beam quality high. In addition, the optical gain and amplification efficiency are high because it is amplified through a long optical fiber [24]. Such narrow and long geometries of fiber-based optical amplifiers also have the advantage of easier thermal management than bulk structures [25, 26]. Furthermore, the development of a double clad optical fiber allows high brightness pump light to be guided in an inner clad and interact more efficiently with gain ions, thereby leading to the emergence of new field of high-power fiber laser. In 2004, the development of high-power fiber lasers was greatly advanced, thereby breaking the 1-kW barrier with continuous wave (CW) Yb-doped fiber amplifiers [25].

Fiber-based optical amplifiers can be easily inserted into the resonator structure by exploiting fiber Bragg gratings or fiber couplers. In particular, the optical fiber ring resonator structure using the optical fiber coupler enabled the development of mode-locked fiber lasers. Mode-locked fiber lasers, which generate pulses of high peak power and narrow pulse width, enable the

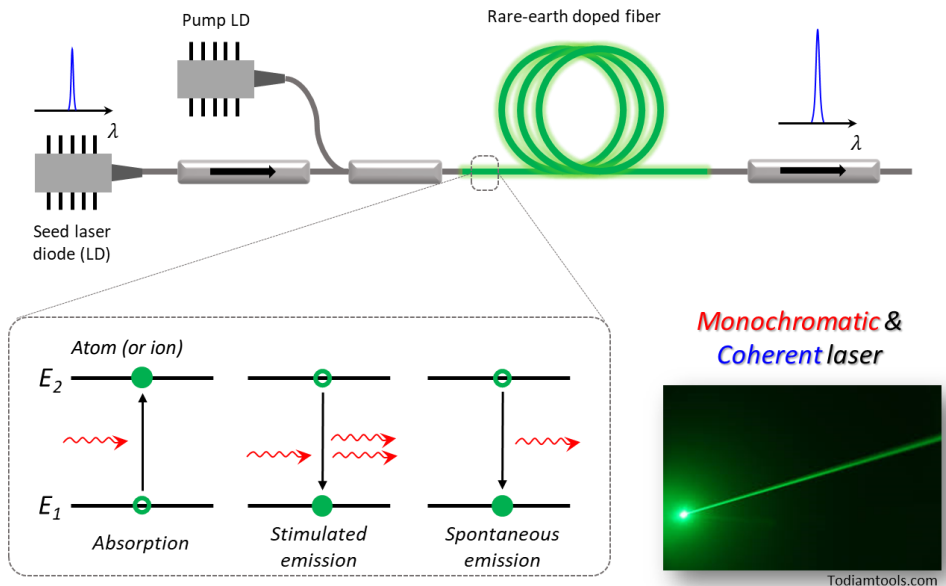


Fig. 1.2.1 Schematic diagram of a fiber amplifier made using rare-earth doped fibers. The inset is from Ref. [27].

exploration of various nonlinear optical phenomena caused by high peak power, and such nonlinear optical phenomena are recently applied in various applications such as optical sensors and biomedical optics [28]. Moreover, many studies have been conducted to increase the peak power or average power of pulse lasers through engineering of GVD and manipulation of nonlinear effects. Recently, a novel fiber laser system exploiting Mamyshev resonator with MW level peak power has been demonstrated and attracts great attention in the field of pulsed fiber lasers [29].

Fiber lasers have been developed in various ways to achieve the power, energy, and pulse widths required for engineering applications. However, the wavelength of emitted laser light has been greatly limited by rare-earth ions. For example, even though

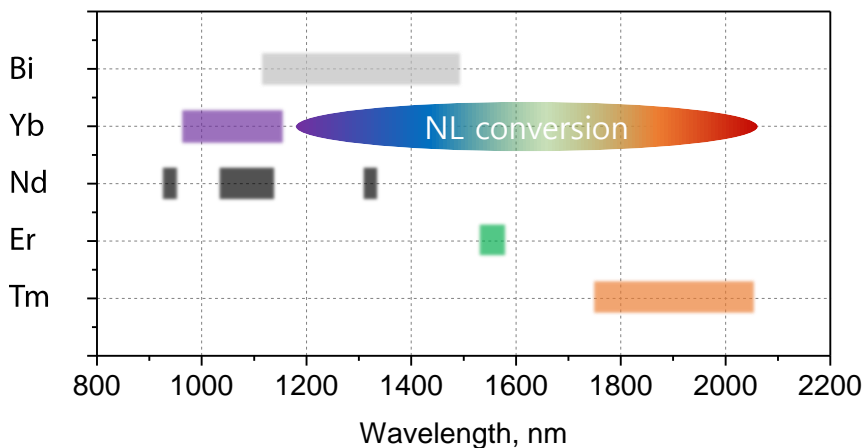


Fig. 1.2.2 Wavelength range of fiber laser according to the type of rare-earth ion

bio-medical applications such as optical coherence tomography require light in the wavelength range of 1200 to 1400 nm [30], rare earth ions have not yet been found that can amplify light at wavelengths in the region. LiDAR technology, which has recently been widely applied in autonomous vehicles and defense applications, requires laser light sources in the eye-safe wavelength band of 1400–1700 nm [31], but Erbium doped fiber amplifiers that amplify light in the wavelength region near 1500 nm have low amplification efficiency and cannot cover all of the wavelength band required for LiDAR applications. Thus, the bandwidth of gain materials currently used in fiber lasers alone cannot satisfy the wavelength requirements of the applications [24]. Although the wavelength of a fiber laser is largely limited by rare-earth ions, nonlinear wavelength conversion phenomena due to the

high nonlinearity of the fiber can be used to cover the wavelength range, as shown in Fig. 1.2.2 [1]. Recently, researches for generating a broadband light source covering a wide wavelength band using nonlinear optical phenomena, such as Raman and Brillouin scattering, SPM, and FWM have been actively conducted.

### 1.3. Nonlinear fiber optics

With the advent of high-power fiber lasers, nonlinear optical phenomena have become more frequent in optical fibers, and nonlinear fiber optics has emerged as the most important part of fiber optics [1].

In any dielectric material, if a sufficiently strong electromagnetic field is launched to the material, the bound electrons of the dielectric medium will exhibit a nonlinear response to the field. The response to the field of bound electrons will appear as dipole moment and total polarization as following [32]:

$$\mathbf{P} = \epsilon_0 (\chi^{(1)} \cdot \mathbf{E} + \chi^{(2)} : \mathbf{E} \mathbf{E} + \chi^{(3)} : \mathbf{E} \mathbf{E} \mathbf{E} + \dots), \quad (1,3,1)$$

where  $\epsilon_0$  is the vacuum permittivity and  $\chi^{(n)}$  is the  $n$ -th susceptibility. In general,  $\chi^{(1)}$  is most dominant, and the refractive index is almost determined by  $\chi^{(1)}$ . All higher-order terms after the second order are due to the anharmonic motion of the bound electrons, which contribute to polarization when the field strength is large enough. Among them, the second susceptibility,  $\chi^{(2)}$ , is

nearly zero due to the amorphous structure of the optical fiber. The most dominant nonlinear optical phenomenon in optical fibers is due to the third susceptibility,  $\chi^{(3)}$ . Nonlinear optical phenomena caused by  $\chi^{(3)}$  are called Kerr nonlinearity. Since Kerr nonlinearity is a response function for three fields, intensity-dependent refractive index, third-harmonic generation, and four-wave mixing are representative phenomena of Kerr nonlinear effects. Raman (Brillouin) scattering caused by optical (acoustic) phonons is also considered as the third-order nonlinear effect [1, 32]. Among them, the intensity-dependent refractive index causes the phenomenon of self-phase modulation (SPM) in which the phase is changed by the intensity of the pulse itself, and cross-phase modulation (XPM) in which the phase is changed by the intensity of another pulse [1]. SPM forms an optical soliton by balancing with GVD in the AD domain, and XPM is applied as various technologies such as nonlinear polarization rotation based saturable absorber and nonlinear loop mirror [4].

## 1.4. Supercontinuum generation

With the development of PCFs with high nonlinearity and engineering dispersion characteristics, nonlinear wavelength conversion studies using PCFs have been actively conducted. In particular, when a sub-picosecond ultrafast pulse with a high peak power of kW is applied to the PCF, the ultrafast pulse expands the

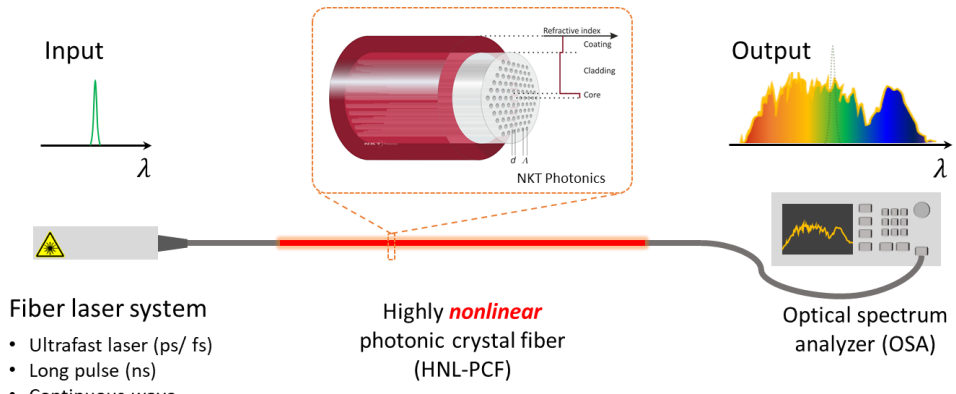


Fig. 1.4.1 Scheme of SCG via highly nonlinear PCF (the incet is from Ref. [23])

spectrum to hundreds to thousand nanometers by interplay of dispersion, SPM, FWM, and Raman scattering. Therefore, it is possible to create a broadband spectral light source that can cover whole visible wavelength band if the PCF characteristics and the pump pulse are well controlled [33]. This broadband spectrum is called supercontinuum (SC), and the process of generating SC is called SC generation (SCG).

SC is usually generated by applying a pump pulse in the AD wavelength region to the PCF. When a sub-ps pump pulse which wavelength is in the AD wavelength range, the pump pulse spectrum is expanded by the SPM. Then, the pump pulse is split into multiple solitons and dispersive waves (DWs) by third-order dispersion, Raman scattering, and modulation instability. DWs are phase-matched to the solitons in the ND region, causing the SC spectrum to extend towards the blue frequency. In addition, soliton in the AD region is gradually red-shifted by Raman scattering. This process broadens the SC spectrum from side to side [34]. Besides

the SCG pumped in AD region (AD–SCG), a spectrum can also be extensively extended via SPM and FWM in the normal dispersion (ND) region, which is called as ND–SCG. In ND–SCG, the spectrum is also broadened by the interaction of launched dark solitons and DWs in the AD region [35]. In addition, there is one more type of SCG, which is generated via PCF with flattened all-normal dispersion (FAND). The distinguishable feature of SCG in FAND (FAND–SCG) is that the FAND–SCG is only due to coherent spectral broadening processes including SPM and FWM. Thus, coherence property of the FAND–SCG is much better than the two other SCGs [34]. Consequently, SCG is a phenomenon that occurs when the energy spectrum of the pump pulse applied from the input stage is spread to other wavelength regions by nonlinear optical phenomenon.

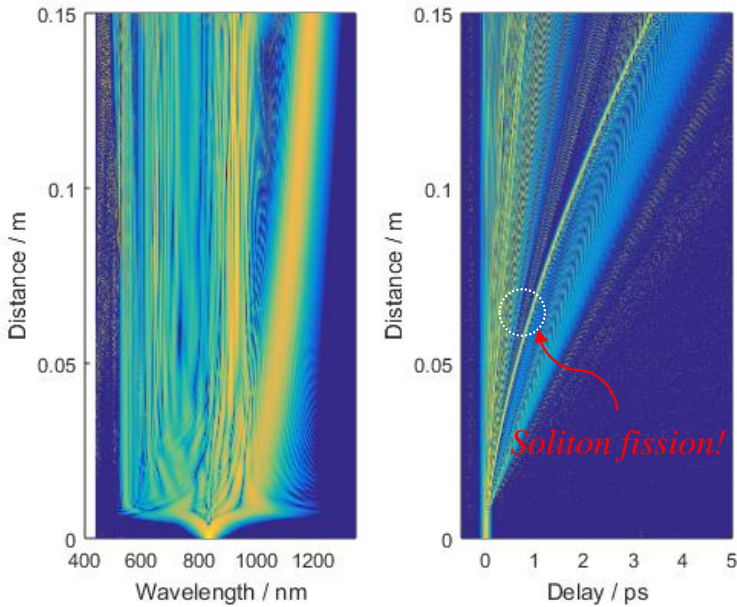


Fig. 1.4.2. SCG via highly nonlinear PCF, which is a reproduced figure in Ref. [12]

## 1.5. Motivation

In virtue of advances in fiber fabrication and fiber laser technology, nonlinear fiber optics could be studied extensively. Also, thanks to the academic achievement of such nonlinear fiber optics, wideband fiber lasers covering a wide wavelength band could be developed in various ways. A broadband fiber laser based on a nonlinear wavelength conversion phenomenon is a light source that is generated when an energy spectrum of a pump pulse applied from an input port spreads to other wavelength regions by a nonlinear optical phenomenon.

The SC light source can be applied to various fields such as optical sensor [30], bio-medical imaging [28], and optical communication [36] in virtue of its ultra-broadband characteristics. Simultaneously, the SC light source has difficulty in power scaling due to its ultra-broadband characteristics. Even if someone wants to amplify a wide band SC radiation as shown in Fig. 1.5.1, there is no rare-earth ion that can cover the ultra-wide spectrum of several hundred nm. Thus, even if the amplifier is inserted after the HNL-PCF as shown in Fig. 1.5.2 (b), only a portion corresponding

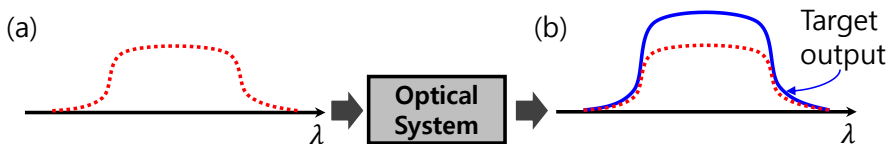


Fig. 1.5.1. Concept of the amplification system of broadband SC radiations

to the bandwidth of the amplifier will be amplified because the bandwidth of the amplifier is much smaller than the bandwidth of the SC. Thus, in a typical SCG system, the amplify stage is inserted before the nonlinear conversion stage as shown in Fig. 1.5.2 (c). The energy and peak power of the pump pulses will be much amplified so that the energy of the SC pulses coming out will also be much increased. However, when the peak power of the pump pulse is amplified by the amplifier, the nonlinear phenomenon experienced by the HNL-PCF is also increased, so that the linewidth is significantly increased much more than the average spectral power. Therefore, the combination of the conventional passive HNL-PCF and the fiber amplifier has a limitation in power scaling of SC pulses [37].

To approach this problem, this paper will theoretically examine the nonlinear optical phenomena and SCG in the active type HNL-PCF combined with the fiber amplifier and HNL-PCF (Fig. 1.5.2 (d)). An active-type HNL-PCF is a HNL-PCF doped with rare-earth ions in the core, which can be fully implemented with current advanced fiber fabrication technology. In the previous studies, SCG using Yb-doped fiber (YDF) has been studied similarly to Fig. 1.5.2 (d), but YDF has a low nonlinearity compared to low PCF. [38]. In 2016, L. A. Vazquez-Zuniga et al. fabricated a highly linear fiber amplifier by doping Er ion to soft glass fibers which nonlinearity is sufficiently high. The authors observed that by applying a ps pulse to a high-nonlinearity fiber amplifier, the linewidth was increased

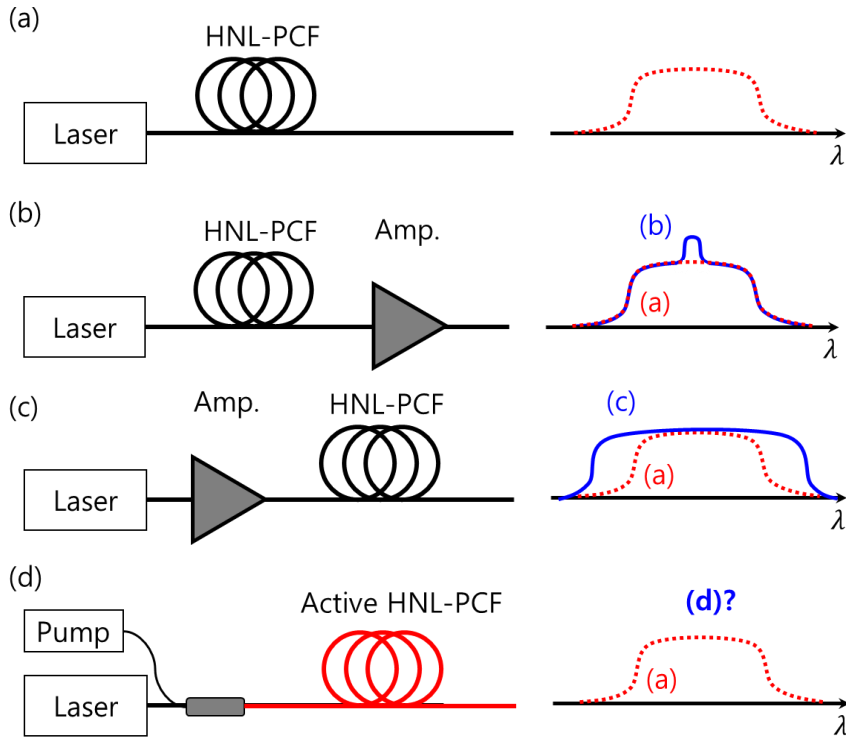


Fig. 1.5.2. Concept of the amplification system of broadband SC radiations: (a) SCG system without any amplifier stages and its output spectrum as a reference, (b) SCG system with an amplifier stage after the HNL-PCF and output spectrum, (c) SCG system with a pre-amplifier stage before the HNL-PCF and its output spectrum, (d) SCG system made of an active HNL-PCF which is an all-in-one system of the HNL-PCF and the fiber amplifier, and the resultant output spectrum

to about 350 nm per unit length [39]. According to the study, when high nonlinearity and optical gain exist simultaneously, nonlinear optical phenomena continue to occur because the optical gain continues to amplify the pump pulse, which is the seed of nonlinear wavelength conversion. Against this background, this study theoretically examines how SCG, which occurs in the presence of high nonlinearity and optical gain, differs from SCG generated only by nonlinearity.

As mentioned earlier, nonlinear optical phenomenon that pulses experience under the complex interaction of dispersion and nonlinearity is the heart of the SCG. In particular, the optical soliton and nonlinear optical phenomena experienced by the soliton are the core of the AD-SCG. Thus, SCG in an environment where both optical gain and high nonlinearity exist simultaneously can be regarded as a physical environment where the optical soliton interacts with optical gain, high nonlinearity, and dispersion of optical fiber in a complicated manner. Conventional SCG is a phenomenon that depends on soliton dynamics in closed system with little energy inflow from external system. On the other hand, the SCG considered in this study is a phenomenon that depends on the soliton dynamics in the open system where the energy is continuously injected from the external system. On the other hand, the formation of individual soliton in the open system has been studied a lot. In particular, many studies have been reported on dissipative soliton in which both optical gain, optical loss, and nonlinearity and fiber dispersion are balanced [10]. However, the physics of these solitons interacting complexly in open systems has not been studied. Therefore, this study is not only an engineering study of power scaling of SCG, but also a scientific study of nonlinear optics in open systems.

## **1.6. Scope of the study**

In this dissertation, I theoretically explore SCG in active-type HNL-PCFs. In particular, SCG and related soliton dynamics in the AD and FAND regions are examined. Since the soliton from a pulse with a peak power of kW typically has a width of femtosecond, a rigorous model is required to handle the interaction of these ultrafast solitons with rare-earth ions. Chapter 2 first discusses the nonlinear Schrödinger equation (NLSE), an equation that describes the nonlinear optical phenomena of ultrafast pulses. I also derive the Maxwell-Bloch equation for two-, three- and four-level structures, which describe the interaction of ultrafast pulses with rare-earth ions. Chapter 3 discusses the characteristics of SCG and associated bright soliton (BS) dynamics in Yb-doped HNL-PCF with a single ZDW. Next, the impact of BS dynamics on the characteristics of SCG is discussed. Chapter 4 discusses SCG characteristics and associated dark soliton (DS) dynamics in Yb-doped HNL-PCF with FAND characteristics. Next, the influence of dark soliton dynamics on the characteristics of SG is discussed. The final Chapter 5 concludes with a summary of the dissertation.

## Chapter 2

# Numerical model of ultrafast optics in active and nonlinear media

### 2.1. Numerical model of ultrafast optics

When a sub-picosecond ultrafast pulse is applied to the HNL-PCF, the pulse evolves into an SC pulse under the interaction of Kerr nonlinearity and dispersion, such as SPM, FWM, and Raman scattering [1, 12]. The dynamics of these pulses can be described by the NLSE, as follows:

$$\frac{\partial A}{\partial Z} = -\frac{\alpha}{2} - \sum_{m=2}^{\infty} \frac{i^{m-1} \beta_m}{m!} \frac{\partial^m A}{\partial T^m} + i\gamma \left( 1 + \tau_{\text{shock}} \frac{\partial}{\partial T} \right) A(Z, T) \int_{-\infty}^{\infty} R(T') |A(Z, T-T')|^2 dT' \quad (2.1.1)$$

where  $A$ ,  $p$ , and  $n$  denote the envelope of the optical field, the transition dipole moment, and the normalized population inversion, respectively;  $Z$  and  $T$  denote the propagation distance and the time coordinate in the co-moving frame at the envelope group velocity;  $\alpha$ ,

## Chapter 2. Numerical model of ultrafast optics in active & nonlinear media

$\beta_m$ , and  $\gamma$  denote the attenuation, the  $m$ -th order dispersion, and the nonlinear coefficients;  $\tau_{\text{shock}}$  denotes the shock coefficient for self-steepening, which is usually characterized by the inverse of the center angular frequency (i.e.,  $1/\omega_0$ ). The nonlinear response function is expressed by  $R(T) = (1-f_R)\delta(T) + f_R h_R(T)$ , which includes SPM and Raman response, where  $f_R$  is usually given by 0.2 for typical silica fibers. The Raman response function  $h_R(T)$  will be given in Section 2.1.3.

In the following section, physical phenomena (e.g. GVD, SPM, and Raman scattering) by each term will be analyzed sequentially.

### 2.1.1. Group velocity dispersion (GVD) in NLSE

In NLSE, GVD is characterized by  $\beta_2$ . If  $\beta_2$  is positive, red light is faster than blue light. if negative, blue light is faster than red light. To see how these GVD phenomena are described by the NLSE, let's write the equation as follows, except for the terms in the NLSE except for GVD.

$$\frac{\partial A}{\partial Z} = -\frac{i\beta_2}{2} \frac{\partial^2 A}{\partial T^2}. \quad (2.1.2)$$

The Fourier transform of this equation gives the following equation.

$$\frac{\partial \tilde{A}}{\partial Z} = i \frac{1}{2} \beta_2(\omega)(\omega - \omega_0)^2 \tilde{A}(Z, \omega - \omega_0). \quad (2.1.3)$$

This differential equation is the ordinary differential equation for  $Z$  and the solution is given as:

## Chapter 2. Numerical model of ultrafast optics in active & nonlinear media

$$\tilde{A}(Z, \omega - \omega_0) = \tilde{A}(0, \omega - \omega_0) \exp\left(\frac{i}{2} \beta_2(\omega) (\omega - \omega_0)^2 Z\right) \quad (2.1.4)$$

Accordingly, it can be seen that GVD induces a quadratic phase on spectral phase. This soon changes the temporal location of that frequency component, which in turn causes chirping of the pulse in the time domain. To verify this, I apply the Eq. (2.1.4) to the Gaussian pulse to extract the phase term as follows:

$$\phi(Z, T) = -\frac{\operatorname{sgn}(\beta_2) Z / L_D}{1 + (Z / L_D)^2} \frac{T^2}{2T_0^2} + \frac{1}{2} \tan^{-1}\left(\operatorname{sgn}(\beta_2) \frac{Z}{L_D}\right), \quad (2.1.5)$$

where  $T_0$  is width of Gaussian pulse and  $L_D$  is the dispersion characteristic length expressed by  $L_D = \frac{T_0^2}{|\beta_2|}$ . From Eq. (2.1.5), one can see that chirping is caused by GVD. When  $\beta_2$  is positive, up-chirping occurs when the frequency of the leading edge is lower than that of the trailing edge. When  $\beta_2$  is negative, down-chirping occurs when the frequency of the leading edge is higher than the frequency of the trailing edge. Chirping due to GVD causes compression or broadening of the pulse depending on the initial chirping of the pulse. If I denote the initial chirping of the pulse as  $C$ , for positive  $\operatorname{sgn}(C \beta_2)$ , the pulse is broadened, and for negative  $\operatorname{sgn}(C \beta_2)$ , the pulse is compressed.

### 2.1.2. Self-phase modulation (SPM) in NLSE

The nonlinear coefficient  $\gamma$  is a characterizing coefficient associated with nonlinear phenomena in NLSE, causing Kerr nonlinear effects such as SPM or intrapulse FWM. To discuss the SPM, this section analyzes the NLSE, including only the SPM term.

$$\frac{\partial A}{\partial Z} = i\gamma |A|^2 A \quad (2.1.6)$$

Looking at Eq. (2.1.6), one can see that the SPM term only changes the phase. In other words, the intensity of the field does not change, and one can obtain the solution of Eq. (2.1.6) as:

$$A(Z, T) = A(0, T) \exp(i\gamma |A|^2 Z) \quad (2.1.7)$$

This means that field at each time undergoes an additional phase shift by instantaneous intensity. This is nonlinear chirping depending on intensity. The chirping is calculated as follows.

$$\delta\omega(Z, T) = -\gamma \frac{d|A(T)|^2}{dT} Z \quad (2.1.8)$$

The nonlinear chirping calculated by applying this to Gaussian and super-Gaussian pulse is shown in Fig. 2.1.1. Accordingly, it can be seen that the SPM causes red-shift at the leading edge of the bright pulse and blue-shift at the trailing edge. In other words, the phenomenon of increasing the linewidth of the spectrum by the SPM increases, which is proportional to the nonlinear phase shift. The nonlinear chirping by SPM causes nonlinear dynamics of the pulse with non-zero GVD.

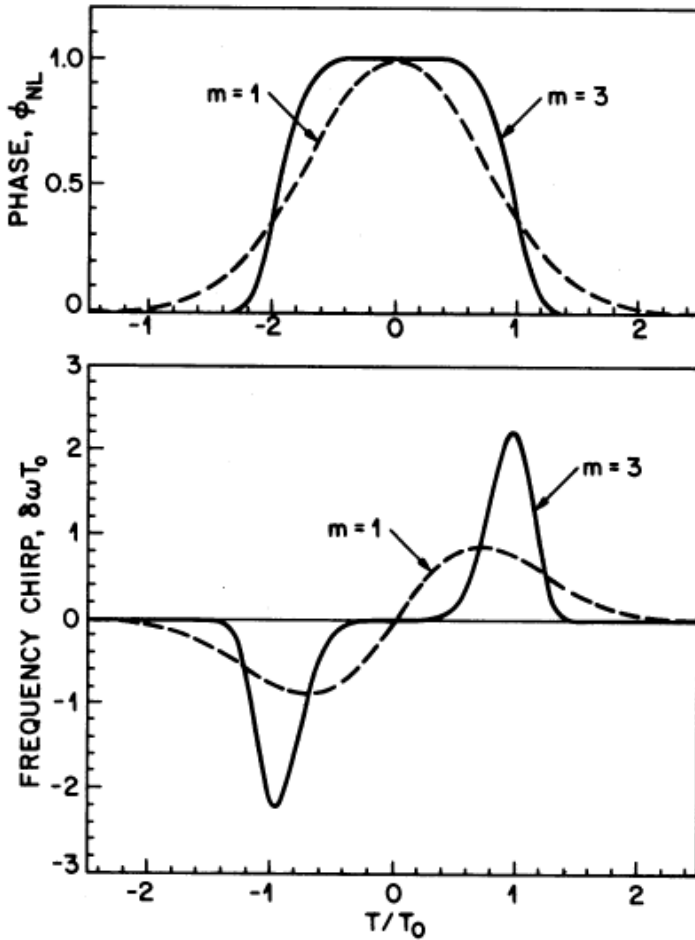


Fig. 2.1.1. Temporal variation of SPM-induced phase shift and frequency chirp for Gaussian (dashed curve) and super-Gaussian (solid curve) pulses in Ref. [1].

### 2.1.3 Time-delayed response in NLSE

Since optical pulses have a broader spectrum than CW, they suffer from Raman scattering rather than Brillouin scattering [1]. Raman scattering is inelastic scattering by optical phonons, where photons undergoing Raman Stokes scattering loses its energy and become low-frequency Stokes photons [1]. In addition, Stokes light is further amplified by the stimulated process, which is called

## Chapter 2. Numerical model of ultrafast optics in active & nonlinear media

stimulated Raman scattering (SRS). Photons undergoing Raman anti-Stokes scattering become photons with high frequency, anti-Stokes photons, but generally have a negative gain by a stimulated process. SRS is determined by the response of the optical phonon, which is slower than the response of the electron. Typical silica fibers have a response time of approximately 32 fs [1]. The time-delayed response by Raman scattering is modeled as follows:

$$h_R(T) = \frac{\tau_1^2 + \tau_2^2}{\tau_1 \tau_2} \exp(-T/\tau_2) \sin(T/\tau_1), \quad (2.1.9)$$

where  $\tau_1$  is the inverse of the optical phonon frequency and  $\tau_2$  is the lifetime of the optical phonon. In a typical silica fiber,  $\tau_1$  has about 12.2 fs and  $\tau_2$  has about 32 fs. Fourier transform of Eq. (2.1.9), gives Raman gain spectrum as shown in Fig. 2.1.2. This Raman response causes Raman-soliton self-frequency shift (RSSFS) and intrapulse Raman scattering (IRS) to be introduced later.

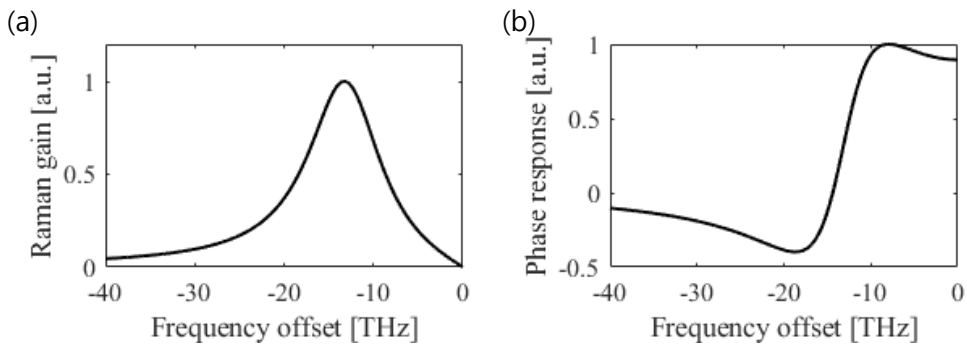


Fig. 2.1.2. (a) Raman gain spectrum and (b) phase response obtained by Eq. (2.1.9)

### 2.1.4 Bright (dark) soliton formation in AD (ND) regime

Sections 2.1.1 and 2.1.2 review GVD and SPM respectively. GVD and SPM govern the spectral–temporal dynamics of the pulse, causing linear and nonlinear chirping, respectively. However, there are conditions under which two types of chirping are compensated for each other. In this case, the optical pulse is maintained in its shape and guided without any change in the spectral–temporal domain. This special pulse is called an optical soliton. In particular, the AD region is down–chirped by GVD and at the same time nonlinear up–chirping by SPM. Thus, in the AD domain, GVD and SPM can be balanced to form a soliton. This corresponds to the eigenstate in the eigenvalue problem derived by applying an inverse scattering transform to the NLSE [40, 41]. In this case, the eigenvalue is distributed along the discrete spectrum, and the eigenvalue is represented by  $N$ , the soliton number.  $N$  is expressed as  $L_D / L_{NL}$ , where  $L_{NL}$  is a nonlinear characteristic length expressed as  $1/\gamma P_0$ . The soliton corresponding to  $N = 1$  is called fundamental soliton [1, 41]. In particular, when CW is applied in the AD region, fluctuation occurs in CW due to modulation instability, and soliton occurs spontaneously from the fluctuation. Therefore, a large number of optical solitons spontaneously occur in SCG in the AD region. Since the soliton in the AD region is a bright pulse on the zero–intensity background, it is also called bright soliton (BS).

On the other hand, for the bright pulse of the ND region, the

## Chapter 2. Numerical model of ultrafast optics in active & nonlinear media

linear and nonlinear chirping cannot be balanced. This is because both chirping by ND and chirping by SPM are positive chirping. Thus, bright pulses in the ND region generally undergo endless broadening. However, assuming CW boundary conditions in the NLSE, one can obtain stable soliton solutions even in the ND region, which is called dark soliton (DS). The DS is a dark pulse on a light background and corresponds to an eigenstate with a continuous spectrum in the IST eigenvalue problem. Figure 2.1.3 compares the typical characteristics of BS and DS. BS is symmetric without chirping, while DS is anti-symmetric with phase shift in the middle of dip [42].

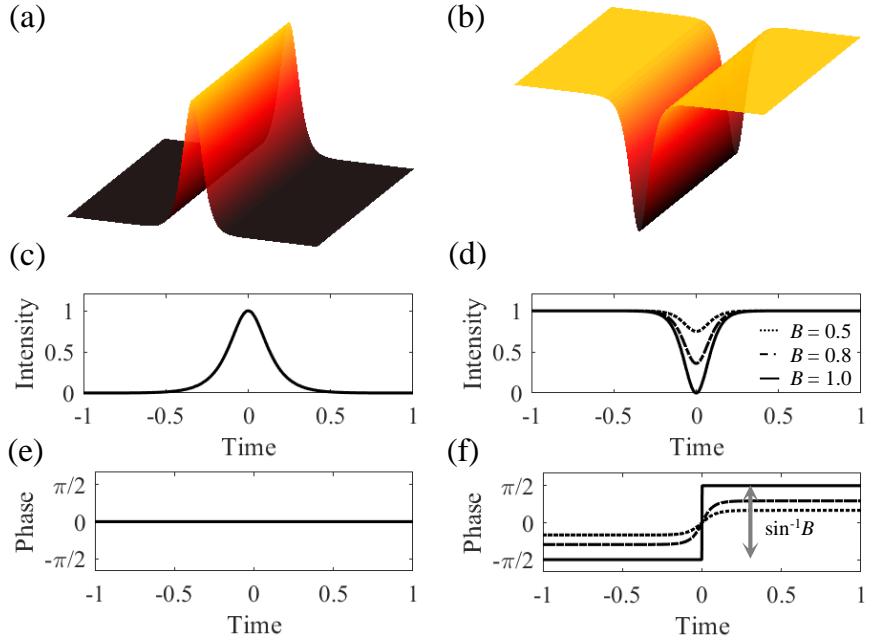


Fig. 2.1.3. Three dimensional visualization of propagation of (a) BS and (b) DS. Intensity profile of (c) BS and (d) DS. Phase profile of (e) BS and (d) DS. From this figure, one can find that BS is symmetric, whereas DS is anti-symmetric.

## 2.2. Semiclassical model of light–matter interaction

### 2.2.1. Overview of Maxwell–Bloch equation (MBE)

In classical physics, a state of a physical system is determined in a definite way [43]. For example, if there are two states A and B which the system can stay, then the system definitely belongs to either state A or B. However, in quantum mechanics, quantum system can belong to superposition of two states (i.e.  $|\psi\rangle = c_a|a\rangle + c_b e^{i\phi}|b\rangle$ , where  $c_a$  and  $c_b$  are real) [43]. According to Copenhagen interpretation, by measurement process, the system wave function  $|\psi\rangle$  collapses to either  $|a\rangle$  or  $|b\rangle$  with a probability of  $c_a^2$  and  $c_b^2 (=1-c_a^2)$ , respectively. The important thing is that the system inherently has the possibility of two states in form of superposition of two wave functions. This is the most distinguishable feature from classical physics where the system should have either A or B state and the determined state is not determined at the moment of measurement [43].

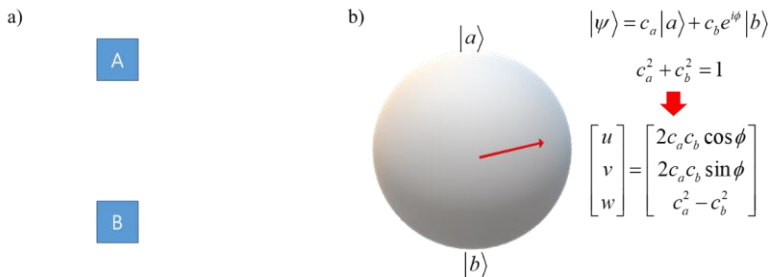


Fig. 2.2.1. (a) State diagram of two states in classical physics, (b) State diagram of two states in quantum physics called as Bloch vector representation

## Chapter 2. Numerical model of ultrafast optics in active & nonlinear media

Thus, the superposition is the most important and fundamental feature of quantum systems [43, 44]. Sometimes, we call the property of superposition of states as quantum coherence. Coherence means a fixed relationship between the phase of waves. Two waves are coherent when the phase difference is constant. If they are not coherent if there is a random or changing relationship. In other words, coherence means a property of wave which can interfere by other waves having the same frequency with a fixed phase relationship. In quantum mechanics, quantum coherence manifests itself in the form of an interference effect of two wave functions. For example, the observation probability distribution of a particle of the quantum state on x-axis is described by  $\langle \psi | \hat{x} | \psi \rangle = c_a^2 \langle a | \hat{x} | a \rangle + c_b^2 \langle b | \hat{x} | b \rangle + (c_a c_b e^{-i\phi} \langle b | \hat{x} | a \rangle + c.c.)$  [44]. In the point of view of wave theory, the first two terms correspond to intensities of each beam and the last two terms correspond to interference pattern. What if the last two terms disappear due to some decoherence effects? Then, the probability is nothing but probability of classical system which will belong to either state A or B. The system is nothing but classical system not having quantum properties. This is why we call the property of preservation of superposition state as quantum coherence.

Then, what happens if quantum coherence is considered in light-atom interaction? If we abandon the quantum coherence of atoms in light-atom interaction still holding the concept of quantization of states, the system behavior is the same with what

## Chapter 2. Numerical model of ultrafast optics in active & nonlinear media

Einstein had considered in his remarkable paper, ‘On the quantum theory of radiation (1917)’ [45]. He had described the interaction of light and quantized atoms via the well-known rate equations. However, if we consider the quantum coherence for further steps, response of the system is largely different against the rate equations. This will be shown in this report.

The superposition of two states has been described as Bloch vector in an efficient way. If a system has a chance to choose a state A or B, then in classical physics, we can just draw two boxes for two states. However, in quantum system, two boxes are not enough for description of the state because the system is the superposition of two states with a fixed phase relationship. Thus, Bloch had developed a Bloch vector expression which can represent the superposed quantum states on a sphere, which is an homage to Poincare sphere for representation of polarization of optical waves [46]. Even though light waves can be described by field quantization, the mean photon number of light waves is extremely large, Maxwell equations are nice equations to describe propagation of light waves. Thus, the interaction of light waves of many photons and atoms can be described by coupled Maxwell equations and Schrödinger equations. We call the coupled equation set as Maxwell–Bloch equations [44]. Then, how can we couple the macroscopic Maxwell equation and the microscopic Schrödinger equation? The key point is making microscopic things macroscopic through statistical summation [44]. One can obtain the microscopic

Chapter 2. Numerical model of ultrafast optics in active & nonlinear media

transition dipole moment by solving the Schrödinger equation. Then, we do the statistical summation of the microscopic transition dipole moment and obtain the macroscopic polarization as a result. The macroscopic polarization drives the electric field and the electric field again change the microscopic transition dipole moment through coherent light–atom interaction. The Maxwell–Bloch equations are self–consistent in this way.

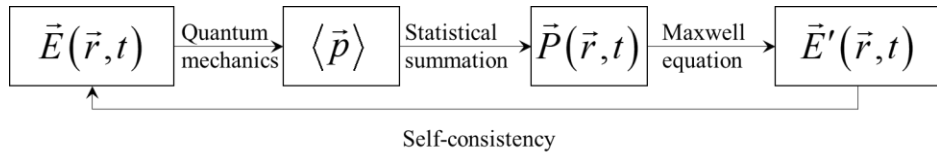


Fig. 2.2.2. Electric field induces microscopic dipole moment according to the laws of quantum mechanics. These moments are then summed to yield the macroscopic polarization of the medium, which acts as a source in Maxwell's equations. The condition of self-consistency then requires that the assume field equal to the reaction field.

### 2.2.2. MBE for a two-level system

Under the slowly varying envelope approximation (SVEA) and adopting co-moving frame ( $Z, T$ ), Maxwell–Bloch equation is simply described as following [44]:

$$\frac{\partial A}{\partial Z} = i\gamma_Q P \exp(-ik_0 z) \quad (\text{Macroscopic}), \quad (2.2.1)$$

$$\frac{\partial p}{\partial T} = - \left( \frac{1}{T_2} - i\Delta_a \right) p - \frac{i\mu^2}{\hbar} En \quad (\text{Microscopic}), \quad (2.2.2)$$

$$\frac{\partial n}{\partial T} = -\frac{1}{T_1}(n+1) + \frac{2i(Ep^* - E^* p)}{\hbar} \quad (\text{Microscopic}), \quad (2.2.3)$$

## Chapter 2. Numerical model of ultrafast optics in active & nonlinear media

Microscopic equations are coupled to the macroscopic Maxwell equation via  $P = N_0 p$ , which means the transition dipole moment  $p$  represents behavior of atomic ensemble at  $(Z, T)$ . In Eq. (2.2.1)–(2.2.3),  $p$  represents the complex phasor form of the transition dipole moment, where the time-harmonic term is factored out. More specifically, the transition dipole moment is represented by  $\tilde{p} = p e^{-i\omega_0 t} + p^* e^{i\omega_0 t}$  and  $\tilde{p} = \mu\rho_{21} + \mu\rho_{12}$ . Another quadrature is expressed as  $\tilde{q} = i\mu\rho_{21} - i\mu\rho_{12}$ .

The concept of the saturation energy is automatically given in the rate equation approximation. The rate equation approximation approximates Maxwell–Bloch equation assuming the fast decay of the coherent interaction which is represented by Eq. (A.1.8) (See Appendix A for details of the rate equation approximation and derivation of Maxwell–Bloch equations). If the pulse width is much longer comparing to the dipole decay time (i.e.  $T_2$  time), the transition dipole  $p$  rapidly decays to a certain steady state;  $p \rightarrow p^{ss}$ .

At the steady state, Eq. (A.1.8) becomes

$$-\left(\frac{1}{T_2} - i\Delta_a\right)p^{ss} - \frac{i\mu^2}{\hbar} An = 0, \quad (2.2.4)$$

$$p^{ss} = -\frac{i\mu^2 T_2}{\hbar} \frac{1}{1 - iT_2 \Delta_a} An, \quad (2.2.5)$$

where  $p = \bar{p}$  for simple notation (Then,  $\tilde{p} = p \exp(i(k_0 z - \omega_0 t)) + c.c.$ ).

Substituting Eq. (A.1.8) to Eq. (A.1.12), the equation for the normalized population inversion is obtained as;

$$\begin{aligned}
 \frac{\partial n}{\partial T} &= -\frac{1}{T_1}(n+1) + \frac{2i}{\hbar}(Ap^{ss*} - A^* p^{ss}) \\
 &= -\frac{1}{T_1}(n+1) - \frac{4\mu^2 T_2}{\hbar^2} |A|^2 n \frac{1}{1+(T_2 \Delta_a)^2} \\
 &= -\frac{1}{T_1}(n+1) - \frac{2\mu^2 T_2}{\hbar^2 n c \varepsilon_0} I n \frac{1}{1+(T_2 \Delta_a)^2} \\
 &= -\frac{1}{T_1}(n+1) - \frac{I}{\hbar \omega_0 / (2\mu^2 T_2 \omega_0 / \hbar n c \varepsilon_0)} \frac{1}{1+(T_2 \Delta_a)^2} n \\
 &= -\frac{1}{T_1}(n+1) - \frac{I}{\hbar \omega_0 / \sigma_s} \frac{1}{1+(T_2 \Delta_a)^2} n
 \end{aligned} \tag{2.2.6}$$

The transition cross section is defined as  $\sigma_s = \frac{2\mu^2 T_2 \omega_0}{\hbar n c \varepsilon_0}$ . If the pulse width  $T_p$  is longer than  $T_2$  and shorter than  $T_1$  (i.e.  $T_2 < T_p < T_1$ ) and the spontaneous decaying  $T_1$  time is typically given by 0.1 ms in my consideration (e.g. Ytterbium or Erbium ions), then the slow evolution of the first term becomes negligible, so that

$$\frac{\partial n}{\partial T} = -\frac{I}{\hbar \omega_0 / \sigma_s} \frac{1}{1+(T_2 \Delta_a)^2} n \quad (T_2 < T \ll T_1) \tag{2.2.7}$$

$$n(Z, T) = \int_{-\infty}^T -\frac{I(Z, T')}{\hbar \omega_0 / \sigma_s} \frac{1}{1+(T_2 \Delta_a)^2} n(Z, T') dT' \tag{2.2.8}$$

$$n(Z, T) = n(Z, T = -\infty) \frac{1}{1+(T_2 \Delta_a)^2} \exp\left(-\frac{1}{\hbar \omega_0 / \sigma_s} \int_{-\infty}^T I(Z, T') dT'\right) \tag{2.2.9}$$

In Eq. (2.2.7), the saturation energy is given by  $E_{sat} = \hbar \omega_0 \frac{A_{eff}}{\sigma_s}$  which is the amount of energy delivered by an optical wave at which  $E_{pulse} \sigma_s / A_{eff} = \hbar \omega_0$ . In other words, the saturation energy is the optical energy at which every single atom effectively absorbs the single photon energy  $\hbar \omega_0$ . However, Eq. (2.2.7) is just valid for

## Chapter 2. Numerical model of ultrafast optics in active & nonlinear media

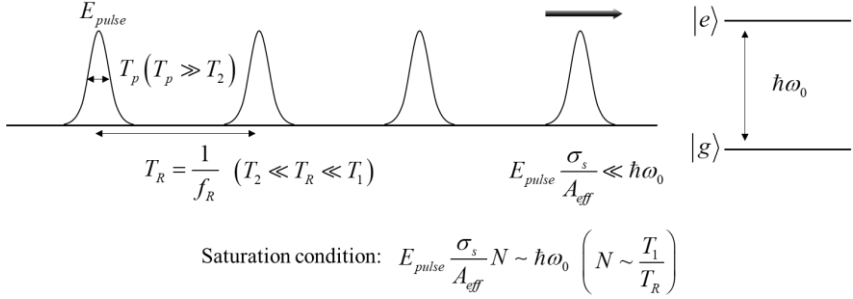


Fig. 2.2.3. Interaction of multiple pulses with the fixed repetition rate and atoms where quantum coherence is negligible, and the condition of gain saturation.

optical waves within  $T_1$  time. The reason is that the first term keeps pulling down the state to the ground state with  $T_1$ , such that  $n(Z,T) = n(Z,T_0) \exp(-(T-T_0)/T_1) - 1$ . Then, it can be deduced that at certain time, the force pulling down to the ground state and the force pulling up to the excited state by the presence of optical fields can be balanced,

$$n^{ss} = -\frac{1}{1 + \frac{I_{av}T_1}{\hbar\omega_0/\sigma_s} \frac{1}{1 + (T_2\Delta_a)^2}}. \quad (2.2.10)$$

The meaning of Eq. (2.2.10) is simple. If optical energy absorbed by atoms during the  $T_1$  time, is equal to the energy of single photon, then the gain is reduced to half of the unsaturated gain. For the case of single pulse generated in optical fiber laser systems,  $I_{av}T_1$  is much less than  $\hbar\omega_0/\sigma_s$ , where  $I_{av}$  is an averaged intensity of a single pulse. However, in practice, pulses propagate with a fixed repetition rate. In case of optical fiber laser systems, the repetition rate is about 10 – 100 MHz. Thus,  $I_{av}T_1$  becomes comparable to  $\hbar\omega_0/\sigma_s$ , when the multiple pulses with the repetition

## Chapter 2. Numerical model of ultrafast optics in active & nonlinear media

rate interacts to atoms. It also should be noted that at the saturation energy, the gain is negative.

### 2.2.3. MBE for a three-level system

$\text{Er}^{3+}$  ion has been used for gain material for amplification of 1550-nm wavelength light, which is a representative three-level quantum emitter as shown in Fig. 2.2.4. This scheme can increase lasing efficiency compared to the two-level scheme. In the two-level system, the laser field acts a role of pump and signal at the same time. The laser field excites the atom and simultaneously stimulates atom to emit the same mode photon to the laser field. Thus, the two-level atom is easily saturated. To avoid the saturation problem and to improve lasing efficiency, pump wavelength can be separated from signal wavelength. The pump laser increases the population of atoms at state  $|3\rangle$ , and the atoms rapidly decay to state  $|2\rangle$ . This pumping process does not stimulate atoms at state  $|2\rangle$  and does not induce stimulated photon emission, unlike two-level systems where the pump laser stimulated the excited state ions to induce stimulated photon emission and saturation of two-level atoms. In this section, how the three-level system is different to the previous two-level system will be shown in terms of the saturation energy and the saturated population inversion for multiple pulses.

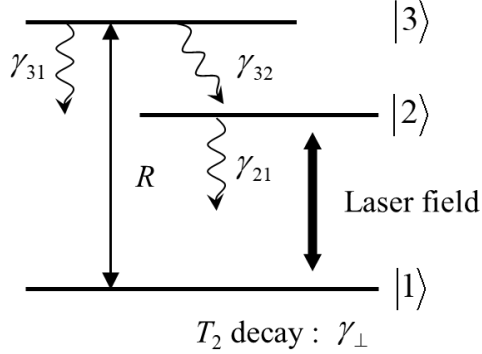


Fig. 2.2.4.  $\text{Er}^{3+}$  energy level

The Maxwell–Bloch model for the three–level atom is following [47]:

$$\dot{\rho}_{33} = -\gamma_{32}\rho_{33} + R(\rho_{11} - \rho_{33}), \quad (2.2.11)$$

$$\dot{\rho}_{22} = -\gamma_{21}\rho_{22} + \gamma_{32}\rho_{33} + \frac{i\mu\tilde{E}}{\hbar}(\rho_{12} - \rho_{21}), \quad (2.2.12)$$

$$\dot{\rho}_{11} = \gamma_{21}\rho_{22} - R(\rho_{11} - \rho_{33}) - \frac{i\mu\tilde{E}}{\hbar}(\rho_{12} - \rho_{21}), \quad (2.2.13)$$

$$\dot{\rho}_{12} = i\omega_{12}\rho_{12} - \gamma_{\perp}\rho_{12} + \frac{i\mu\tilde{E}}{\hbar}(\rho_{22} - \rho_{11}), \quad (2.2.14)$$

where  $R$  is pumping rate represented by  $\frac{P_p\sigma_{abs}(\omega_p)}{\hbar\omega_p A_{eff}}$ . In this

scheme, I presume that quantum coherent interaction by pump laser is negligible by the fast decay from state  $|3\rangle$  to  $|2\rangle$ . In other words, the rate equation approximation for  $|3\rangle - |1\rangle$  transition by optical pumping is already applied in Eq. (2.2.11). With conditions of  $\gamma_{32} \gg R, \gamma_{21}, \gamma_{\perp}$ , the three–level Maxwell–Bloch model can be approximated to the two–level Maxwell–Bloch model. The derivation is following;

## Chapter 2. Numerical model of ultrafast optics in active & nonlinear media

Due to the fast decay of atoms at state  $|3\rangle$ ,  $\dot{\rho}_{33}$  can be regarded in a steady state so that  $\dot{\rho}_{33}=0$ . With the steady state condition,  $\rho_{33}$  can be obtained from Eq. (2.2.11).

$$\rho_{33} = \frac{R}{R + \gamma_{32}} \rho_{11}, \quad (2.2.15)$$

In addition, from  $\rho_{11} + \rho_{22} + \rho_{33} = 1$  and Eq. (2.2.13), the relationship of  $\rho_{22}$  and  $\rho_{11}$  is given by  $\rho_{22} + \frac{2R + \gamma_{32}}{R + \gamma_{32}} \rho_{11} = 1$ . If we apply the condition of the fast decay of  $\rho_{33}$  to the relation, then we can presume that  $\rho_{22} + \rho_{11} \approx 1$ . The normalized population difference  $n = \rho_{22} - \rho_{11}$  is derived from Eq. (2.2.12), (2.2.13) and (2.2.15).

$$\begin{aligned} \dot{n} &= -2\gamma_{21}\rho_{22} + \gamma_{32}\rho_{33} + \frac{2i\mu\tilde{E}}{\hbar}(\rho_{12} - \rho_{21}) + R(\rho_{11} - \rho_{33}) \\ &= -(R + \gamma_{21})\left(n - \frac{R - \gamma_{21}}{R + \gamma_{21}}\right) + \frac{2i(Ep^* - E^*p)}{\hbar} \end{aligned}, \quad (2.2.16)$$

where  $\varepsilon = \frac{R}{\gamma_{32}} \ll 1$ . At the last step, the driving term in terms of electric field and the envelope of the dipole moment is derived with the definitions of the two quadrature  $\tilde{p}$  and  $\tilde{q}$  in two-level system. Compared to Eq. (2.2.3), it is easily turned out that in three-level systems, fluorescent decay time of the two-level system can be replaced to  $T_1^* = \frac{T_1}{1 + RT_1}$  and that if there is no driving term by electric fields, then the normalized population inversion decays to  $\frac{RT_1 - 1}{RT_1 + 1}$ . Thus, I can denote the term as the equilibrium

## Chapter 2. Numerical model of ultrafast optics in active & nonlinear media

population inversion with optical pumping;  $n_{eq} = \frac{RT_1 - 1}{RT_1 + 1}$ . If the number of the pump photon during  $T_1$  time is much larger than 1, then  $n_{eq}$  converges to 1, and  $T_1^*$  time decreases inversely proportional to the number of the pump photons. This means that  $n$  quickly reaches to  $n_{eq}$  within  $T_1^*$  time, unless the signal field is incident in medium. The derivation of the equation for the dipole moment is the same with the derivation of Eq. (A.1.11). Thus, the MBE for the three-level atom can be summarized as following:

$$\frac{\partial A}{\partial Z} = i\gamma_Q \bar{P} \quad (\text{Macroscopic}), \quad (2.2.17)$$

$$\frac{\partial \bar{p}}{\partial T} = -\left(\frac{1}{T_2} - i\Delta_a\right)\bar{p} - \frac{i\mu^2}{\hbar} An \quad (\text{Microscopic}), \quad (2.2.18)$$

$$\frac{\partial n}{\partial T} = -\frac{1}{T_1^*}(n - n_{eq}) + \frac{2i(A\bar{p}^* - A^*\bar{p})}{\hbar} \quad (\text{Microscopic}), \quad (2.2.19)$$

where  $T_1^* = \frac{T_1}{1+RT_1}$  and  $n_{eq} = \frac{RT_1 - 1}{RT_1 + 1}$ . It should be noted that these equations are valid with the assumption of  $\gamma_{31} \gg R, \gamma_{21}, \gamma_\perp$ .

### 2.2.4. MBE for a four-level system

$\text{Yb}^{3+}$  ion has been used as gain material for light amplification at 1064 nm wavelength, which has four-level energy structure as shown in Fig. 2.2.5. The ions are pumped at 976 nm wavelength and have high emission at 1064 nm wavelength, such that the saturation problem can be avoided. Furthermore,  $\text{Yb}^{3+}$  ion provides higher

## Chapter 2. Numerical model of ultrafast optics in active & nonlinear media

quantum efficiencies in lasing thanks to three main reasons: 1) The first reason is from separation of absorption states. While the pump and the signal laser simultaneously excite ions at the ground state in  $\text{Er}^{3+}$  ion, in  $\text{Yb}^{3+}$  ion, the pump laser excites ions at the state 0 and the signal laser excites ions at the state 1, such that two absorption processes are separated in the four-level structure. In the four-level structure, ions at the state 1 rapidly decay to the state 0, so that the population inversion between the state 2 and 1 is further enhanced than  $\text{Er}^{3+}$  ion (c.f. for  $\text{Er}^{3+}$  ion, more ions stay at the ground state so that pump power for the population inversion is more required than the case of  $\text{Yb}^{3+}$  ion). 2) Moreover, the absorption cross section and the emission cross section for  $\text{Yb}^{3+}$  ions are better for better lasing efficiency than  $\text{Er}^{3+}$  ions. 3) Small wavelength differences in absorption and emission wavelengths of  $\text{Yb}^{3+}$  ions than  $\text{Er}^{3+}$  ions give enhanced quantum efficiencies in lasing. In this section, assuming the fast decays from the state 3 to the state 2 and from the state 1 to the state 0, quantum-coherent interaction of the signal field at 1064-nm wavelength in Yb-doped optical fibers will be treated with the semiclassical framework.

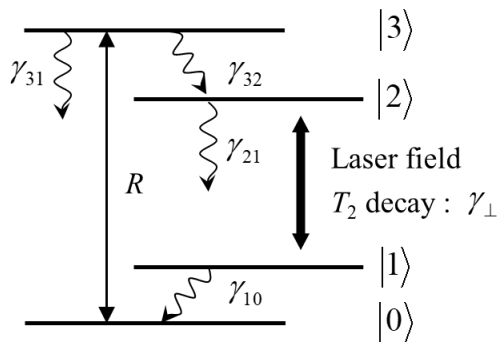


Fig. 2.2.5.  $\text{Yb}^{3+}$  energy level

## Chapter 2. Numerical model of ultrafast optics in active & nonlinear media

The Maxwell–Bloch equations for the four–level is given by [47]:

$$\dot{\rho}_{33} = -(\gamma_{30} + \gamma_{32})\rho_{33} + R(\rho_{00} - \rho_{33}), \quad (2.2.20)$$

$$\dot{\rho}_{22} = -\gamma_{21}\rho_{22} + \gamma_{32}\rho_{33} + \frac{i\mu\tilde{E}}{\hbar}(\rho_{12} - \rho_{21}), \quad (2.2.21)$$

$$\dot{\rho}_{11} = -\gamma_{10}\rho_{11} + \gamma_{21}\rho_{22} - \frac{i\mu\tilde{E}}{\hbar}(\rho_{12} - \rho_{21}), \quad (2.2.22)$$

$$\dot{\rho}_{00} = -R(\rho_{00} - \rho_{33}) + \gamma_{30}\rho_{33} + \gamma_{10}\rho_{11}, \quad (2.2.23)$$

$$\dot{\rho}_{12} = i\omega_{12}\rho_{12} - \gamma_{\perp}\rho_{12} + \frac{i\mu\tilde{E}}{\hbar}(\rho_{22} - \rho_{11}), \quad (2.2.24)$$

In Eq. (2.2.20) and (2.2.21), the transitions between the state 3 and the state 2 and between the state 1 and the state 0 are treated as rate equations due to fast decays by  $\gamma_{32}$  and  $\gamma_{10}$ . Assuming that  $\gamma_{32}$  and  $\gamma_{10}$  are much larger than any other decay rate, the MBE of the four–level system can be derived as following: Ions at state  $|3\rangle$  rapidly decay to state  $|2\rangle$  so that Eq. (2.2.20) can be treated by steady–state analysis. From Eq. (2.2.20) with the steady state approximation,  $\dot{\rho}_{33} \approx 0$  and  $\rho_{33} \approx \frac{R}{\gamma_{30} + \gamma_{32} + r}\rho_{00}$ .

Moreover, ions at state  $|1\rangle$  rapidly decay to state  $|0\rangle$  so that Eq. (2.2.22) can be treated by steady–state analysis. From Eq. (2.2.22) with the steady state approximation,  $\dot{\rho}_{11} \approx 0$ ,  $\dot{\rho}_{22} + \dot{\rho}_{00} \approx 0$ , and  $\rho_{22} + \rho_{00} \approx 1$ . This yields that

$$-\gamma_{10}\rho_{11} + \gamma_{21}\rho_{22} - \frac{i\mu\tilde{E}}{\hbar}(\rho_{12} - \rho_{21}) \approx 0, \quad (2.2.25)$$

## Chapter 2. Numerical model of ultrafast optics in active & nonlinear media

$$\begin{aligned}\dot{\rho}_{22} - \dot{\rho}_{11} &\approx \dot{\rho}_{22} \\ &= -\gamma_{21}\rho_{22} + R\rho_{00} + \frac{i\mu\tilde{E}}{\hbar}(\rho_{12} - \rho_{21}).\end{aligned}\quad (2.2.26)$$

On the other hand, the transition dipole moment equation, Eq. (2.2.24) is slightly different from those of three- or two-level systems. With the definition of the transition dipole moment  $p = \mu(\rho_{12} + \rho_{21})$ , the quadrature equations are derived;  $\dot{p} = -\omega_{12}\tilde{q} - \gamma_{\perp}\tilde{p}$  and  $\dot{\tilde{q}} = \omega_{12}\tilde{p} - \gamma_{\perp}\tilde{q} + \frac{2\mu^2\tilde{E}}{\hbar}(\rho_{22} - \rho_{11})$ . From the quadrature equations, the equation of the envelope of  $\tilde{p}$ ,  $p$  is derived as following:

$$\dot{p} = -(\gamma_{\perp} - i\Delta_a)p - \frac{i\mu^2}{\hbar}En. \quad (2.2.27)$$

The equation of the normalized population inversion can be obtained as:

$$\begin{aligned}\dot{n} &\approx \dot{\rho}_{22} = -(\gamma_{21} + R)\rho_{22} + R + \frac{i\mu\tilde{E}}{\hbar}(\rho_{12} - \rho_{21}) \\ &= -\frac{1}{T_1^*}(\rho_{22} - n_{eq}) + \frac{i(Ep^* - E^*p)}{\hbar},\end{aligned}\quad (2.2.28)$$

where  $T_1^* = \frac{1}{\gamma_{21} + R} = \frac{T_1}{RT_1 + 1}$  and  $n_{eq} = \frac{RT_1}{RT_1 + 1}$ . It is noteworthy that  $n_{eq}$

of the four-level system is larger than of the three-level system due to the presence of the decay from the state  $|1\rangle$  to  $|0\rangle$ :

$$\left( n_{eq}^{4-level} = \frac{RT_1}{RT_1 + 1} \right) > \left( n_{eq}^{3-level} = \frac{RT_1 - 1}{RT_1 + 1} \right)$$

Therefore, the Maxwell-Bloch equations for the four-level system can be summarized as following:

$$\frac{\partial A}{\partial Z} = i\gamma_Q \bar{P} \quad (\text{Macroscopic}), \quad (2.2.29)$$

$$\frac{\partial \bar{p}}{\partial T} = -\left(\frac{1}{T_2} - i\Delta_a\right)\bar{p} - \frac{i\mu^2}{\hbar}An \quad (\text{Microscopic}), \quad (2.2.30)$$

$$\frac{\partial n}{\partial T} = -\frac{1}{T_1^*}\left(n - n_{eq}\right) + \frac{i(A\bar{p}^* - A^*\bar{p})}{\hbar} \quad (\text{Microscopic}), \quad (2.2.31)$$

where  $T_1^* = \frac{T_1}{1+RT_1}$  and  $n_{eq} = \frac{RT_1}{RT_1+1}$ . It should be noted that these

equations are valid with the assumption of  $\gamma_{31} \gg R, \gamma_{21}, \gamma_\perp$ .

### 2.3. Gain saturation effect by an ultrafast pulse train

For application of generalized nonlinear Schrödinger equation – Maxwell–Bloch equation to supercontinuum generation in an active fiber, the theory should be slightly modified due to the assumption of  $T_p \gg T_2$ . In terms of temporal width, this condition is sufficiently satisfied in supercontinuum generation in all–normal dispersion regime. However, in terms of spectral bandwidth, the above condition cannot be held, because the pulse spectral bandwidth is significantly broadened by Kerr nonlinearity such that the spectral bandwidth is broader than the gain bandwidth  $1/T_2$ . If the spectral bandwidth is narrower than the gain bandwidth, the transition dipole  $p_{ss}$  will react almost constantly for all frequency components of the optical field  $A$ , so the Eq. (A.2.7) will hold for the case. However, if the spectral bandwidth is much broader than the gain bandwidth, the above assumption no longer holds, and  $p_{ss}$  will respond differently depending on the frequency component of the field  $A$ . In this

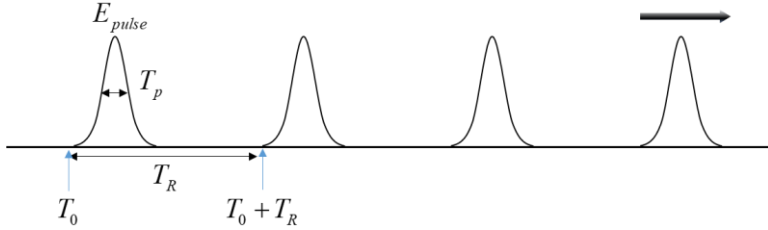


Fig. 2.2.6. A pulse train with a fixed repetition rate ( $1/T_R$ )

derivation, I will extend the theory to cover the amplification of supercontinuum pulse.

The Maxwell–Bloch equations for the three-/four–level system can be summarized as following:

$$\frac{\partial A}{\partial Z} = i\gamma_Q \bar{P} \quad (\text{Macroscopic}), \quad (2.3.1)$$

$$\frac{\partial \bar{p}}{\partial T} = -\left(\frac{1}{T_2} - i\Delta_a\right)\bar{p} - \frac{i\mu^2}{\hbar}An \quad (\text{Microscopic}), \quad (2.3.2)$$

$$\frac{\partial n}{\partial T} = -\frac{1}{T_1^*}(n - n_{eq}) + \frac{2vi(A\bar{p}^* - A^*\bar{p})}{\hbar} \quad (\text{Microscopic}), \quad (2.3.3)$$

$$\text{where } T_1^* = \frac{T_1}{1+RT_1}, \quad n_{eq} = \frac{RT_1-1}{RT_1+1} \quad (\text{three-level}), \quad \text{and} \quad n_{eq} = \frac{RT_1}{RT_1+1}$$

(four–level). In derivation of Eq. (A.2.7), it is assumed that Eq. (A.2.7) is at steady state. In other words, the assumption is equivalent to that  $\bar{p}$  will react to constantly for all frequency components of the optical field  $A$ , even for frequency components of  $A$  outside the gain bandwidth. Thus, for the extension of the theory, the assumption of the steady state of  $\bar{p}$  should be abandoned. I apply the Fourier transform to Eq. (2.3.2) to account for changes in time instead of steady state:

$$\bar{p}(Z, T) = \frac{1}{2\pi} \int_{-\infty}^{\infty} \tilde{p}(Z, \omega - \omega_0) e^{-i(\omega - \omega_0)T} d\omega \quad (2.3.4)$$

Substituting Eq. (2.3.4) to Eq. (2.3.2), the frequency response function of  $\bar{p}$  to  $A$  and  $n$  can be obtained:

$$\frac{1}{2\pi} \int_{-\infty}^{\infty} d\omega e^{-i(\omega - \omega_0)T} \cdot \left[ -i(\omega - \omega_0) \tilde{p} = -\left( \frac{1}{T_2} - i(\omega_0 - \omega_a) \right) \tilde{p} - \frac{i\mu^2}{\hbar} \tilde{A}n(T) \right] \\ (2.3.5)$$

$$\left( \frac{1}{T_2} - i(\omega - \omega_a) \right) \tilde{p}(Z, \omega - \omega_0) = -\frac{i\mu^2}{\hbar} \tilde{A}(Z, \omega - \omega_0) n(T). \quad (2.3.6)$$

$$\tilde{p}(Z, \omega - \omega_0) = -\frac{i\mu^2 T_2}{\hbar} \frac{\tilde{A}(Z, \omega - \omega_0) n(T)}{1 - i(\omega - \omega_a) T_2} \quad (2.3.7)$$

Substituting Eq. (2.3.7) to Eq. (2.3.4), I can obtain the transition dipole as following:

$$\bar{p}(Z, T) = \frac{1}{2\pi} \int_{-\infty}^{\infty} -\frac{i\mu^2 T_2}{\hbar} \frac{\tilde{A}(Z, \omega - \omega_0) n(T)}{1 - i(\omega - \omega_a) T_2} e^{-i(\omega - \omega_0)T} d\omega \quad (2.3.8)$$

It should be noted that no approximation or assumption are included in the derivation of Eq. (2.3.8). Thus, Eq. (2.3.8) is only an alternative representation of Eq. (2.3.2). Thus, Eq. (2.3.8) can be substituted to Eq. (2.3.3) and I integrate Eq. (2.3.3) to find a saturated value of the population inversion when supercontinuum pulse absorbed by gain ions.

At a steady state of the population inversion, the change of the population inversion should be zero, which leads that  $n(T_0 + T_R) = n(T_0)$ . Thus, I will derive  $n(T_0)$  satisfying  $n(T_0 + T_R) = n(T_0)$  as following:

## Chapter 2. Numerical model of ultrafast optics in active & nonlinear media

$$n(T_0 + T_R) - n(T_0) = \int_{T_0}^{T_0 + T_R} \frac{\partial n}{\partial T} dT = \int_{T_0}^{T_0 + T_R} -\frac{1}{T_1^*} (n - n_{eq}) dT + \int_{T_0}^{T_0 + T_R} \Phi dT, \quad (2.3.9)$$

where  $\Phi(Z, T) = \frac{2vi(A\bar{p}^* - A^*\bar{p})}{\hbar}$ . For the time interval  $[T_0, T_0 + T_p]$ ,

the first term is negligible since the pulse width is much smaller than  $T_1^*$  and  $T_R$ . For the integration of the second term, I first integrate  $A\bar{p}^*$  as following:

$$\begin{aligned} & \int_{T_0}^{T_0 + T_R} dT A\bar{p}^* \\ &= \int_{T_0}^{T_0 + T_R} dT \left[ \frac{1}{2\pi} \int_{-\infty}^{\infty} d\omega_1 \tilde{A}(Z, \omega_1 - \omega_0) e^{-i(\omega_1 - \omega_0)T} \right] \\ & \quad \times \left[ \frac{1}{2\pi} \int_{-\infty}^{\infty} d\omega_2 \frac{i\mu^2 T_2}{\hbar} \frac{\tilde{A}^*(Z, \omega_2 - \omega_0) n(T)}{1 + i(\omega_2 - \omega_a) T_2} e^{i(\omega_2 - \omega_a)T} \right] \quad (2.3.10) \\ &= \frac{1}{(2\pi)^2} \int_{-\infty}^{\infty} \int_{-\infty}^{\infty} d\omega_1 d\omega_2 \frac{i\mu^2 T_2}{\hbar} \frac{\tilde{A}(Z, \omega_1 - \omega_0) \tilde{A}^*(Z, \omega_2 - \omega_0)}{1 + i(\omega_2 - \omega_a) T_2} \\ & \quad \times \left[ \int_{T_0}^{T_0 + T_R} dT \exp(-i(\omega_1 - \omega_2)T) n(T) \right] \end{aligned}$$

If I consider the lower pulse energy (e.g. pJ to nJ) compared to saturation energies of rare earth ions usually doped in active fibers (e.g.  $\sim \mu\text{J}$  for Er and Yb ions), a variation of the population inversion induced by a single pulse usually have an order of  $10^{-6}$ , which is negligible. Thus, I can assume that the change of the population inversion is negligible for the time interval of  $[T_0, T_0 + T_R]$  and the last term of the integrand of Eq. (2.3.10) can be simplified as

## Chapter 2. Numerical model of ultrafast optics in active & nonlinear media

$$\begin{aligned}
& \int_{T_0}^{T_0+T_R} dT \exp(-i(\omega_1 - \omega_2)T) n(T) \\
& \approx n(T_0) \int_{T_0}^{T_0+T_R} dT \exp(-i(\omega_1 - \omega_2)T) \\
& = n(T_0) T_R \text{sinc}\left((\omega_1 - \omega_2) \frac{T_R}{2}\right) e^{-i(\omega_1 - \omega_2)\left(T_0 + \frac{T_R}{2}\right)}. \\
& \approx 2\pi n(T_0) \delta(\omega_1 - \omega_2) e^{-i(\omega_1 - \omega_2)\left(T_0 + \frac{T_R}{2}\right)}
\end{aligned} \tag{2.3.11}$$

Typical fiber lasers have repetition rate of MHz ( $1/T_R$ ) and supercontinuum generation and supercontinuum spectra bandwidth are broader than THz. Thus, the above *sinc* function can be approximated as Dirac-delta function with respect to frequency.

Substituting Eq. (2.3.11) to Eq. (2.3.10),

$$\int_{T_0}^{T_0+T_R} dT A \bar{p}^* = \frac{1}{2\pi} \int_{-\infty}^{\infty} d\omega \frac{i\mu^2 T_2}{\hbar} \frac{|\tilde{A}(Z, \omega - \omega_0)|^2}{1+i(\omega - \omega_a)T_2} n(T_0). \tag{2.3.12}$$

Then, the second term of Eq. (2.3.9) can be calculated as

$$\begin{aligned}
\int_{T_0}^{T_0+T_R} \Phi dT &= -\frac{2v\mu^2 T_2}{\hbar^2} \frac{1}{2\pi} \int_{-\infty}^{\infty} \left[ \frac{1}{1+i(\omega - \omega_a)T_2} + \frac{1}{1-i(\omega - \omega_a)T_2} \right] |\tilde{A}(Z, \omega - \omega_0)|^2 n(T_0) d\omega \\
&= -\frac{1}{E_{sat}} \frac{1}{2\pi} \int_{-\infty}^{\infty} \frac{S(Z, \omega - \omega_0) n(T_0)}{1+(\omega - \omega_a)^2 T_2^2} d\omega \\
&= -\frac{E_{pulse}^{eff}}{E_{sat}} n(T_0)
\end{aligned} \tag{2.3.13}$$

In the above derivation, the effective pulse energy,  $E_{pulse}^{eff}$  means an effectively absorbed pulse energy by gain ions within gain bandwidth, which is expressed as  $E_{pulse}^{eff} = \frac{1}{2\pi} \int_{-\infty}^{\infty} \frac{S(Z, \omega - \omega_0)}{1+(\omega - \omega_a)^2 T_2^2} d\omega$ ,

where  $S(Z, \omega - \omega_0)$  is an energy spectral density at  $Z$ , such that

$$E_{pulse} = \frac{1}{2\pi} \int_{-\infty}^{\infty} S(Z, \omega - \omega_0) d\omega. \quad \text{The energy spectral density is}$$

## Chapter 2. Numerical model of ultrafast optics in active & nonlinear media

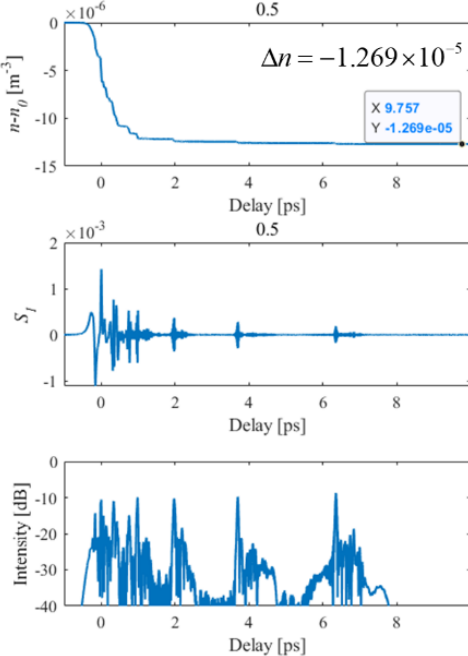
$S(Z, \omega - \omega_0) = 2nc\epsilon_0 |\tilde{A}(Z, \omega - \omega_0)|^2$ . Finally, the saturated population inversion can be obtained as

$$n(T_0 + T_R) - n(T_0) \approx -\frac{T_R}{T_1^*} (n(T_0) - n_{eq}) - n(T_0) \frac{E_{pulse}^{eff}}{E_{sat}} \approx 0. \quad (2.3.14)$$

where  $n_{sat} = \frac{n_{eq}}{1 + \frac{N^* E_{pulse}^{eff}}{E_{sat}}}$ ,  $E_{pulse}^{eff} = \frac{1}{2\pi} \int_{-\infty}^{\infty} \frac{2nc\epsilon_0 |\tilde{A}(Z, \omega - \omega_a)|^2}{1 + (\omega - \omega_a)^2 T_2^2} d\omega$ , and

$N^* = \frac{T_1^*}{T_R}$ . Consequently, the derived equation, Eq. (2.3.14) yields the

same result with the numerical solution of Maxwell–Bloch model as shown in Fig. 2.2.7.



Theoretical calculation (1)

$$E_{pulse} = \frac{1}{2\pi} \int_{-\infty}^{\infty} |\tilde{A}|^2 d\omega$$

$$\Delta n = -7.4777 \times 10^{-5}$$

Theoretical calculation (2)

$$E_{pulse} = \frac{1}{2\pi} \int_{\omega_a - \frac{\Gamma_a}{2}}^{\omega_a + \frac{\Gamma_a}{2}} |\tilde{A}|^2 d\omega$$

$$\Delta n = -0.977 \times 10^{-5}$$

Theoretical calculation (3) ✓

$$E_{pulse} = \frac{1}{2\pi} \int_{-\infty}^{\infty} \frac{|\tilde{A}|^2}{1 + (\omega - \omega_a)^2 T_2^2} d\omega$$

$$\Delta n = -1.2789 \times 10^{-5}$$

Fig. 2.2.7. Change of the population inversion during amplification of supercontinuum pulse and validity of Eq. (2.3.14).

## Chapter 3

# SCG and bright soliton dynamics in gain–embedded highly nonlinear photonic crystal fibers with AD

### 3.1. Background of the study

Supercontinuum generation (SCG) is an extensive spectral broadening process by interplay of linear dispersion and nonlinear optical effects such as self–phase modulation (SPM), four–wave mixing (FWM), Raman scattering, and self–steepening [12, 33, 34]. In fact, the advent of photonic crystal fibers (PCFs) has remarkably improved the SCG technology thanks to their easy engineering of nonlinearity and group velocity dispersion [48]. The SC radiation generated via a PCF has a wide, flat, and smooth spectrum with high spatial coherence, so that it is widely used in numerous application fields such as microscopy [49], optical sensors [50], optical

coherence tomography [51], and biomedicine [52]. While various studies have been conducted on the development of an SC source to improve its bandwidth (BW), coherence, and spectral flatness, etc., their main focus has been, more or less, either on developing a novel-type PCF or on exploiting a novel-type pump source [12, 37, 53]. In particular, the development of a novel-type PCF for SCG applications has so far emphasized on engineering its passive characteristics including dispersion and nonlinearity [12]. However, in recent years SCG based on an active-type optical fiber (i.e. a fiber doped with active rare-earth ions) has drawn a significant level of attention for its novel characteristics that cannot be obtained by means of a passive-type PCF, which include its extended power scalability and spectral broadening controllability while maintaining high spectral flatness and temporal coherence [37, 39, 54–58]. Taking advantage of both high optical gain and high nonlinearity of such a fiber, an experimental study on SCG using a highly nonlinear erbium-doped optical fiber seeded by 11-ps optical pulses has recently been reported [39]. In this work, high optical gain per unit length ( $> 10$  dB/m on average) and high spectral broadening per unit length ( $\sim 350$  nm/m on average) were demonstrated. On the other hand, an extensive numerical study on SCG in an ytterbium (Yb)-doped highly-nonlinear photonic crystal fiber (HNL–PCF) with flattened all-normal dispersion (FAND) seeded by sub-ps ultrafast optical pulses has also been reported [37]. This recent work, as the first theoretical attempt to explain

optical gain effects on SCG in the sub-ps ultrafast pulse regime, verified that optical gain can substantially enhance average energy spectral density (AESD) of SC radiation without significantly degrading its spectral flatness and BW. I stress that utilizing an active-type PCF can open up new possibilities for extended power-scaling and controlled spectral broadening of SCG whilst this recent investigation was just limited to the case of FAND [37].

On this background, I think that it is necessary to extend the recent investigation on an active HNL–PCF to the case with anomalous dispersion (AD). However, it is noteworthy that extension of the discussion to the case in the AD regime is not straightforward from the viewpoint of theoretical frameworks: SCG mechanisms in the AD regime are substantially different from those in the FAND regime [33, 37], because SCG in the AD regime tends to trigger sub-ps input pulses to form even shorter pulses, i.e., sub-100-fs solitons as well as dispersive waves (DWs) owing to soliton fission. This aspect contrasts with the case in the FAND regime, in which the input pulse shape is more or less preserved without undergoing any radical changes and evolutions [33, 37]. Thus, if optical gain is involved in SCG in an active HNL–PCF with AD, ultrafast solitons and DWs become to interact with rare-earth ions on very rapid timescales, so that the related SCG dynamics must be treated and analyzed in a drastically different way from the case of SCG in the FAND regime [37]. That is, the rate-equation-based approach utilized in [9] might be no longer appropriate

enough for such extremely fast nonlinear interactions in the AD regime. I note that to date only a handful of numerical or theoretical studies have been carried out on analyzing novel characteristic aspects of SCG in active fibers in the AD regime [54, 59, 60]. In particular, Lei et al. reported that SCG in a Yb-doped fiber (YDF) with AD can be modeled by combining the well-known rate equation and the nonlinear Schrödinger equation (NLSE) when excited by ps pulses [54]. However, it remains questionable to apply the given method to the rigorous analysis of SCG in the sub-100-fs regime, because the interactions between active ions and sub-100-fs ultrafast solitons, which inevitably arise during the SCG process in the AD regime, cannot be modeled properly based on the standard rate equation method. In other words, the standard rate equation method cannot take account of the quantum coherence effects of excited ions, which become non-negligible for the case having timescales within their dipole relaxation time (e.g.,  $T_2 \sim 16$  fs for Yb ions) [4, 61]. In addition, Arteaga-Sierra et al. reported soliton dynamics in fiber amplifiers, using the complex Ginzburg-Landau equation (CGLE) along with a real-valued super-Gaussian gain spectrum [59]. Although this work focused on the soliton generation in a cascade way and the related pulse dynamics during amplification of low soliton number pulses (i.e.  $N < 1$ ), it did not fully investigate optical gain effects in the context of SCG, the resultant characteristics of which are, in general, quantified by BW, AESD, and spectral flatness, etc. Thus, a comprehensive theoretical

study of SCG in an active HNL–PCF with AD in the sub–ps (or sub–100–fs) regime has yet to be carried out, which will eventually unveil further aspects of an active HNL–PCF operating in the AD regime.

Here, in this study I theoretically analyze SCG in an active HNL–PCF with AD seeded by sub–ps optical pulses at a near–zero–dispersion wavelength. In order for properly dealing with sub–100–fs solitons generated by soliton fission during SCG in the AD regime, ultrafast interactions between solitons and active ions are to be described in a semi–classical approach, which is based on the generalized CGLE (GCGLE) derived by combining the NLSE and the Maxwell–Bloch equations (MBEs) in the semi–classical limit [4, 61–63]. Based on this theoretical model, I numerically simulate SCG in an active HNL–PCF with AD, and show how the interplay among optical gain, nonlinear effects, and dispersion determines SCG evolution and the related soliton dynamics. Moreover, I numerically demonstrate that an active HNL–PCF with AD can be utilized as a novel external booster amplifier for a soliton–based SC source. (It should be noted that the research results described in this chapter is under consideration for publication in IEEE Journal of Quantum Electronics [64].)

## 3.2. Numerical model and methods

### 3.2.1. Numerical model

I here consider a conceptual schematic of SCG seeded with sub-ps pulses in an active HNL-PCF as illustrated in Fig. 3.2.1. I assume that the active dopants are based on rare-earth ions and the input laser operates in the sub-ps regime with a repetition rate in the MHz range [37]. Because of the short duration of the input pulses, they can evolve in the HNL-PCF under considerable influence of group velocity dispersion and various nonlinear optical effects such as SPM, FWM, Raman scattering, and self-steepening. At the same time, the sub-ps optical pulses propagating in the active HNL-PCF are supposed to be amplified by gain ions during the SCG process. In other words, the input pulses evolve under complex interactions of dispersion, nonlinearity, and optical gain effects.

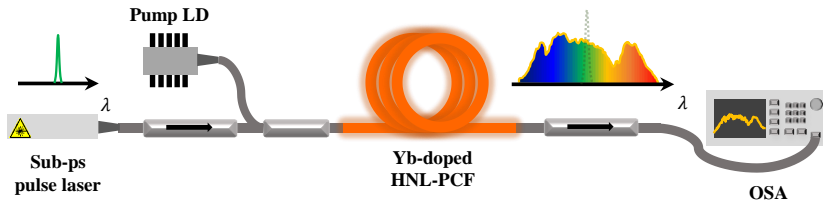


Fig. 3.2.1. Conceptual schematic of SCG in an Yb-doped active HNL-PCF.

LD: Laser diode, OSA: Optical spectrum analyzer.

In general, SCG dynamics involving linear dispersion and various nonlinear effects is described by the NLSE [1], whereas quantum-coherent amplification dynamics in an active medium within very short timescales (e.g., as short as  $T_2$  time) is described by the MBEs [4, 61, 62]. Thus, a self-consistent equation set

encompassing the NLSE and the MBEs can surely be a governing master equation set for pulse evolution under effects of dispersion, nonlinearity, and coherent amplification. In fact, the NLSE–MBE equation set is expressed as follows:

$$\begin{aligned} \frac{\partial A}{\partial Z} = & -\frac{\alpha}{2}A - \sum_{m=2}^{\infty} \frac{i^{m-1} \beta_m}{m!} \frac{\partial^m A}{\partial T^m} + i\gamma_Q N_{tot} p \\ & + i\gamma \left( 1 + \tau_{shock} \frac{\partial}{\partial T} \right) A(Z, T) \int_{-\infty}^{\infty} R(T') |A(Z, T - T')|^2 dT', \end{aligned} \quad (3.2.1)$$

$$\frac{\partial p}{\partial T} = \left( -\frac{1}{T_2} - i\Delta_a \right) p - \frac{i\mu^2}{\hbar} An, \quad (3.2.2)$$

$$\frac{\partial n}{\partial T} = -\frac{1}{T_1^*} (n - n_{eq}) + \frac{i(Ap^* - A^* p)}{\hbar}, \quad (3.2.3)$$

where  $A$ ,  $p$ , and  $n$  denote the envelope of the optical field, the transition dipole moment, and the normalized population inversion, respectively;  $Z$  and  $T$  denote the propagation distance and the time coordinate in the co-moving frame at the envelope group velocity;  $\alpha$ ,  $\beta_m$ , and  $\gamma$  denote the attenuation, the  $m$ -th order dispersion, and the nonlinear coefficients;  $\tau_{shock}$  denotes the shock coefficient for self-steepening, which is usually characterized by the inverse of the center angular frequency (i.e.,  $1/\omega_0$ ). The nonlinear response function is expressed by  $R(T) = (1-f_R)\delta(T) + f_R h_R(T)$ , which includes SPM and Raman response, where  $f_R$  is usually given by 0.2 for typical silica fibers (see [37] for details of the Raman response function). As for the dopant parameters,  $\gamma_Q$  denotes the polarization coupling constant,  $N_{tot}$  the number density of dopants,  $T_2$  the dipole relaxation time,  $\Delta_a$  the frequency offset of the center frequency of

the optical pulses from the amplification frequency  $\omega_a$ , and  $\mu$  the transition dipole moment.  $T_1^*$  and  $n_{eq}$  denote the effective spontaneous decay time (or the effective pumping time) and the population inversion at equilibrium, which are dependent on pumping rate  $R_p$  and the spontaneous decay time  $T_1$ . It is noteworthy that Eqs. (3.2.2) and (3.2.3) are derived, under an assumption that Yb ions have a four-level energy structure:  $T_1^*$  and  $n_{eq}$  are thus expressed as  $T_1^* = T_1/(R_p T_1 + 1)$  and  $n_{eq} = R_p T_1 / (R_p T_1 + 1)$  [47].

However, without loss of generality it is known that in the case of a fiber-optic gain medium of rare-earth ions, the Bloch vector does not change much in the vertical direction even when considering coherent interactions between optical fields and gain ions [65]. This applies to our case, because the soliton energy level of interest, which is typically in a pico-joule order, is much smaller than the saturation energy of gain ions, which is typically in a micro-joule order. Consequently, the amount of the normalized population inversion change during coherent amplification becomes nearly negligible [62, 65]. In fact, it has been reported that its typical change is quantified as small as below  $10^{-5}$  in room-temperature conditions [66]. Thus, in this limit I readily derive the GCGLE from the NLSE–MBE set as follows (see [65] for details of the derivation):

$$\begin{aligned}
 \frac{\partial A}{\partial Z} = & -\frac{\alpha}{2} - \sum_{m=2}^{\infty} \frac{i^{m-1} \beta_m}{m!} \frac{\partial^m A}{\partial T^m} + i\gamma \left( 1 + \tau_{\text{shock}} \frac{\partial}{\partial T} \right) A(Z, T) \int_{-\infty}^{\infty} R(T') |A(Z, T - T')|^2 dT' \\
 & + \frac{1}{2\pi} \frac{g}{2} \int_{-\infty}^{\infty} \frac{\tilde{A}(Z, \omega - \omega_0)}{1 - i(\omega - \omega_a)T_2} e^{-i(\omega - \omega_a)T} d\omega.
 \end{aligned}$$

(3.2.4)

In Eq. (3.2.4), the saturated gain coefficient  $g$  is given by  $g = g_{us} / (1 + N^* E_{pulse}^{eff} / E_{sat})$ , where  $N^*$  is the number of pulses that pass through gain ions over the time  $T_1^*$  with a repetition rate of  $1/T_R$ , and  $g_{us}$  is the unsaturated gain coefficient expressed as  $\sigma_s N_{tot} n_{eq}$ . I note that both  $T_1^*$  and  $g_{us}$  depend on the pumping rate. During the derivation of Eq. (3.2.4), the effectively absorbed pulse-energy  $E_{pulse}^{eff}$  is obtained as [65]:

$$E_{pulse}^{eff} = \frac{1}{2\pi} \int_{-\infty}^{\infty} \frac{|\tilde{A}(Z, \omega - \omega_0)|^2}{1 + (\omega - \omega_a)^2 T_2^2} d\omega. \quad (3.2.5)$$

It is noteworthy that transient responses of gain ions for ultrafast pulses described in Eq. (3.2.2) are sufficiently taken into account in the derivation of Eqs. (3.2.4) and (3.2.5), which are, however, completely ignored in the rate-equation-based approximation [67]. I stress that Eq. (3.2.5) indeed exhibits an important aspect of the ultrafast interactions between broadband SC radiation and gain ions: It tells how the effectively absorbed pulse energy is estimated when the spectral BW of the input pulses is significantly larger than that of gain ions: The contributions of the spectral components of the input pulses outside the gain BW are taken into account via the weighting function as given in the denominator of Eq. (3.2.5). This plays a critical role in properly describing the gain saturation effect by the repetitive ultrafast SC pulses [65]. Otherwise, the coherent absorption of the input SC pulses by gain ions might considerably be overestimated [65].

I now investigate SCG in an HNL–PCF having AD. It is launched by input pulses centered at 1064 nm having a hyperbolic secant profile such as  $A(T) = P_0^{1/2} \operatorname{sech}(T/T_0)$  with a 176-fs pulse duration (full width at half maximum: FWHM) and a 0.6-nJ pulse energy, which correspond to a 3.0-kW peak power and a soliton number  $N$  of 9. I assume the passive parameters of the HNL–PCF as follows: The fiber length  $L$  is in the range of around 1 m. The fiber dispersion coefficients at 1064 nm are given by  $\beta_2 = -11.2 \text{ ps}^2/\text{km}$ ,  $\beta_3 = 8.0 \times 10^{-2} \text{ ps}^3/\text{km}$ ,  $\beta_4 = 9.9 \times 10^{-5} \text{ ps}^4/\text{km}$ ,  $\beta_5 = 1.2 \times 10^{-7} \text{ ps}^4/\text{km}$ , and  $\beta_6 = 4.0 \times 10^{-11} \text{ ps}^5/\text{km}$ , which result in AD with a negative slope at around 1064 nm and the zero-dispersion wavelength (ZDW) at 975 nm [57]. The fiber attenuation is low enough to be ignored, taking account of the short fiber length. The fiber nonlinear coefficient  $\gamma$  is given by  $29 \text{ W}^{-1}\text{km}^{-1}$ . On the other hand, I assume the active parameters of the HNL–PCF as follows: When operating in non-zero gain, the fiber gain is based on excited Yb ions, matched for the amplification of the input pulses centered at 1064 nm. The spontaneous decay time  $T_1$  and the dipole relaxation time  $T_2$  of the Yb ions are given by 0.8 ms and 16 fs, respectively [24, 37]. The latter yields the Yb ions’ gain BW of 20 THz. The unsaturated gain coefficient  $g_{us}$  of the active HNL–PCF is set to 40 dB/m, thereby being capable of resulting in the overall energy gain at the fiber end of  $\sim 10$  dB along with the other given parameters. I note that the unsaturated gain coefficient corresponds to a core absorption rate of 178 dB/m at 976 nm, which is readily

achievable with current fiber fabrication techniques [68]. The effective saturation energy per single-pulse denoted as  $E_{sat}/N^*$  is set to 3 nJ, which is a typical value for a Yb-doped fiber amplifier with a MHz-level repetition rate [37]. I summarize all the parameters in Table 1, which will remain unchanged unless stated otherwise. Finally, I solve Eqs. (3.2.4) and (3.2.5) by utilizing the 4-th-order Runge–Kutta method in the Fourier domain [69], for which I determine the number of grids and the time window size to be  $2^{15}$  and 90 ps, respectively, allowing for both SC radiation’s temporal and spectral spreads to fit into the time and frequency windows of 360 THz. I calculate the spectral flatness measure (SFM) of the calculated SC radiation utilizing the formula specified in [53].

**Table 3.2.1. Simulation parameters.**

Parameter	Value	Parameter	Value
$\beta_2$ [ps <sup>2</sup> /km]	-11.2	$g_{us}$ [dB/m]	0 ~ 40
$\beta_3$ [ps <sup>3</sup> /km]	$8.0 \times 10^{-2}$	$T_1$ [ms]	0.8
$\beta_4$ [ps <sup>4</sup> /km]	$9.9 \times 10^{-5}$	$T_2$ [fs]	16
$\beta_5$ [ps <sup>5</sup> /km]	$1.2 \times 10^{-7}$	$E_{sat}/N^*$ [nJ]	3
$\beta_6$ [ps <sup>6</sup> /km]	$4.0 \times 10^{-11}$	$P_0$ [kW]	1 ~ 10
$\gamma$ [W <sup>-1</sup> km <sup>-1</sup> ]	29	$T_0$ [fs]	100
$L$ [m]	0.74 ~ 1.60		

### 3.2.2. Numerical methods

The GCGLE can be solved via the 4th-order Runge–Kutta method in Fourier domain. To apply the numerical method, the

time–domain GCGLE (Eq. (3.2.4)) should be transformed to the Fourier–domain GCGLE as following:

$$\frac{\partial \tilde{A}}{\partial Z} - \hat{L}\tilde{A} = \gamma \frac{\omega}{\omega_0} \tilde{\phi}(Z, \omega - \omega_0) + \frac{g}{2} \frac{1}{1-i(\omega-\omega_a)T_2} \tilde{A}(Z, \omega - \omega_0) \quad (3.2.6)$$

where  $\tilde{A}$  is a Fourier transform of  $A$ ,  $\hat{L}$  is a linear operator that acts as a fiber dispersion, and  $\tilde{\phi}$  is a Fourier transform of nonlinear function of  $A$ .  $\hat{L}$  and  $\tilde{\phi}$  are expressed as following:

$$\hat{L} = i \sum_{m=2}^{\infty} \frac{\beta_m}{m!} (\omega - \omega_0)^m \quad (3.2.7)$$

and

$$\phi(Z, T) = A(Z, T) \int_0^{\infty} R(T') |A(Z, T - T')|^2 dT' \quad (3.2.8)$$

The term including the linear operator  $\hat{L}$  in Eq. (3.2.6) can be eliminated by introducing  $\tilde{A} = \exp(-\hat{L}Z) \tilde{A}'$ . Then, one obtains the simple ordinary differential equation, which is readily solvable utilizing the 4th–order Runge–Kutta method.

$$\frac{\partial \tilde{A}'}{\partial Z} = \gamma \frac{\omega}{\omega_0} \tilde{\phi}(Z, \omega - \omega_0) \exp(-\hat{L}Z) + \frac{g}{2} \frac{1}{1-i(\omega-\omega_a)T_2} \tilde{A}(Z, \omega - \omega_0) \exp(-\hat{L}Z) \quad (3.2.9)$$

### 3.3. Gain effects and soliton dynamics on SCG in the AD regime

#### 3.3.1. Gain effects on in the AD regime

I first investigate the gain effects on SCG in the HNL–PCF with

AD specified in the preceding section, comparing two distinct cases: One is the case when the HNL–PCF works as a passive (undoped) fiber, i.e.,  $g_{us} = 0$  dB/m, as similar as the passive PCFs with AD reported in the literature [12, 33, 34, 70]. The other is the case when it works as an active fiber with  $g_{us} = 40$  dB/m. I note that all the fiber parameters except the gain coefficient are the same for both cases as specified in the preceding section, and that the fiber length is set identically to 1.6 m for both cases. I numerically analyze both cases based on Eqs. (3.2.4) and (3.2.5), and plot the temporal and spectral evolutions of the corresponding SC radiation in Figs. 3.3.1(a)–1(d). I also calculate 20-dB BWs and AESDs of them with respect to propagation distance in Figs. 3.3.1(e) and 1(f). I note that the AESD is given by the mean energy spectral density within 20-dB BW of the given SC radiation. When the HNL–PCF works as a passive fiber as shown in Fig. 3.3.1(c), one can see that the input pulse ( $N = 9$ ) undergoes the typical soliton fission process such that the input pulse splits into multiple fundamental solitons, generating DWs. The DWs are phase-matched with the corresponding fundamental solitons. These DWs are commonly known as non-solitonic radiation (NSR) or Cherenkov radiation [34]. The emitted solitons undergo deceleration, being red-shifted by Raman scattering. Time delays of these solitons continually increase, eventually giving rise to collisions with the DWs in the normal dispersion (ND) region. The DWs are then trapped by the decelerating Raman solitons, being blue-shifted under the phase

and group–velocity matching conditions with the corresponding Raman solitons [34, 70]. Consequently, the resultant SC spectrum is extensively broadened by the Raman solitons and DWs as shown in Fig. 3.3.1(a). However, I note that as the solitons are consecutively released from the input pulse, its effective soliton number gradually decreases. Thus, once the effective soliton number has become less than unity, the soliton fission process is eventually terminated [12]. In contrast, when the optical gain is turned on, the dynamics associated with soliton fission becomes substantially different from that of the passive case: The ‘pulse remnant’ [59], which is the part of the input pulse remaining after the soliton fission or breakup at  $z = 0.07$  m, continues to emit fundamental solitons as shown in Fig. 3.3.1(d). This is since it can continually gain extra energy via the amplification process by excited gain ions, being able to be recovered from the energy loss by emitting solitons. As a result, the recovered pulse remnant can keep emitting fundamental solitons more frequently and extensively, being red–shifted and spreading widely over the AD frequency region by Raman scattering in the fiber. In addition, the DWs generated under the phase and group–velocity matching conditions with the solitons are also widely distributed over the ND frequency region. In fact, the high nonlinearity combined with the high gain makes the SC radiation more densely distributed in both time and frequency domains.

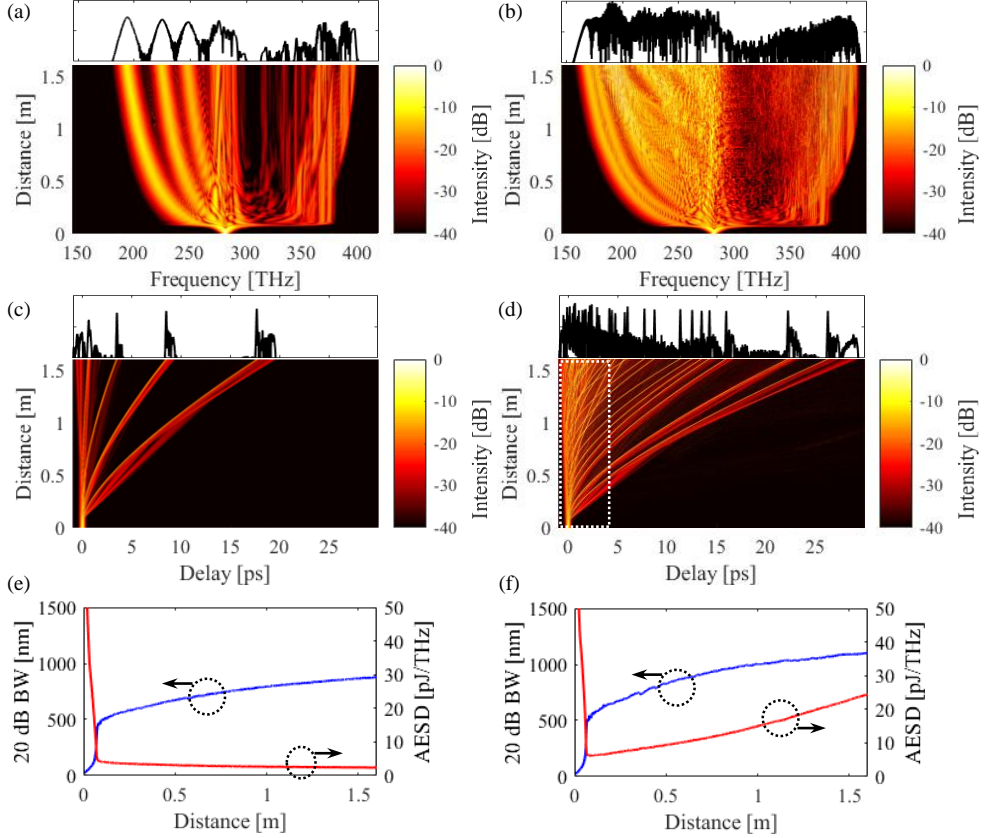


Fig. 3.3.1. Evolutions of SC radiation in passive and active HNL–PCFs. (a) and (b): Spectral evolutions in the passive HNL–PCF ( $g_{us} = 0$  dB/m) and in the active HNL–PCF ( $g_{us} = 40$  dB/m), respectively. (c) and (d): Temporal evolutions in the passive case and in the active case, respectively. (e) and (f): Evolutions of 20–dB BW and AESD in the passive case and in the active case, respectively. Note that the output spectra and temporal traces are put on top of the figures of (a) – (d), respectively.

The impacts of gain effects on the SC radiation are clearly visible in the BW and AESD as shown in Figs. 3.3.1(e) and 1(f). In the passive HNL–PCF case, the BW increases rapidly as the input pulse reaches the soliton–fission length, and then keeps increasing slowly owing to the Raman red–shifts of the emitted solitons and

the blue-shifts of the trapped DWs after the fission length. In this passive case the total energy of the SC radiation obviously remains constant, so that the increase in the BW implies the decrease of the AESD. That is, the AESD rapidly decreases until the fission length, and then keeps decreasing slowly. In contrast, when the optical gain is involved in, the total energy of the SC radiation is no longer constant, thereby being able to increase even during the SCG process. However, I note that the BW does not increase substantially in comparison with the passive case. This is due to the fact that the fission length is as short as  $\sim 0.2$  m in the given conditions, so that the soliton number of the input pulse cannot grow substantially in such a short distance. In other words, the frequency red-shift of the first emitted soliton, which crucially determines the BW of the generated SC radiation, is not substantially larger than that in the passive case, even though it is surely larger than that in the passive case. As a result, the extra energy supplied into the SC radiation via the amplification process through excited gain ions leads to a substantial amount of increase in the AESD. Whilst the AESD initially decreases until the fission length, it continues to increase afterwards as shown in Fig. 3.3.1(f). This aspect is in stark contrast to the passive case, in which the AESD monotonically decreases through the whole fiber length.

### 3.3.2. Soliton dynamics under the optical gain effect

The detailed soliton formation and dynamics in the active HNL–PCF case are further illustrated in Figs. 3.3.2(a) and (b), which are, in fact, the zoomed-in images of the part enclosed by the rectangle in a white-dashed line in Fig. 3.3.1(d). In Fig. 3.3.2(a), I note that the input pulse breaks up into multiple fundamental solitons, also generating DWs after the soliton fission length. Actually, the pulse remnant is continually amplified by excited gain ions, so that it consecutively emits fundamental solitons every time it has gained sufficient energy to do so by amplification. The fundamental solitons characteristically undergo red-shifts and group delays by Raman scattering. In fact, these features are very similar to those observed in the ‘soliton cascades’ reported in [59], where the dynamics of soliton cascades was numerically studied particularly for the case of the amplification of ultrashort optical pulses having energy less than required to form a soliton of an equal pulse width in an active fiber with moderate gain and moderate nonlinearity parameters. Contrasting to the soliton cascades previously reported [59], I stress that the active HNL–PCF in this current investigation has substantially high gain and high nonlinearity parameters, and that the input pulse also has a substantially high soliton number. Consequently, solitons are generated not only from the leading part of the pulse remnant but also from the trailing part of it, as shown in Fig. 3.3.2(a). Formation of such solitons is further zoomed in Fig. 3.3.2(b): In particular, I note that a new type of pulse starts to form in the region enclosed by the rectangle and ellipse in a white–

dashed line in Fig. 3.3.2(b). Although the pulse is in an intermediate stage before being able to form an ordinary soliton shape from the viewpoint of its spectrogram features shown in Fig. 3.3.2(c), I may well call it a ‘quasi–soliton (QS)’ because it approximately exhibits characteristic features of a soliton, eventually evolving into an ordinary one afterwards, which include continual red–shift and distinct localization in the spectro–temporal domain [71]. These QSs tend to undergo specific group delays by Raman scattering in the given situations, thereby resulting in collisions with nearby ordinary solitons or other QSs, while travelling at different group velocities as illustrated in Fig. 3.3.2(b). Actually, I have analyzed the collision process incurred by one of the QSs in more detail by means of the spectrogram analysis into three different stages of I, II and III [see the inset of the Fig. 3.3.2(b)], and show their temporal and spectral evolutions in Fig. 3.3.2(c) [12]. In Stage I, which is the period before the collision occurs, the soliton at  $\sim 250$  THz (at a low frequency) is initially preceding the QS at  $\sim 270$  THz (at an intermediate frequency). The soliton’s peak power is higher than that the QS’s. By the way, the soliton’s group delay rate is also higher than the QS’s because both are in the AD regime.

Thus, they are gradually coming closer in this stage. In addition, in this stage the trace of the QS represented in the spectrogram has not been localized as clearly as that of the soliton. In Stage II, it is very intriguing to note that a high–frequency DW at  $\sim 370$  THz is generated while the soliton and the QS collide. I cannot explain the

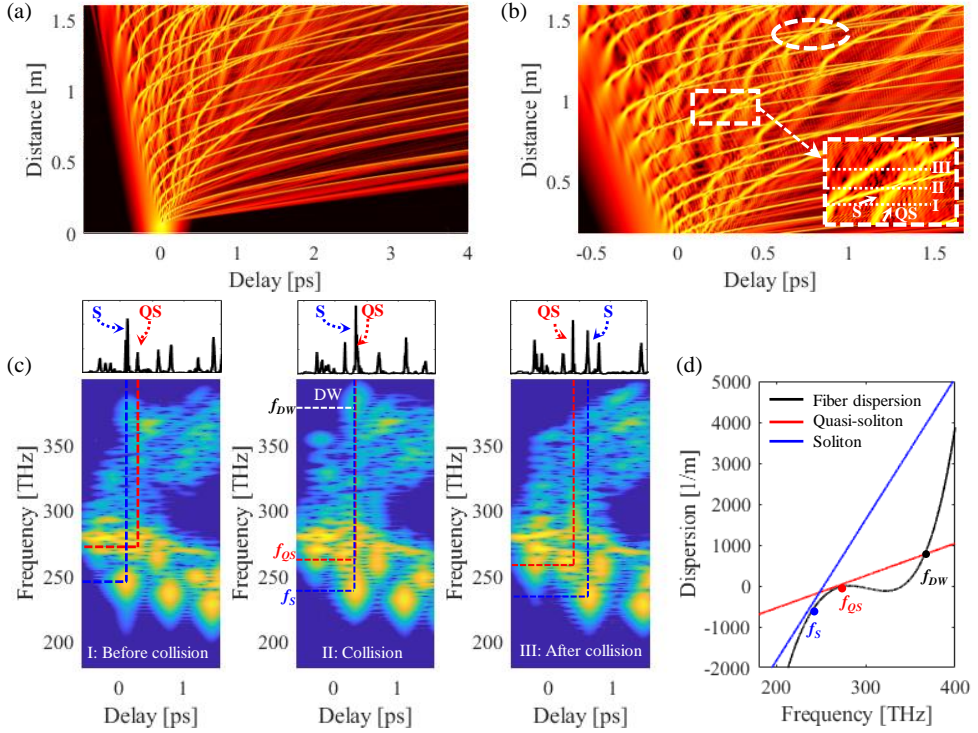


Fig. 3.3.2. Detailed soliton formation and dynamics in the active HNL–PCF.

(a) Zoomed-in image of the part enclosed by the rectangle in a white-dashed line in Fig. 3.3.1(e). (b) Formation of solitons and QSs, and their collision dynamics. The inset is the zoomed-in image of the part enclosed by the rectangle in a white-solid line in (b). (c) Spectrograms and the linear-scale intensity profiles corresponding to Stage I, Stage II, and Stage III. S: Soliton; QS: Quasi-soliton. (d) Dispersion relations of the corresponding soliton, QS, and the HNL–PCF.

frequency of this DW in terms of FWM involving the corresponding soliton and QS. I instead attribute its generation to the consequence of the energy shed from the QS during its transition towards an ordinary soliton after the soliton–QS collision: I have numerically verified it, analyzing the dispersion relations of the corresponding soliton, QS, and the HNL–PCF, as shown in Fig. 3.3.2(d). I note

that the dispersion relation line for the QS intersects that of the HNL–PC approximately at the center frequencies of the QS and the DW given in the Fig. 3.3.2(c), which are also denoted with the solid circles in red ( $f_{QS} = 268$  THz) and in black ( $f_{DW} = 366$  THz) in Fig. 3.3.2(d), respectively. This implies that the DW is indeed likely to be phase–matched with the QS in the HNL–PCF [1, 34]. On the other hand, the dispersion relation line of the soliton seems to intersect that of the HNL–PCF at the even higher frequency ( $f_s = 410$  THz) if I find one for a phase–matched DW. However, it is hard to expect such a case to occur by means of the soliton itself, because it has already been formed as an ordinary soliton even earlier than this stage, thereby only being able to give rise to a very limited energy shed by the soliton–QS collision unless the collision is extremely strong [4, 34]. I confirm that there are no additionally significant spectro–temporal components beyond the range shown in Fig. 3.3.2(c). That is, the phase–matched DW generation by the soliton itself has already occurred while the soliton was initially formed from the input pulse at the even earlier stage, in which the frequency of the soliton was even higher because it had not undergone the corresponding red–shifts by Raman scattering. Anyhow, after the soliton–QS collision, the spectrogram trace of the QS gradually becomes further distinctive in the spectro–temporal domain and eventually turns into that of an ordinary soliton in State III as shown in Fig. 3.3.2(c). I emphasize that generation of these high frequency DWs via soliton–QS collisions is

one of the characteristic features of SCG in an active HNL–PCF with high gain and high nonlinearity. Another astonishing aspect of the soliton dynamics in this active HNL–PCF is that a bunch of solitons and QSSs can collide together at the same time: See the extreme event at  $z = \sim 1.4$  m enclosed by an ellipse in a white-dashed line in Fig. 3.3.2(b). I suspect that this happens because DWs trapped by the soliton pair along with the QSSs are reflected back and forth among them, subsequently pulling them closer to each other [72]. In such an eventful circumstance, one may be able to observe a variety of extreme events, such as optical Newton's cradle dynamics [71], optical rogue wave generation [59, 72–75], and optical event horizon [76], which I however think are beyond the scope of this study and should be dealt with in further detail elsewhere.

### **3.3.3. Spectrogram analysis on gain effects on SCG in AD**

I can see additional impacts of gain effects on the SC radiation when I compare side by side the resultant spectrograms with and without optical gain: Fig. 3.3.3(a) represents the spectrogram with the output snap shots for the temporal intensity and spectral power density profiles in the passive HNL–PCF case, in which only four solitons are generated at AD frequencies along with the corresponding DWs at ND frequencies trapped by the solitons. In contrast, Fig. 3.3.3(b) represents the spectrogram with the output

snap shots for the temporal intensity and spectral power density profiles in the active HNL–PCF case, in which a huge number of solitons and DWs are generated at the same time, forming a soliton cluster densely packed in the range of 0 to  $\sim 10$  ps and the corresponding “sea of DWs”. This feature again signifies that the DWs trapped by the soliton cluster along with QSSs collide back and forth with the number of solitons and QSSs in the cluster, provoking extreme events such that they cover up the temporal and spectral spaces otherwise could have remained nearly empty as in the passive case. This eventually results in a substantial level of improvement in terms of SFM for the output SC radiation as can be noticed in Fig. 3.3.3: I have calculated the SFM values in 20-dB BW for both passive and active cases, which are given by 0.19 and 0.26, respectively.

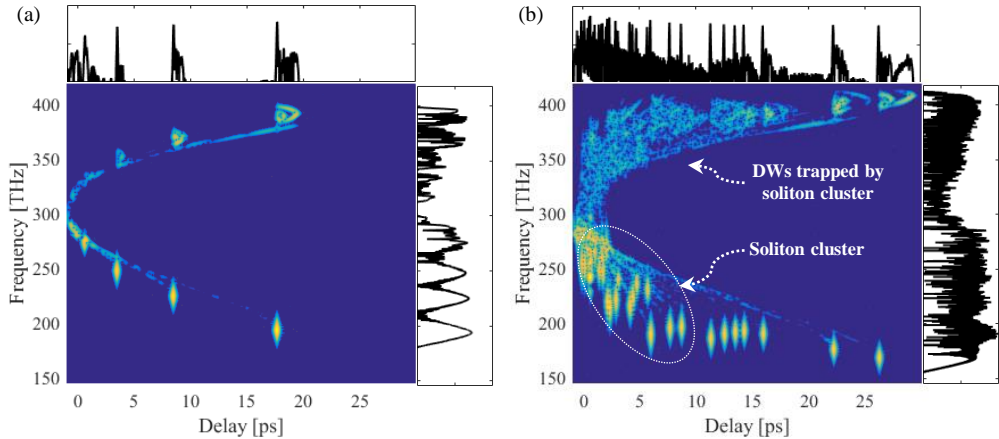


Fig. 3.3.3. Output spectrograms for the passive and active HNL–PCFs. (a) Passive HNL–PCF case ( $g_{us} = 0$  dB/m). (b) Active HNL–PCF case ( $g_{us} = 40$  dB/m).

### 3.4. Comparative analysis of energy–scaling schemes for SCG

In the preceding section, I have verified the novel characteristic features of SCG in an active HNL–PCF with AD in terms of AESD and SFM. However, one may think that scaling of AESD of SC radiation is still possible with a passive HNL–PCF if the input pulse energy is scaled up in advance to the passive HNL–PCF. This can be realized by simply inserting a lumped amplifier between the seed source and the passive HNL–PCF as the cases demonstrated in most SCG experiments [55, 77, 78]. (Alternatively, one may think of direct amplification of the SC radiation obtained after the passive HNL–PCF; however, this cannot be an effective way, because there is no practical amplifier whose gain BW can cope with the huge BW of the SC radiation extending to several hundreds of nanometers [24, 79]. Notwithstanding, I will also investigate this specific situation in the next section.) In this configuration, unlike the active HNL–PCF case, the amplification and SCG processes are separate, thereby taking place one by one. I thus investigate this passive HNL–PCF case with initially energy–boosted input, and compare its characteristics with those of the active HNL–PCF case. For the sake of a fair comparison, I assume that the total energy scaling factors are identically set from 1 to 10 dB in 1 m of fiber length for both cases. In other words, for the former case, I vary the peak power of the input pulse from 1 to 10 kW, which corresponds to the

total energy of the input pulse from 0.2 to 2 nJ. For the latter case, I vary the unsaturated gain coefficient from 0 to 33.4 dB/m with the peak power of the input pulse fixed at 1 kW, which results in exactly the same amounts of the total energy or the total energy scaling factor of the resultant SC radiation as the former case. I note that I keep all other pulse and fiber parameters the same as those used in the preceding section for both cases. I present the corresponding numerical simulation results in Fig. 3.4.1.

As shown in Fig. 3.4.1, even though the total energy of the output SC radiation is the same for both cases, their specific characteristics in terms of BW, AESD, and the number of solitons generated are drastically different. In the former case, as the input peak power increases, the BW of the SC radiation grows considerably as shown in Figs. 3.4.1(a) and (c). This is due to the fact that in the case of SCG pumped at an AD frequency, the BW of the SC radiation is, in principle, determined by how far the first-ejected soliton shifts by Raman scattering [12], which is in turn proportional to the peak power of the input pulse [41]. In contrast, in the latter case, the BW of the SC radiation does not grow as considerably as in the former case. The reason for this consequence is that the peak power of the input pulse cannot grow as immediately as the amplification process by excited gain ions until reaching the fission length as already verified in Fig. 3.3.1(f). For example, if I suppose that the total energy of the SC radiation is scaled up by 10 dB for both cases, the former case results in an

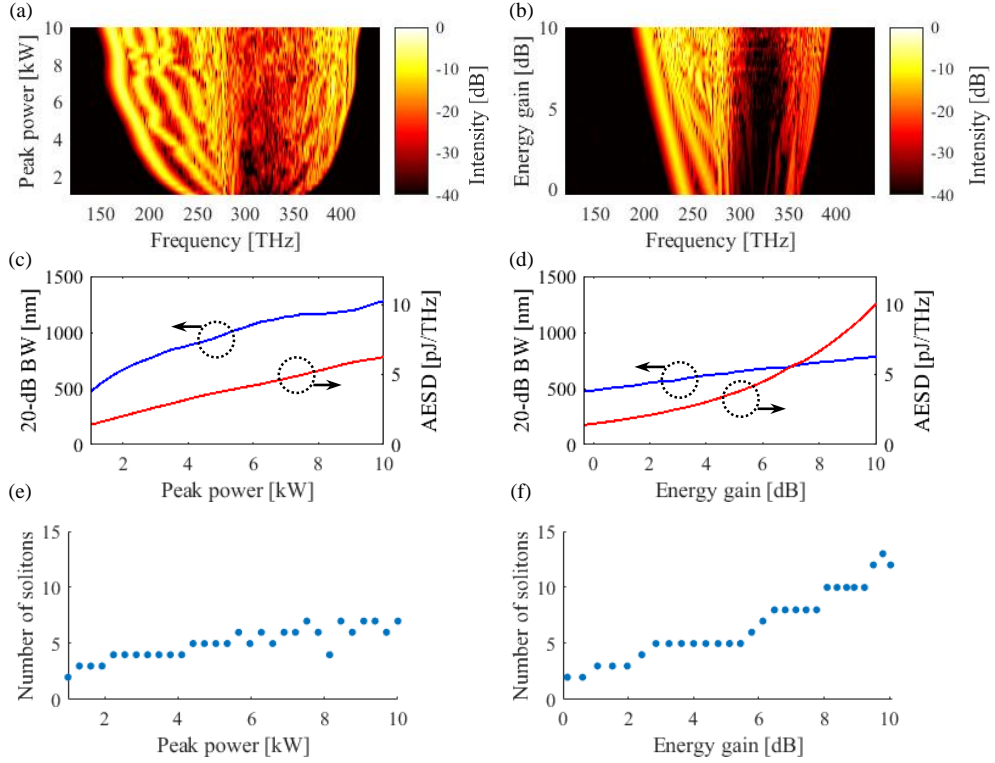


Fig. 3.4.1. Characteristics of the passive HNL–PCF case combined with initially energy–boosted input and the active HNL–PCF case. (a) and (b): Spectral evolutions in the passive HNL–PCF case with initially energy–boosted input and in the active HNL–PCF case, respectively. (c) and (d): Evolutions of 20–dB BW (blue) and AESD (red) in the passive HNL–PCF case with initially energy–boosted input and in the active HNL–PCF case. (e) and (f): Total numbers of solitons generated in the passive HNL–PCF case with initially energy–boosted input and in the active HNL–PCF case, respectively.

immediate 10–dB increase in the peak power of the input pulse whereas in the latter case the total 10–dB energy gain is distributed in the whole SC radiation throughout the whole length of the fiber. Consequently, the peak power of the first–ejected soliton in the latter case cannot be as high as that in the former case. Thus, without loss of generality, the BW growth of the latter case becomes insignificant relative to the former case. Since the total energy of the output SC radiation is assumed to be the same in both cases, the narrower BW implies the higher AESD. Therefore, the AESD through the active HNL–PCF should be by far higher than that through the passive HNL–PCF as shown in Figs. 3.4.1(c) and (d). I highlight that the high energy injected into the passive HNL–PCF by means of the input pulse is used to broaden the BW of the SC radiation, whereas the high energy injected by means of excited gain ions progressively amplifies the SC radiation throughout the whole fiber length, thereby being able to increase the AESD more effectively. The difference of these characteristic features can also be manifested by the number of solitons generated in both cases as shown in Figs. 3.4.1(e) and (f). I note that substantially more solitons are generated in the active case than in the passive case. [In Figs. 3.4.1(e) and (f), the slight fluctuations of the soliton numbers are due to the fact that the solitons that coincidentally collide at the fiber end are counted as one pulse.] In result, I stress that an active HNL–PCF has a clear advantage over its passive counterpart in terms of AESD scaling.

### 3.5. Direct amplification of SC radiation

In the preceding two sections, I have discussed that the distinct characteristic features of SCG via an active HNL–PCF in comparison with its passive counterparts. In this section, making the most of the advantageous features of SCG via an active HNL–PCF, I propose and verify that an active HNL–PCF can also be exploited for amplifying broadband SC radiation that has already been produced via other passive–type PCFs. Perhaps, one may think of the use of a conventional amplifier based on a low–nonlinearity YDF to amplify such SC radiation. However, I should note that the gain BW of Yb ions is limited just to  $\sim 20$  THz, which is far too narrow to amplify the whole SC radiation whose BW can typically go beyond 200 THz. In fact, there are no other practical candidates to deal with such broadband radiation. Thus, it is necessary to exploit the characteristic features of an active HNN–PCF since I have already verified in the preceding section that the high nonlinearity combined with high gain via an active HNL–PCF can extend the gain effects to an even wider spectral range than the nominal gain BW that rare–earth ions can provide. In this regard, I further investigate the functionality of an active HNL–PCF as an external amplifier capable of amplifying broadband SC radiation, in comparison with a conventional amplifier based on a low–nonlinearity YDF. For the sake of a fair comparison, I assume that SC radiation inputs for both cases are identically generated by the

passive HNL–PCF investigated in Section 3.1, the characteristics of which are the same as those already shown in Figs. 3.3.1(a) and 2(c). That is, they identically have a total energy of  $\sim 0.6$  nJ and a 20–dB BW of 792 nm. The nonlinear coefficient of the YDF is set to a typical value of silica–based fibers (i.e.,  $\gamma = 1 \text{ W}^{-1}\text{km}^{-1}$ ). The length of each fiber is determined to yield 10–dB energy gain for each case for a fair comparison, so that the YDF and the active HNL–PCF lengths are given by 0.74 and 1.40 m, respectively. All other fiber parameters remain the same as in the preceding sections.

The spectral evolution and the output spectrum of the SC radiation amplified by the YDF are shown in Fig. 3.5.1(a), which indicates that the amplified SC radiation considerably loses its initial BW because only a fraction of the SC radiation that lies within the gain BW of Yb ions ( $\sim 20$  THz) is amplified. This consequence in turn gives rise to substantial degradation in SFM as shown in Fig. 3.5.1(c). The SFM values within 20–dB BW for the SC radiation before and after amplification are calculated to be 0.24 and 0.04, respectively. In contrast, the output SC radiation amplified by the active HNL–PCF yields very promising outcomes in terms of BW and SFM as shown in Fig. 3.5.1(d): The BW further increases by a small amount owing to the extra red–shift of the first–emitted soliton by Raman scattering, and it still produces a flat SC radiation, maintaining nearly the same SFM as the original value. The SFM values in 20–dB BW before and after amplification are calculated to be 0.24 and 0.25, respectively. These characteristics are superior

to those with the conventional YDF case. In this light, an active HNL–PCF with AD should be a good candidate for an external amplifier for soliton–based SC radiation since it can scale up the power of SC radiation without incurring degradation of SFM as in the case of an active HNL–PCF with FAND for amplifying coherent SC radiation [37].

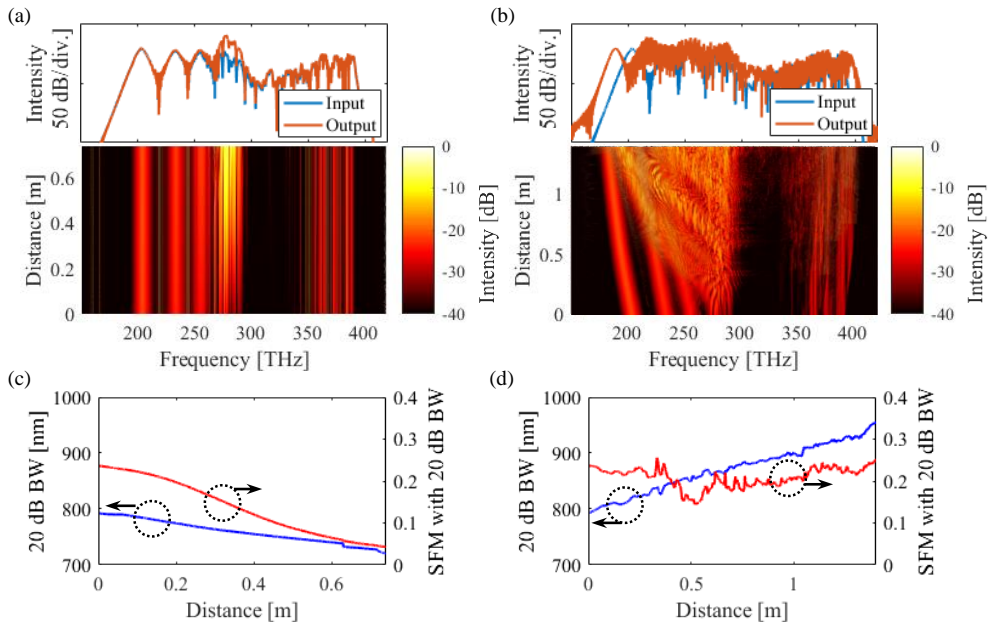


Fig. 3.5.1. Characteristics of the passive HNL–PCF case combined with a conventional amplifier based on a low–nonlinearity YDF and the active HNL–PCF case. (a) and (b): Spectral evolutions in the passive HNL–PCF case combined with a conventional amplifier based on a low–nonlinearity YDF and in the active HNL–PCF, respectively. (c) and (d): Evolutions of 20–dB BW (blue) and SFM (red) within the 20–dB BW in the passive HNL–PCF case combined with a conventional amplifier based on a low–nonlinearity YDF and in the active HNL–PCF, respectively.

# Chapter 4

## SCG and dark soliton dynamics in gain–embedded highly nonlinear photonic crystal fibers with FAND

### 4.1. Background of the study

#### 4.1.1. Conventional SCG techniques based on soliton dynamics

Supercontinuum (SC) generation (SCG) is a nonlinear spectral broadening process caused by Kerr nonlinearity and dispersion interactions such as self–phase modulation (SPM), four–wave mixing (FWM), Raman scattering, and self–steepening [12, 33, 80]. In fact, with the advent of photonic crystal fiber (PCF) with high nonlinearity and easy group velocity dispersion (GVD) engineering, SCG technology has been greatly improved. [12]. In particular, when a sub–ps scale ultrafast pulse is applied in the anomalous

dispersion (AD) region of a PCF with a single zero-dispersion wavelength (ZDW), various bright soliton (BS) dynamics including soliton fission, soliton-dispersive wave (DW) interaction, and Raman soliton self-frequency shift (RSSFS) occurs, which has enabled SCGs of ultra-broad bandwidth (BW) of hundreds to thousands of nm, recently. [12, 33, 81]. SCG has received great attention not only for the technical applicability of broadband spectral light sources but also for the physical environment in which various BS dynamics occur, especially DW trapping in gravity-like potentials generated by solitons [70], optical rogue wave generation [74, 75, 82], and optical Newton's cradle [83]. On the other hand, as a counterpart of SCG in AD based on BS dynamics (AD–SCG), SCG based on dark soliton (DS) generated from normal dispersion (ND) has also been studied [35, 84–86]. SCG in ND based on DS (ND–SCG) is a phenomenon that occurs when time-delayed two pulses of ND wavelength are applied to a PCF with a single ZDW, where the time-delayed two pulses form a DS train, and the generated DS train DS train creates a phase-matched DW in the AD region, increasing the spectrum BW [35, 86]. The difference from BS-based AD–SCG is that in the AD–SCG, the BS is generated at a random location due to modulation instability [12, 80], whereas in the ND–SCG, the DS is not voluntarily generated by the modulationally stable characteristic of the ND [40, 42]. Thus, a seed (e.g. a DS or time-delayed two pulses) for DS generation should be intentionally applied [40, 42, 86, 87].

#### **4.1.2. SCG in FAND–PCFs**

On the other hand, unlike AD / ND–SCG in PCF where ZDW is present, development of flattened all–normal dispersion (FAND) PCF with ND in all wavelength range enables SCG of new mechanism that does not depend on soliton dynamics (FAND–SCG) [88]. In this FAND–SCG, since the spectrum is widened only by coherent processes such as SPM, FWM, and optical wave breaking (OWB), the shot–to–shot fluctuation by the incoherent process is significantly reduced, resulting in a stable and high coherent SC radiation [88, 89]. Also, since it does not undergo soliton fission, SC light maintains a single pulse shape. [88, 89]. Thus, the resulting SC light is a single pulsed light source with a flat spectrum of several hundred nm while maintaining high coherence, and can be used for applications requiring a high coherence light source [90]. In this regard, I recently reported that if rare–earth ion–doped FAND–PCFs are utilized for FAND–SCG, it is possible to amplify SC spectra while retaining the characteristics of existing FAND–SCGs without significant changes in the spectral flatness measurement (SFM) or BW. [37].

In comparison with FAND–SCG and AD–SCG, the spectrum is broadened by the incoherent process in AD–SCG, but only by the coherent process in FAND–SCG [88–90]. Thus, FAND–SCG has a broader coherence spectrum (i.e.  $|g_{12}^{(1)}|$ ) and higher spectrally

averaged coherence (i.e.  $\langle |g_{12}^{(1)}| \rangle$ ) than AD–SCG [33]. On the other hand, the ND–SCG is an SCG generated by pumping in the ND region like the FAND–SCG. The two ND–SCGs may be considered to be the same or similar SCGs with the same GVD region of the seed pulse, but the principles are different. The differences between the two SCGs are as follows: ND–SCG is a SCG generated from a PCF with a single ZDW characteristic, in which the DW in the AD region is generated by the intentionally launched DS and the spectrum is extended to the AD region [35, 84–86]. On the other hand, FAND–SCG occurs in PCF with all–normal dispersion, and there is no intentional or spontaneous soliton generation, so that it is caused only by the spectral broadening of a seed pulse without generating phase–matched DW [88–90]. As a result, FAND–SCG is a soliton–free SCG, unlike AD and ND–SCG [88–90]. Recently, however, in the extreme parameter range of FAND–SCG (when the peak power of the seed pulse is higher than a few tens of kW or when the pulse width is as long as nanosecond), it has been reported that incoherent processes such as noise–seeded Raman scattering can degrade the coherence of SCG [90]. This incoherent process can lead to the generation of localized structures such as BS or DS in nonlinear media [12, 40, 42, 80, 91]. It is well known that BS is generated by modulational instability in AD domain [12, 80]. In the ND region, even if a slight dip occurs in the background pulse, the dip can develop into DS without threshold [40, 42], so dips inherent in the fine structure generated by the incoherent

process are likely to evolve from the ND region to the DS [40, 91]. Indeed, a study has also been reported that when a pulse builds up in a mode-locked fiber laser with Net ND, DS can be generated from noise [91]. However, DS generation and related dynamics in FAND–SCG have not yet been theoretically predicted or found.

#### **4.1.3. Scope of the study: Eruptive generation of DSs and coherence-collapse of FAND–SCGs in active PCFs**

In this regard, this study shows that DS can occur in FAND–SCG when high optical gain is applied, and the principle of DS generation is examined. It is shown that DS dynamics can increase shot-to-shot fluctuation of the SC spectrum and cause coherence collapse. This study deals with DS-based incoherent SCG phenomena that occur when a gain above a certain threshold is applied, which is higher than the gain used in the coherent SCG study of the Ytterbium (Yb)–doped FAND–PCF [37]. SCG generated from Yb–doped FAND–PCF assumes that sub-ps ultrafast pulse is used as seed, where seed pulse undergoes amplification by optical gain as well as GVD and Kerr nonlinearity [37]. This phenomenon can be modeled by a generalized complex Ginzburg–Landau equation (GCGLE) derived from a combination of the nonlinear Schrödinger equation (NLSE), which describes pulse dynamics by GVD and Kerr nonlinearity, and the Maxwell–Bloch equation (MBE), which describes light amplification [4, 12, 37, 80].

Based on the GCGLE, I observe the spectral and temporal evolution of the FAND–SCG with gain and show that DS occurs in the high gain region. Next, the SCG is calculated for each of the four combined cases when optical gain is included, not included, and when intrapulse Raman scattering (IRS) is included, not included. Then, I prove that DSs occur only when the IRS and the high optical gain are present at the same time. In particular, I demonstrate that the Raman–induced oscillatory structure (RIOS), which moves toward the leading edge with the oscillatory structure on the SC pulse when high optical gain and IRS are present at the same time, explains the principle of DS generation due to RIOS. The effects of RIOS and DS dynamics on the spectral characteristics of SCG such as BW, averaged energy spectral density and coherence under optical gain conditions are analyzed. Then, I discuss the phase transition that changes from coherent FAND–SCG to incoherent FAND–SCG by DS according to the optical gain.

## **4.2. Numerical model**

In this paper, I deal with SCG that occurs when sub-ps pulse is applied to Yb-doped FAND–PCF. At this time, the applied sub-ps pulse undergoes various nonlinear phenomena such as GVD, SPM, FWM, OWB, and IRS, and simultaneously undergoes amplification by Yb ions [37]. In general, the GVD and Kerr nonlinear phenomena experienced by ultrafast pulses can be described as NLSE [12, 80],

and the optical gain phenomena experienced by pulses can be described as MBE [4]. Yb-doped FAND-PCF can be described by NLSE and MBE coupled equation (NLSE-MBE) because pulse evolution proceeds under the interaction of GVD, Kerr nonlinear phenomenon and optical gain phenomenon [4] In addition, NLSE-MBE can be derived to GCGLE in a fiber at normal room temperature conditions, which is expressed as [4, 12, 65]:

$$\begin{aligned} \frac{\partial A}{\partial Z} = & -\frac{\alpha}{2} - \sum_{m=2}^{\infty} \frac{i^{m-1} \beta_m}{m!} \frac{\partial^m A}{\partial T^m} + i\gamma \left( 1 + \tau_{\text{shock}} \frac{\partial}{\partial T} \right) A(Z, T) \int_{-\infty}^{\infty} R(T') |A(Z, T-T')|^2 dT' \\ & + \frac{1}{2\pi} \frac{g}{2} \int_{-\infty}^{\infty} \frac{\tilde{A}(Z, \omega - \omega_0)}{1 - i(\omega - \omega_a)T_2} e^{-i(\omega - \omega_0)T} d\omega - \Gamma_R(Z, T). \end{aligned} \quad (4.2.1)$$

In Eq. (4.2.1),  $A$ ,  $\tilde{A}$ ,  $Z$ , and  $T$  are an optical field envelope, the Fourier transform of  $A$ , propagation distance, and time domain in co-moving frame at envelope group velocity, respectively.  $\alpha$ ,  $\beta_m$ , and  $\gamma$  are an attenuation,  $m$ -th order dispersion, and nonlinear coefficients.  $\tau_{\text{shock}}$  is the optical shock coefficient, which is characterized by the inverse of the center angular frequency of the optical field. The nonlinear response function is expressed by  $R(T) = (1-f_R) \delta(T) + f_R h_R(T)$ , which includes the SPM and Raman effects, where  $f_R$  is usually given by 0.2 for typical silica fibers (See [37] for details of the Raman response function).  $\Gamma_R$  is the spontaneous Raman noise (See Eq. (4.6.1)).  $\omega_a$  denotes the center frequency of the Yb-doped fiber amplifier,  $T_2$  the dipole relaxation time of Yb ions, which is inverse proportional to gain bandwidth [4, 37]. The saturated gain coefficient is expressed as  $g = g_{\text{us}} / (1 + E_{\text{pulse}}^{\text{eff}} / E_{\text{sat}}^{\text{eff}})$ ,

where  $E_{sat}^{eff}$  is the effective saturation energy of Yb ions per single pulse.  $E_{pulse}^{eff}$  is the effectively absorbed pulse energy, which is obtained as [65]:

$$E_{pulse}^{eff} = \frac{1}{2\pi} \int_{-\infty}^{\infty} \frac{|\tilde{A}(Z, \omega - \omega_0)|^2}{1 + (\omega - \omega_a)^2 T_2^2} d\omega. \quad (4.2.2)$$

In Eq. (4.2.2), I assume input pulses centered at 1064 nm having a Gaussian pulse profile such as  $A(T) = P_0^{1/2} \exp(-T^2/(T_0/1.665)^2)$  with a 200-fs pulse duration (full width at half maximum: FWHM) and a 1-nJ pulse energy, which correspond to a 4.7-kW peak power. The passive characteristics of the Yb-doped FAND-PCF is the same as those in Ref. [37] and the parameters are as follows: The fiber length  $L$  is 3.6 m and the attenuation of the optical fiber is assumed to be negligible because it is a short optical fiber. The fiber dispersion coefficients at 1064 nm are given by  $\beta_2 = 5.25$  ps<sup>2</sup>/km,  $\beta_3 = 4.37 \times 10^{-4}$  ps<sup>3</sup>/km, and  $\beta_4 = 2.03 \times 10^{-4}$  ps<sup>4</sup>/km, which result in FAND in a vicinity of 1064 nm. The fiber nonlinear coefficient  $\gamma$  is given as  $37$  W<sup>-1</sup>km<sup>-1</sup>, which provides high nonlinearity. As the active characteristics of Yb-doped FAND-PCF,  $T_2$  is set to 16 fs corresponding to 20 THz of the gain BW of Yb ions. [24, 37]. The unsaturated gain coefficient  $g_0$  is set to a value of 30 dB/m, which is higher than the 20 dB/m used in the previous study, which is within the range achievable with current optical fiber manufacturing techniques [68]. The effective saturation energy per single-pulse denoted as  $E_{sat}^{eff}$  is set to 3 nJ, which is a typical value for a Yb-doped fiber amplifier with a MHz-level repetition rate

[37]. I solve Eqs. (4.2.1) and (4.2.2) by utilizing the 4-th order Runge–Kutta method in the Fourier domain [69], where the number of time girds and the time window size to be  $2^{14}$  and 30 ps. The corresponding spectral window size is 546 THz, which allows for both SC radiation’s temporal and spectral spreads to fit into the time and the frequency windows. In this paper, I calculated the modulus of the complex degree of first-order coherence as following [12]:

$$|g_{12}^{(i)}(\omega, \tau=0)| = \frac{|\langle \tilde{A}_1^*(\omega) \tilde{A}_2(\omega) \rangle|}{\sqrt{\langle |\tilde{A}_1(\omega)|^2 \rangle} \sqrt{\langle |\tilde{A}_2(\omega)|^2 \rangle}}, \quad (4.23)$$

and the spectrally averaged coherence  $\langle |g_{12}^{(i)}(\omega, \tau=0)| \rangle$  is calculated as the weighted average of  $|g_{12}^{(i)}(\omega, \tau=0)|$  for normalized energy spectral density [12].

**Table 4.2.1. Simulation parameters.**

Parameter	Value	Parameter	Value
$\beta_2$ [ps <sup>2</sup> /km]	5.25	$g_{us}$ [dB/m]	0 ~ 30
$\beta_3$ [ps <sup>3</sup> /km]	$4.37 \times 10^{-4}$	$T_1$ [ms]	0.8
$\beta_4$ [ps <sup>4</sup> /km]	$2.03 \times 10^{-4}$	$T_2$ [fs]	16
$\gamma$ [W <sup>-1</sup> km <sup>-1</sup> ]	37	$E_{sat}/N^*$ [nJ]	3
$L$ [m]	3.6	$P_0$ [kW]	4.7
		$T_0$ [fs]	200

### 4.3. Review of SCG in active FAND–PCFs in low gain regime

In this section, the previous research on SCG in active FAND–

PCFs is briefly reviewed [37]. The master equation and the used numerical method are nearly similar with those utilized in this dissertation. Figure 4.3.1 shows the SC spectra with and without the optical gain. For the case of 0–dB/m gain, the spectrum is broadened by SPM at early stage. After the OWB length at about 0.2 m, the spectral broadening process is saturated and only the FWM continuously occurs inside the spectrum. If one induces 20–dB/m gain, the spectrum, spectral broadening process is saturated also at about 0.2 m, which indicates that the amplification process with 20–dB/m gain does not significantly affect the OWB length, although the OWB length is slightly reduced. Thus, it can be seen

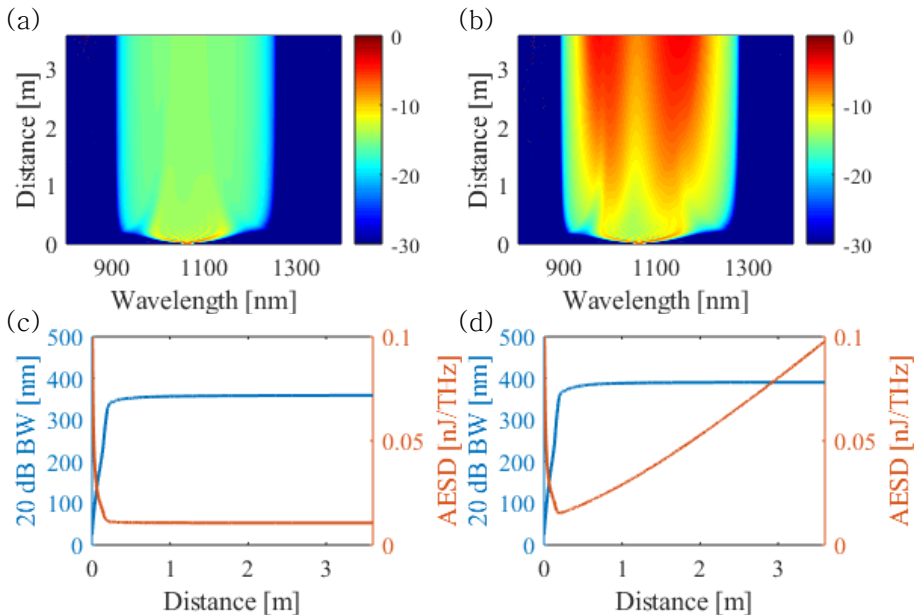


Fig. 4.3.1. spectral evolution of a 1–nJ input pulse through the HNL–PCF with (a) zero–gain or (b) 20–dB/m gain ( $L$ : length of the HNL–PCF). Lower: 20–dB BW (blue) and AESD (green) of the signal pulse with respect to the fiber length for (c) zero–gain or (d) 20–dB/m gain. This figure is a reproduced figure in Ref. [37]

that there is no big difference of 20-dB BW in both cases. On the other hand, it can be seen that AESD is continuously amplified after the OWB length. In other words, the energy injected by the gain ions is not used to increase the BW, but may be used to amplify the AESD. It should be also noted that the portion of the spectrum in the range of Yb gain spectrum is not amplified, but rather amplified to both sides of the amplification frequency. The cause of this phenomenon can be found in the time domain.

Figure 4.3.2 comparatively shows temporal evolutions of SC pulses with and without the optical gain of 20-dB/m. For the case of 0-dB/m gain, the pulse becomes rectangular shape due to SPM at early stage before the OWB. After OWB at 0.2 m, the pulse is

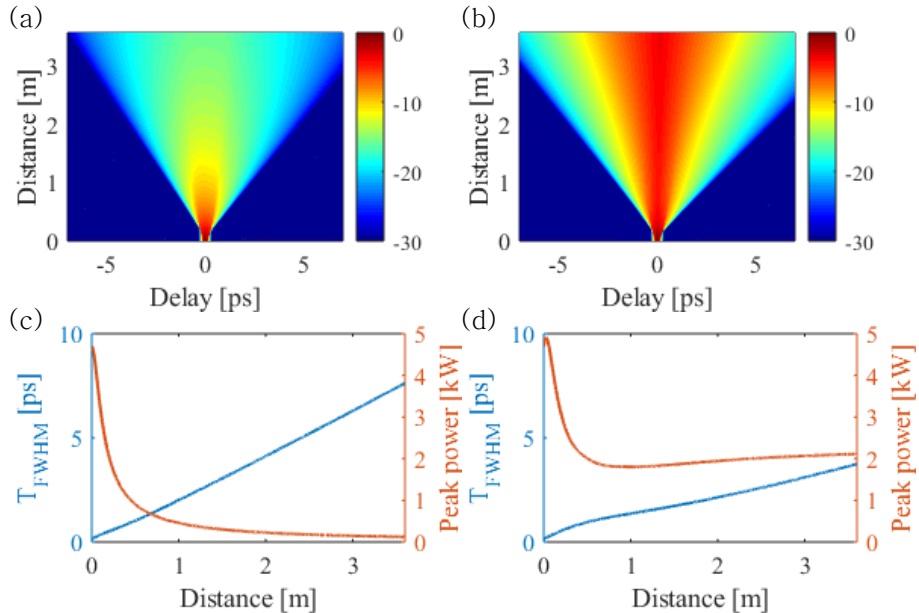


Fig. 4.3.2. Temporal evolution of a 1-nJ input pulse through the HNL-PCF with (a) zero-gain or (b) 20-dB/m gain. FWHM width (blue) and peak power (green) of the signal pulse with respect to the fiber length for (c) zero-gain or (d) 20-dB/m gain. This figure is a reproduced figure in Ref. [37]

suddenly broadened by the newly generated red- and blue-frequency components by FWM in OWB process. Then, the peak power continuously decreases due to the continuous pulse broadening. On the other hand, if the 20-dB/m gain is induced, the pulse peak power is compensated by the optical gain, so that the pulse maintains its nonlinearity. The maintained nonlinearity keeps distributing the energy toward blue- and red-frequency sides by means of SPM spectral broadening process.

Figure 4.3.4 comparatively shows the amplification performance of a low–nonlinear YDF and a HNL–PCF for external amplifier of a

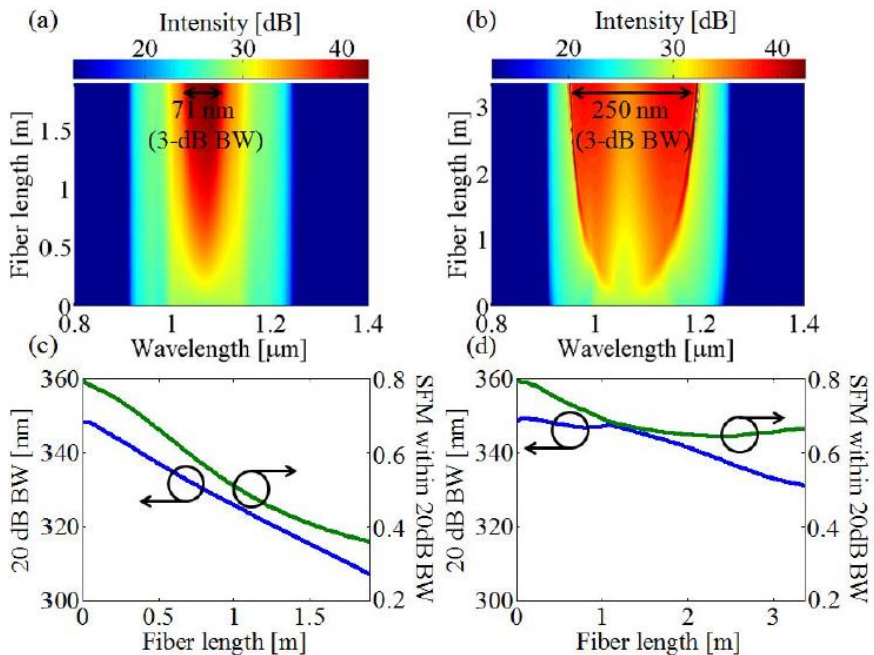


Fig. 4.3.4. Upper: spectral evolution of a 1-nJ SC input pulse through (a) the YDF of 1.9 m or (b) the active HNL–PCF of 3.4 m. Lower: 20-dB BW (blue) and SFM (green) of the signal pulse with respect to the fiber length for (c) the YDF PCF of 1.9 m or (d) the active HNL–PCF of 3.4 m. The image retrieved from Ref. [37].

broadband SC radiation. As shown in Fig. 4.3.4 (a) and (c), the gain effect cannot be distributed over the wide SC spectrum, but it is accumulated in the vicinity of the center frequency. Thus, the 20–dB BW and SFM continuously decreases with propagation distance. However, if one utilizes a HNL–PCF, then the gain effect is distributed over the wide SC spectrum bandwidth, so that SFM is nearly maintained and the BW does not undergo significant reduction. In terms of 3–dB BW, the former case has 71 nm BW, and the latter case has 250 nm BW, thereby indicating that an active HNL–PCF can be utilized as an external boost amplifier for broadband SC radiations.

This numerical investigation shows that the combined effect of the high nonlinearity and the optical gain can open up new possibilities of engineering of SCG. In next section, I further examine nonlinear pulse dynamics under the combined effect of the high nonlinearity and the optical gain in extremely high optical gain regime.

## **4.4. Eruptive generation of DSs on SCG in active FAND–PCFs**

### **4.4.1. DS generation at extremely high gain coefficient**

I first investigate the spectrum and temporal evolution of a seed pulse in a previously specified Yb–doped FAND–PCF for gain

coefficient  $g_0$  of 0, 10, 20 and 30–dB/m. Case with  $g_0 = 0$  dB/m can be considered SCG in passive FAND–PCF, whereas cases with  $g_0 = 10, 20,$  and  $30$  dB/m may be regarded as SCG in active FAND–PCF with different gains applied due to pump power or the number of doping ions. For the calculations of the four SCGs, the passive characteristics of FAND–PCFs and seed pulses are all set the same as mentioned in the previous section. I calculated the spectrum and temporal evolution of the SCG for four cases based on equations (1) and (2), and the results are shown in Fig. 4.4.1. In the case of  $g_0 = 0$ –dB/m, FAND–SCG with no gain effect involved, the spectrum was extended by SPM, and after the occurrence of OWB at about 0.22 m, no further increase in spectral BW occurs as shown in Fig. 4.4.1 (a). In the time domain, after OWB happens, the pulse width broadening continuously occurs due to ND and the peak power of the pulse gradually decreases as depicted in Fig. 4.4.1 (b). When applying a gain of  $g_0 = 10$  dB/m, OWB occurs at about 0.195 m, which is slightly shorter than the passive case, and the spectral intensity has increased overall without significant change in BW of the spectrum as shown in Fig. 4.4.1 (c). It should be noted that the gain effect is not concentrated at 281.8 THz, which is the gain center frequency of Yb, and is evenly distributed over the SC spectrum. This is because the nonlinearity can be maintained in virtue of peak power compensation by the optical gain and eventually the energy injected by the optical gain can be distributed through additional SPM [37]. When a gain of  $g_0 = 20$  dB/m is

applied, the peak power is amplified more than case of  $g_0 = 10$  dB/m and as a result, it can be seen in Fig. 4.4.1 (e) and (f) that the spectral intensity is further amplified. Therefore, in the case of  $g_0 = 10$  and 20 dB/m, even when the gain is applied, SCG is caused by the coherent process of SPM, FWM, and OWB, and the injected energy by the optical gain is distributed over a wide frequency band by coherent processes such as SPM. Up to this point, the BW and the SFM of the spectrum are not significantly changed and only the AESD is amplified by the optical gain, which is same as SCG in Yb-doped FAND–PCF in our previous study [37].

However, when I apply a gain of  $g_0 = 30$  dB/m, unexpectedly, the SC pulse dynamics are no longer on the extension of SC pulse dynamics at  $g_0 = 10$  and 20 dB/m and cause significantly different SCG from the two different gain coefficients are shown in Fig. 4.4.1 (g) and (h). In Fig. 4.4.1 (g), one can see that a continuous energy transfer occurs from the blue frequency part to the red frequency part. In addition, unlike the SCGs with the gain coefficients of 10 and 20 dB/m where BW saturates after OWB, the SCG with 30-dB/m gain coefficient undergoes OWB at about 0.16 m and then further spectral broadening toward red frequency region after 1.5 m. In the time domain, I can see that there is an additional wave that extends out faster than the leading edge of the pulse in Fig. 4.4.1 (h). Moreover, as shown in Fig. 4.4.1 (h), one can see that there is a fine structure over the SC pulse and if I zoom in like the inset of Fig. 4.4.1 (h), it can be observed that dark pulse with lower

intensity than the surroundings maintains its shape and travel above the SC pulse. On the other hand, it is known that light in the ND wavelength region of an optical fiber is modulationally stable, but if any hole is present in a continuous wave, the hole evolves into DS without any special threshold condition [40]. Even if the background wave is a pulse with a finite width rather than a perfect continuous wave, the hole has almost the same property as the DS if the width of background pulse is more than 10 times wider than that of the hole [40, 42]. Based on this, dark pulses generated in the FAND region are likely to have DS characteristics which are  $\tanh^2$  intensity profile and phase change at the dip. To check out this in detail, after capturing arbitrary dark pulses among the dark pulses shown in Fig. 4.4.1 (h), the temporal intensity and phase profile of the dark pulses are examined as shown in Fig. 4.4.2. Figures 4.4.2 (a) and (b) are magnifications on a portion of Fig. 4.4.1 (h), and Figs. 4.4.2 (c) and (d) show the intensity of the dark pulses and phase profiles indicated by the white dotted lines in Figs. 4.4.2 (a) and (b), respectively. As shown in Figs. 4.4.2 (c) and (d), the two dark pulses are fitted at a high agreement with the curve of  $\tanh^2$ , the intensity profile of DS, and phase change about  $\pi$  occurs in the center of the dip, indicating that the two dark pulses are DSs [40, 42]. In particular, the phase changes in the centers of the two DSs are close to  $\pi$  respectively, which indicates that the two DSs have  $B$  close to 1 and thus, they are ‘black soliton’.

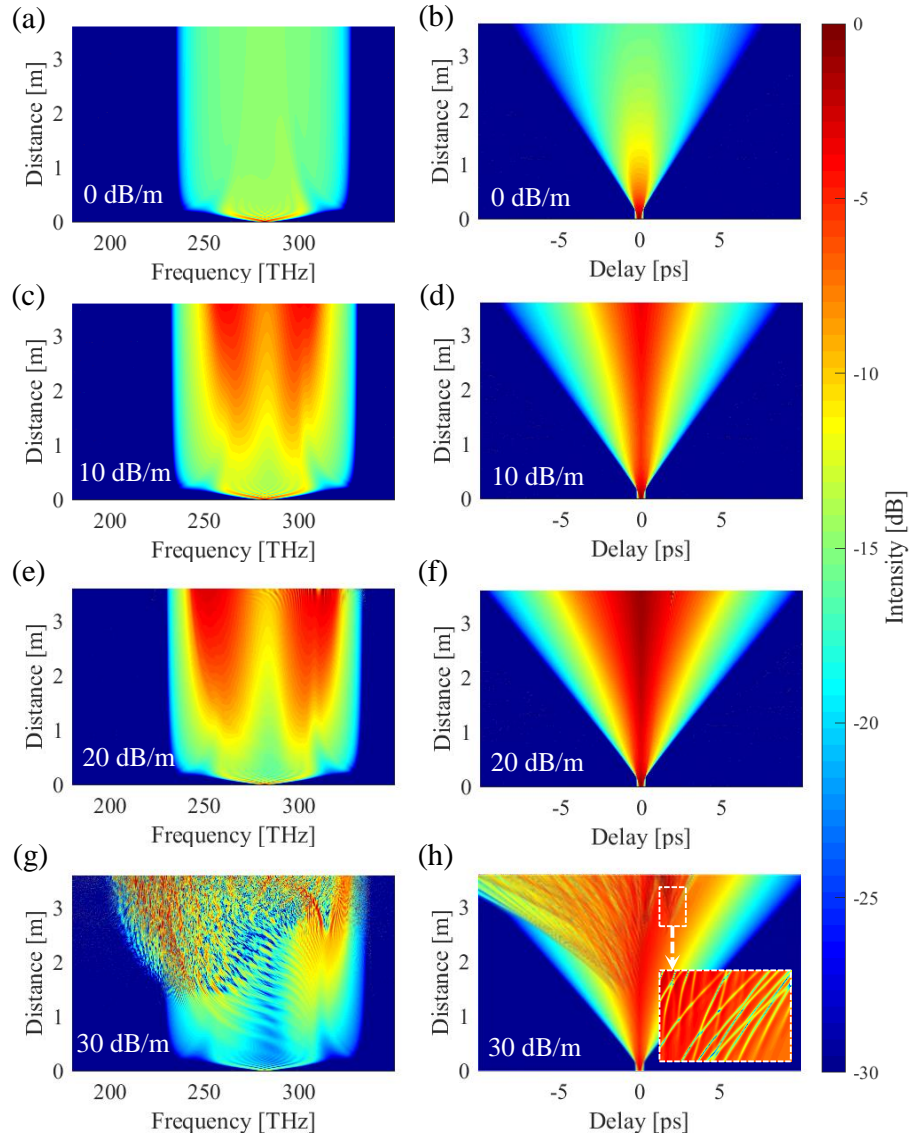


Fig. 4.4.1. Spectral and temporal evolution of SCG seeded by a 1.0-nJ sub-ps pulse with four different gain coefficients: 0-dB/m for (a) and (b), 10-dB/m for (c) and (d), 20-dB/m for (e) and (f), and 30-dB/m for (g) and (h).

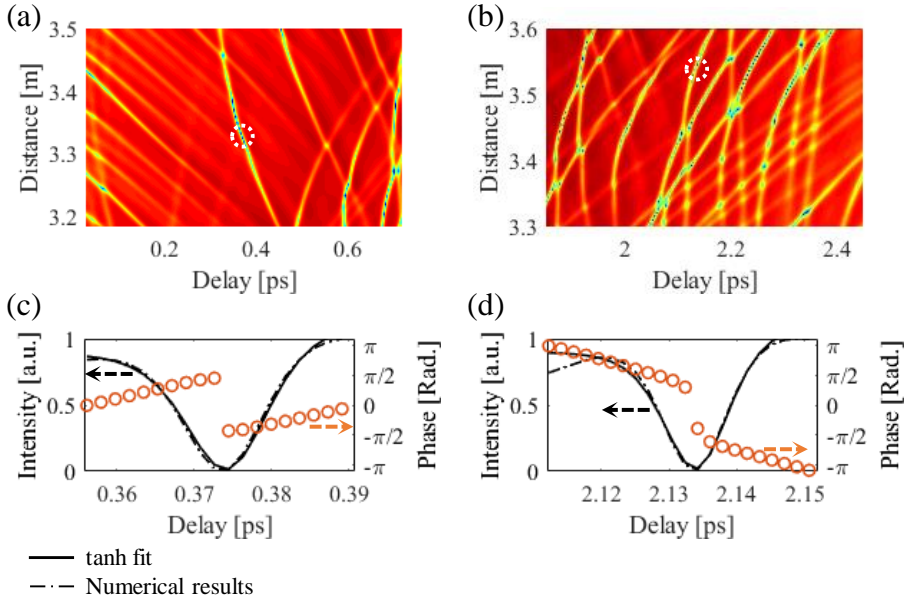


Fig. 4.4.2 Dark pulses atop the SC pulse with 30-dB/m gain coefficient, which are zoomed-in pictures of Fig. 4.4.1(h). (a) Dark pulses in a range of 0.35 ~ 0.39 ps, (b) Dark pulses in a range of 2.11 ~ 2.15 ps. (c) Curve fitting of the white-circled dark pulse in (a) with a  $\tanh^2$  curve and its phase profile, (d) Curve fitting of the white-circled dark pulse in (b) with a  $\tanh^2$  curve and its phase profile.

#### 4.4.2. Factors that cause DS generation in active FAND–PCFs

Although DS could not spontaneously occur in ND regime, spontaneously generated DSs are observed when the high gain with  $g_0 = 30$  dB/m is applied to FAND–SCG as shown in Fig. 4.4.1 (h). Prior to the analysis of the causes of spontaneous generation of DSs, SCG is simulated for the combination of two by two cases in order to identify factors that cause DS generation: Case I and II correspond to cases where optical gains of 0 and 30 dB/m are included, respectively, when IRS is not included for both cases.

Case III and IV correspond to cases where optical gains of 0 and 30 dB/m are included, respectively, when IRS is included for both cases. Comparing two SCGs of Case I and III shown in Fig. 4.4.3 (c) and (e) respectively, there is little difference in both cases and DSs do not occur in both cases. On the other hand, comparing two SCGs of Case II and IV shown in Figs. 4.4.3 (d) and (f), in Case IV where IRS and high gain are applied simultaneously, multiple DSs occur on the background pulse, whereas any DSs cannot be found in Case II. When comparing the output intensity profiles of Case II and IV, the intensity profile of Case IV is more asymmetric than Case II, and in Case IV, the fine structure covers the pulse from the middle of the trailing part to the leading edge, which cannot be seen in Case II. Moreover, it can be seen from Fig. 4.4.3 (b) that the peak power in Case IV is higher than in Case II due to the spike caused by DS. By comparing the SCGs of Cases I, II, III and IV, I can see that DS is spontaneously generated when both high gain or high peak power and IRS effects are present. In this paper, I will mainly compare Case II and Case IV to make it clear that DS is caused by IRS under high gain or high peak power condition.

#### **4.4.3. Observation of formation process of DSs at extremely high optical gain regime**

Next, to explain the spontaneous generation of DS, I investigated the temporal and spectral intensities at intervals of 0.1 m from 0.9 m

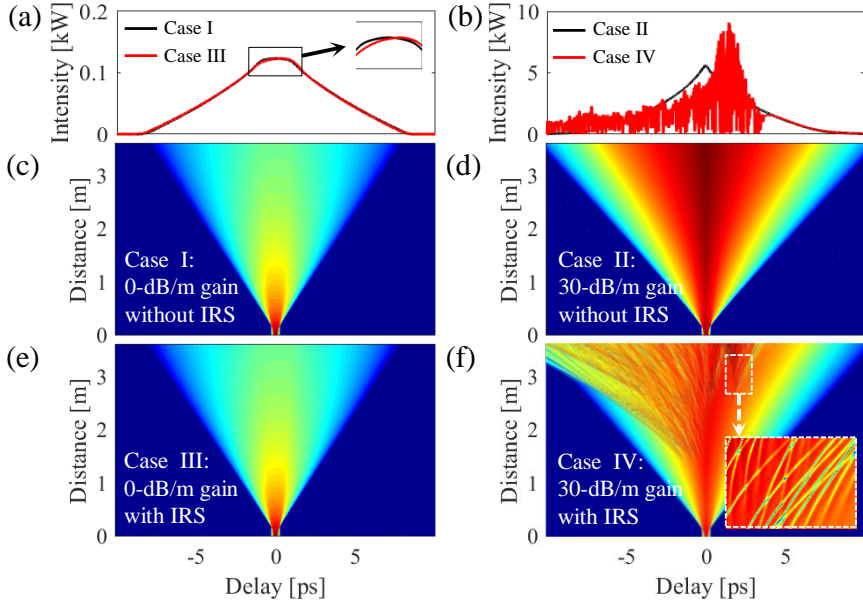


Fig. 4.4.3. Output temporal intensity profile for four cases: (a) output temporal intensity profiles of Case I (with 0-dB/m gain coefficient and without IRS) and Case III (with 0-dB/m gain coefficient and with IRS), (b) output temporal intensity profiles of Case II (with 30-dB/m gain coefficient and without IRS) and Case IV (with 30-dB/m gain coefficient and with IRS). Temporal evolution of SC pulses for four cases: (c) Case I, (d) Case II, (e) Case III, and (f) Case IV.

to 1.4 m in Case IV, and the result is depicted as the red solid lines in Fig. 4.4.4 (a) and (b). The black solid lines in Figs. 4.4.4 (a) and (b) correspond to Case II. Comparing the temporal intensities of Case II and IV at  $z = 0.9$  m in Fig. 4.4.4 (a), I can see that some oscillatory structure is generated over pulse in Case IV. From the fact that the oscillatory structure is generated only in Case IV, I can readily deduce that the oscillatory structure is generated due to IRS, which I can name as Raman-induced oscillatory structure (RIOS). Then, in order to investigate behavior of the RIOS, I select and trace one of the RIOS peaks as indicated by black arrows in Fig.

4.4.4 (a). In Fig. 4.4.4 (a), I can see that the peak moves from the trailing part of the SC pulse to the leading edge gradually when I trace the peak at position  $z = 0.9 \sim 1.4$  m. Additionally, the dip of the RIOS containing the peak is getting deeper and evolved into a gray soliton with a phase shift of about  $0.13\pi$  at the center of the dip, when the RIOS arrives at  $z = 1.4$  m. On the other hand, as shown in Fig. 4.4.4 (b), which corresponds to the spectra of Fig. 4.4.4 (a), as the RIOS moves to the leading edge, the fluctuation of the spectrum also moves toward the red frequency, and as the depth of dip generated by RIOS increases, so does the fluctuation of the spectrum. Thus, it indicates that the fluctuation of the spectrum is caused by the RIOS. It also should be noted that the fluctuation of the spectrum occurs at the outermost blue-shifted SPM peak, which suggests that the RIOS occurs from the blue-shifted SPM peak is sufficiently increased by the optical gain. Consequently, I can infer the causes of spontaneous generation of DS in Yb-doped FAND-PCFs as following: If the peak power of the pulse is compensated or further amplified by the optical gain, then the outermost blue-shifted SPM peak can sufficiently grow. Then, the Raman gain at the SPM peak is also sufficiently increased over a certain threshold and then the RIOS can be emitted at the peak frequency. The RIOS flows from the SPM peak to red frequency region, which is the equivalent flow from a trailing region toward a leading edge on the positively chirped pulse in the time domain (The RIOS's flow on the spectral-temporal domain can be seen in

the spectrogram of Fig. 4.6.1 (a)). As the RIOS flows to the leading edge, the background wave is simultaneously amplified, and the amplitude of the oscillation also increases. The fact that any holes in the background wave evolve to DS without threshold in ND regime, allows that dips in the RIOS evolve to DSs. The higher the background intensity, the narrower the DS width and the deeper the depth [40], so that DSs from the RIOS will gradually evolve to black soliton with  $B = 1$ . After all, the origin of spontaneous DS generation in Yb-doped FAND–PCF comes from the RIOS caused by IRS and high gain.

## 4.5. Raman–induced oscillatory structure (RIOS): The origin of DS generation in SCG via active FAND–PCFs

### 4.5.1. Review of theory on optical shock waves in nonlinear media

The RIOS is an oscillatory structure that is generated by the IRS and traveling above the pulse from the trailing area to the leading edge of the pulse when the peak power reaches a certain threshold power. In 1990, a study similar to the RIOS, published by Y. S. Kivshar, suggested that a Raman–induced shock wave (RISW) with an oscillating tail could be caused by the IRS effect [92]. According to the study, assuming that small amplitude DS occurs in the perfect CW background, Korteweg–deVries–Burgers equation

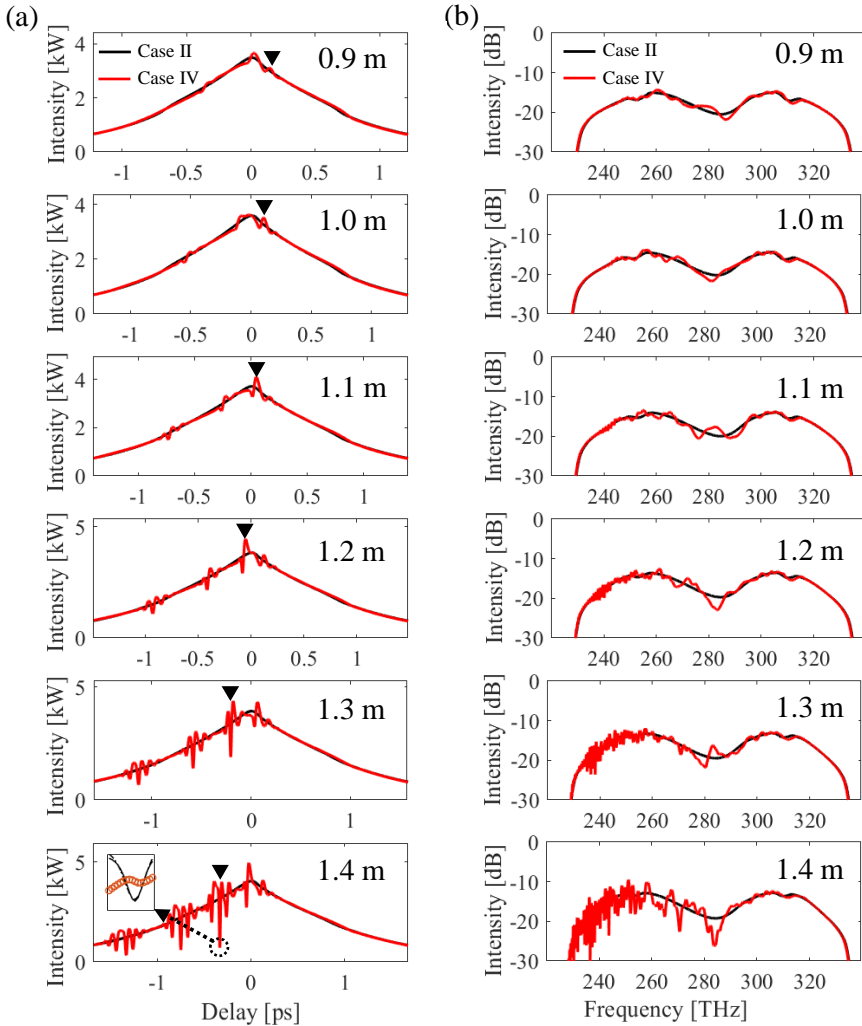


Fig. 4.4.4. (a) Temporal intensity profiles and (b) corresponding spectra of Case II and IV for a given distance.

(KdVBE) is derived from NLSE with IRS. In addition to DS, the KdVBE has a steady-state moving solution in the form of a shock wave with an oscillating structure, the shock wave is called RISW. The RISW is quite similar to the RIOS in that it is an oscillatory structure generated by the IRS and is a wave traveling on a background wave. In addition, theoretical studies have been

reported to have optical shock wave solutions in the Ginzburg–Landau equation assuming optical gain [93] and to have a stationary kink wave solution with oscillatory tail by higher order GVD and SRS [94]. As above, many studies have reported that IRS–like shock waves can be generated on the CW background by the IRS, but the theoretical study on the shock wave occurring in the situation I consider (Finite width pulse when IRS and optical gain are simultaneously) has not been performed yet. However, a rigorous theoretical analysis of the shock wave solutions that GCGL may have is beyond the scope of this paper, and will be addressed later in other publications.

#### 4.5.2. Analysis on gain–involved FWM–SRS coupling

As discussed in the preceding section, an elastic wall is now implemented into intermediate tubing apparatus that can be connected to the conventional urinary catheter tubing

When comparing Cases II and IV, the RIOS is clearly a wave generated by the IRS. However, it is known that in the FAND–SCG having a high peak power and low  $\beta_2$  value, the effective Raman gain coefficient is considerably reduced by the coupling between the IRS and the FWM [90]. Due to the low effective Raman gain coefficient, the amplification of Stokes frequency due to SRS is not prominent in FAND–SCG, and this is also shown in pulse spectrum and temporal intensity evolution of Fig. 4.4.1 (a)–(f), which maintain symmetry

even in the presence of SRS. Given this fact, the asymmetry of the spectrum and temporal intensity at high gains of 30–dB/m can be considered counter–intuitive. I now investigate the effects of Yb ions on the optical gain on the FWM–SRS coupling and the effective Raman gain constants, and verify that the effective Raman gain constants in the presence of optical gains cause an asymmetric spectrum. Based on references [90, 95], the equation where Stokes and anti–Stokes fields are coupled by FWM–SRS under the optical gain is derived as follows:

$$\frac{d}{dz} \begin{bmatrix} \bar{A}_s \\ \bar{A}_a^* \end{bmatrix} = i \frac{1}{L_{NL} e^{-gz}} \begin{bmatrix} q - Ke^{-gz} & q \\ -q & -q + Ke^{-gz} \end{bmatrix} \begin{bmatrix} \bar{A}_s \\ \bar{A}_a^* \end{bmatrix}. \quad (4.5.1)$$

In Eq. (4.5.1),  $\bar{A}_{s/a}$  is the Stokes/anti–Stokes field envelop which are normalized by the optical gain such that  $\bar{A}_{s/a} = A_{s/a} \exp(-g/2)$  and  $q = 1 - f_R + f_R \tilde{h}_R(-\Omega_R)$ , where  $\Omega_R$  is the Raman shift frequency which usually given as 13 THz in a typical silica fiber [80]. The phase mismatch term normalized by nonlinearity is expressed as  $K = -\Delta k/(2\gamma P_p)$  and the nonlinear characteristic length is denoted as  $L_{NL} = 1/(\gamma P_p)$ . In the derivation of Eq. (4.5.1), the frequency dependence of gain, dispersion by gain, and gain saturation are not taken into account in order to show only the effect of optical gain on FWM–SRS coupling. In this calculation, all parameters except peak power and gain constants are the same as those introduced in Section 2. Figures 4.5.1 (a)–(b) show which dominant phenomenon, FWM or SRS in FWM–SRS coupled dynamics, Fig. 4.5.1 (c) displays another energy transfer except for FWM and SRS, and Fig.

4.5.1 (d) – (k) show the normalized Stokes and anti–Stokes powers

$$\bar{P}_{s/a} = |\bar{A}_{s/a}|^2 \text{ and FWM phase parameter } \Delta\phi \text{ calculated from Eq. (4.5.1)}$$

when the pump power is 47, 4700 W, and the gain is 0, 40 dB/m.

Figure 4.5.1 (d) shows power evolution of  $\bar{P}_s$  and  $\bar{P}_a$ , which are displayed in blue– and red–solid lines. Figure 4.5.1 (d) also shows power evolution of normalized Stokes power  $\bar{P}_{s,SRS}$  amplified by only SRS without FWM–SRS coupling, which is plotted as the blue–dotted line. In Fig. 4.5.1 (d),  $\bar{P}_s$  has a positive gain,  $\bar{P}_a$  has a negative gain by SRS, and  $\bar{P}_{s,SRS}$  has a similar evolution with  $\bar{P}_s$ , which means that there is no significant effect by FWM–SRS coupling in the dynamics. At the same time, the FWM phase parameter  $\Delta\phi$  linearly increases with the propagation distance due to the phase mismatch  $\Delta k$  [95]. Therefore, it can be said that this parameter range belongs to the SRS–dominant regime with low FWM influence as shown in Fig. 4.5.1 (a). However, as shown in Fig. 4.5.1 (g), when a gain of 4 dB/m is applied, phase locking occurs at a point of about 1.5 m,  $\Delta\phi$  is locked and becomes constant and after 1.5 m,  $\bar{P}_s$  and  $\bar{P}_a$  begin to amplify with the same gain. At this time,  $\bar{P}_s$  is about 5 dB smaller than  $\bar{P}_{s,SRS}$ , which implies that the effective Raman gain is reduced by FWM–SRS coupling and the dynamics regime changes from the SRS–dominant regime to the FWM–dominant regime. This is because  $Ke^{-gz}$  in the diagonal matrix component on the left side of Eq. (4.5.1) gradually decreases with distance due to optical gain, effectively reducing the

phase mismatch of the FWM, and increasing the FWM effect. Figs. 4.5.1 (h) and (i) show the power and phase evolution when the 4.7 kW peak power of the seed pulse used in the SCG calculation is applied. Since the  $K$  value is already sufficiently small due to the high peak power, phase locking already occurs quickly as shown in Fig. 4.5.1 (i), and as a result, the effective Raman gain constant is sufficiently low to belong to the FWM–dominant regime as shown in Fig. 4.5.1 (h). Moreover, the gains of  $\bar{P}_s$  and  $\bar{P}_a$  are the same, and the output power values are almost similar. In this situation, even if the additional optical gain is applied, it is still in the FWM–dominant regime, which can be seen in Figs. 4.5.1 (i) and (j). This may explain why the spectra in Figs. 4.4.1 (a), (c), and (e) are nearly symmetrical despite the presence of the IRS. However, this approach cannot account for the asymmetric spectral augmentation phenomenon (Fig. 4.4.1 (g)) caused by the IRS at a gain of 30–dB/m. In other words, the spectral broadening that occurs toward the red frequency in Fig. 4.4.1 (g) cannot be explained by discrete energy transfer with the fixed pump frequency and the fixed gain spectra of Stokes and anti–Stokes corresponding to Figs. 4.5.1 (a) and (b). Instead, one can see that energy is continuously transferred from the blue to the red frequency if looking at the purple arrow in Fig. 4.4.1 (g). Looking at the frequency moving from high to low, I can see that the continuous energy transfer is due to the RIOS moving from the trailing area to the leading area in the time domain. This kind of continuous energy transfer by Raman

scattering is not new. In one example, RSSFS in AD–SCG is well known as the continuous energy transfer of BS by Raman scattering [12, 80]. The RIOS is a continuous energy transfer generated by Raman scattering in ND, similar to RSSFS in AD. After all, since the RIOS is not a discrete energy transfer phenomenon, the reduction of the effective Raman scattering gain coefficient due to FWM–SRS coupling is not related to the generation of the RIOS. Instead, as the peak power of the pulse increases due to the optical gain, Raman scattering is increased, and the RIOS is more likely to occur.

#### 4.5.3. DS generation by RIOS in active FAND–PCFs

As a result, when the high gain is applied in the SCG of Yb–doped FAND–PCF, the reason why numerous DS occurs spontaneously is as follows: In passive FAND–SCG (Case I or III) with a gain coefficient of 0 dB/m, the peak power decreases rapidly after OWB length as shown in the black dotted line in Fig. 4.5.2 (b), resulting in less nonlinear effect. Thus, Raman scattering cannot increase even further, and no RIOS occurs. On the other hand, when the optical gain is applied as in Case II, the optical gain compensates for the peak power depletion after OWB, as shown in the black solid line graph in Fig. 4.5.2 (b), and the nonlinear phenomenon does not decrease as a result. In Case IV, the peak power and nonlinear phenomena are kept high by optical gain, so the IRS effect is also increased. If the peak power is sufficiently high, the spectral energy

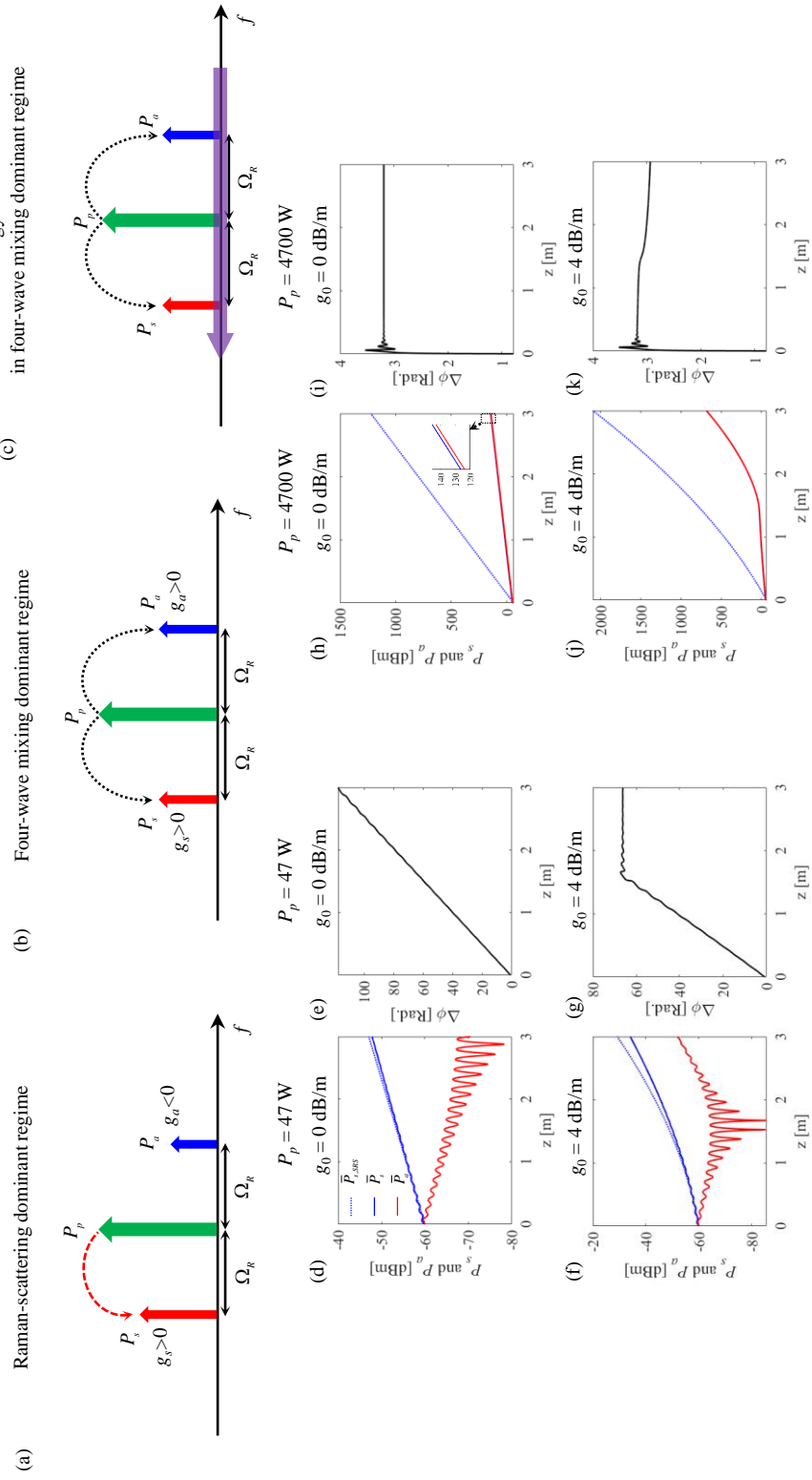


Fig. 4.5.1. Two dynamics regime in FWM-SRS coupled dynamics: (a) SRS-dominant regime and (b) FWM-dominant regime. (c) continuous energy transfer belonging to both (a) or (b). Stokes and anti-Stokes power with respect to the distance when (d)  $P_p = 47 \text{ W}$  and  $g_0 = 0 \text{ dB/m}$ , (f)  $P_p = 47 \text{ W}$  and  $g_0 = 4 \text{ dB/m}$ , (h)  $P_p = 4700 \text{ W}$  and  $g_0 = 0 \text{ dB/m}$ , and (i)  $P_p = 4700 \text{ W}$  and  $g_0 = 4 \text{ dB/m}$ . (e)–(k) are phase evolutions corresponding to (d)–(j), respectively.

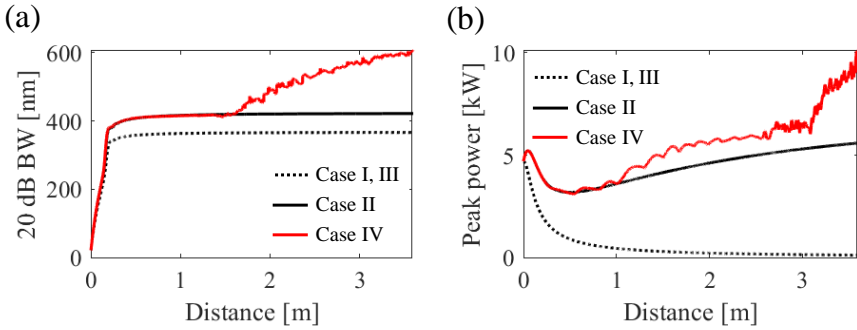


Fig. 4.5.2. Evolution of (a) 20-dB BW and (b) peak power of the SC pulse for four cases.

of outermost blue-shifted SPM peaks increases, and the RIOS is generated at the blue-shifted SPM peak. Since the generated RIOS undergoes a continuous energy transition toward the red frequency by the Raman effect, it proceeds from the trailing area to the leading edge in the time domain. On the other hand, dips inherent in RIOS in the ND regime evolve into DS. As the background intensity increases, the width becomes narrower and the depth deeper. Therefore, the depth of the ND becomes deeper as the background intensity continues to increase due to the gain as shown in Fig. 4 (a). As a result, due to the optical gain amplification of the background intensity, a large number of dips included in the RIOS proceed to evolve to a high blackness DS. Then, one might ask the question: Could DS be generated if a seed pulse of high enough peak power is applied to the passive FAND–PCF? If a seed pulse of sufficiently high peak power is applied to the passive FAND–PCF, the blue-shifted SPM peak becomes large enough, and RIOS is likely to occur from the spectral peak. The generated RIOS can grow deep enough beyond the peak of the pulse and will evolve into

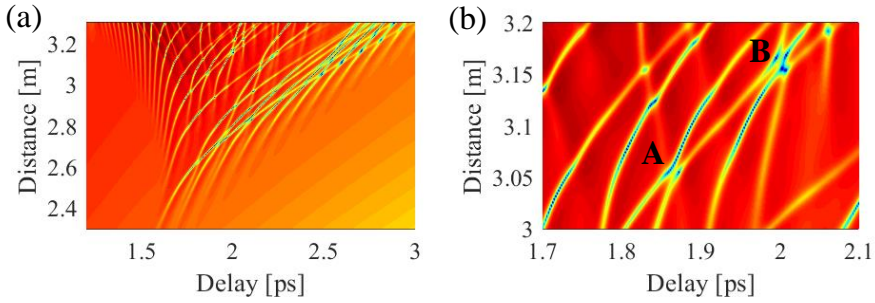


Fig. 4.5.3. (a) DS generation by RIOS in a cascading way. (b) Repulsive collision of DSs. A: Collision of two DSs, B: Collision of multiple DSs.

DS. However, unlike in the active case, the peak power is continuously depleted by the pulse broadening and the nonlinearity is reduced, making continuous DS generation difficult and the width of the DS gradually wider and gradually decay.

Since many DSs occur in the SCG of Yb-doped FAND-PCF, this SCG contains some interesting DS dynamics. As a first example, Fig. 4.5.3 (a) is a scene in which DS is generated gradually by background pulse and RIOS amplification. As a second example, Fig. 4.5.3 (b) is a phenomenon in which different groupo velocities collide with each other and undergo a temporal shift in a repulsive way. The DS dynamics can affect many aspects of the SCG, such as BW, AESD, and coherence. The next section discusses the impact of these DS dynamics on FAND-SCG.

## 4.6. DS dynamics and its impact on SCG in active FAND-PCFs

#### 4.6.1. Comparative review on BS and DS dynamics

In the previous section, I confirmed that RIOS occurs due to interplay of optical gain from Yb ion, Kerr nonlinearity, and IRS, and it can spontaneously generate numerous DS under the optical gain effect. Moreover, many of the generated DSs collide with each other and cause complex interactions. In this section, I examine these DS dynamics and investigate the impacts of DS dynamics on SCG characteristics in terms of AESD, BW, and coherence.

DS that occurs in ND is a counterpart soliton of BS that occurs in AD, and the dynamics of DS are also very different from or opposite to BS dynamics. The major properties of BS and DS are as follows: First, BS corresponds to a solution of eigenvalue problem of inverse scattering transform (IST), which is an eigenstate with discrete spectrum, but DS corresponds to eigenstate with continuous spectrum [40]. Therefore, BS is determined by the integer soliton number  $N$ , but DS is determined by the continuous blackness parameter ' $B$ ' in addition to the soliton number, so the solution is continuously distributed [40]. DS with  $B$  parameter is generally expressed as following [40, 42, 80]:

$$A(Z, T) = \sqrt{P_0} (\cos \phi \tanh \zeta - i \sin \phi) \exp(i\gamma P_0 Z), \quad (4.6.1)$$

$$\text{where } \zeta = \left( T - \sqrt{\gamma P_0 |\beta_2|} \sin(\phi) Z \right) \cos(\phi) / \tau_0, \quad B = \operatorname{sgn}(\sin(\phi)) \cos \phi$$

and  $\tau_0 = T_0 / N$ . One can readily notice from Eq. (4.6.1) that DS has different time delay and group velocity according to  $B$  in which

$dT / dZ = \sin \phi \sqrt{\gamma P_0 |\beta_2|}$ . When  $B < 0$ , DS moves faster than main pulse, whereas when  $B > 0$ , it moves slower than main pulse [40, 42]. In the absence of perturbation such as Raman scattering, DS has different group velocity depending on  $B$  even though it is the same  $N$ , which is different from BS having all the same group velocity for the same  $N$ . Secondly, while BS is a bright pulse in the zero background, DS is a dark pulse in the non-zero background. Therefore, the propagation properties of DS vary greatly depending on properties of the background wave [40, 91]. From Eq. (4.6.1), as the background intensity increases, the width of DS gets narrower with deeper depth, and the group velocity also changes. If the background wave is a pulse with a finite width rather than CW, the group velocity of DW is dependent on the slope of the pulse [40, 91]. For instance, if DS with  $B < 0$  is located near the leading edge with large slope, DS will be directed to the leading edge of the background pulse even faster, then it will decay with widened width and narrowed depth due to the low intensity of the background pulse [91]. Third, while the collisions of the two BSs are attractive to each other, that of the two DSs are repulsive to each other [96]. Thus, the BS merges into higher peak power solitons due to collisions, which sometimes produce rogue waves [74]. However, DS is repulsive rather than attractive to each other, so if two DSs collide, a temporal delay occurs in the direction of repulsion, as shown as A and B in Fig. 4.5.3 (b). For high soliton number  $N$ , while the BS is bounded by repeated merging to a high pulse and

separation, the DS is erupt into a narrow black soliton and several pairs of gray solitons that separate away from each other [80]. Finally, BS experiences red–shift by Raman scattering, while DS tends to undergo blue–shift [92, 97]. However, it is known that the frequency shift effect by Raman scattering of DS is about 2 times lower than that of BS [98].

#### 4.6.2. Spectrogram analysis on impact of DS dynamics on SCG in active FAND–PCFs

Like BS dynamics greatly affects BW and coherence of AD–SCG, DS dynamics can also be involved in the characteristics of the FAND–SCG. In order to analyze the effect of DS dynamics on SCG in the spectral–temporal domain, I calculated the spectrogram at the critical moment during DS–SCG interaction as shown in Fig. 4.6.1 [12]. Figure 4.6.1 (a), which corresponds to State I, is a spectrogram at  $z = 1.0$  m, showing the “S” shaped spectrogram generated by SPM and OWB in coherent FAND–SCG. However, the blue–shifted SPM peak generates RIOS that flows in the direction of the red arrow along the S–shaped edge. At the same time, the pulse continues to be amplified, increasing the depth of the RIOS dip that flows from the edge of the S structure, evolving DS to a higher blackness. The State II in Fig. 4.6.1 (b), I can see DSs created at the edge of the S–shaped spectrogram. State III in Fig. 4.6.1 (c), the pulse at  $z = 1.5$  m is further amplified by the gain, the number

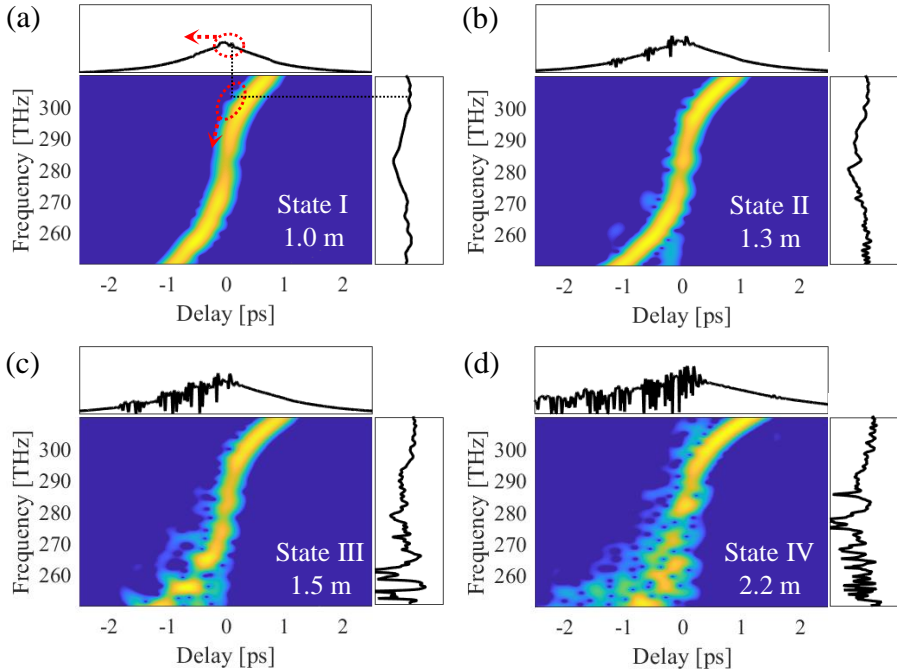


Fig. 4.6.1. Spectrograms of SC lights in an active FAND–PCF with 30–dB/m gain with respect to four different distances: (a) 1.0 m (State I), (b) 1.3 m (State II), (c) 1.5 m (State III), and (d) 2.2 m (State IV).

of generated DSs and its blackness grow sufficiently larger. Since the group velocity of DS is determined by the combination of its blackness, background slope, and Raman scattering, the generated DSs may have different group velocity from each other. DSs with different group velocity collide, and the repulsive collisions pushes DSs away from each other, changing the temporal location of DS. The combination of DS interactions and collisions locates the DS in the middle of the spectrogram of the S structure of the SC pulse. On the other hand, since DS has a  $\pi$  phase change in the middle of dip, the nonlinear phase shift caused by the SPM of SC pulse can no longer be continuous due to the  $\pi$  phase change of DS. As a result,

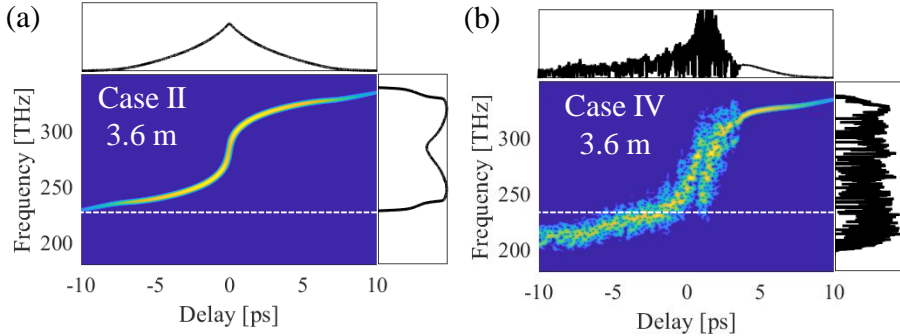


Fig. 4.6.2. Output spectrograms for (a) Case II and (b) IV.

the spectrum of the S structure loses its continuous structure and starts to undergo fragmentation. In State IV as shown in Fig. 4.6.1 (d), the segment of the cleaved S structure is gradually red shifted by Raman scattering and gradually loses the coherent S structure. The resultant spectrogram at  $z = 3.6$  m is shown in Fig. 4.6.2 (b). To compare the effect of DS on the spectrogram, the output spectrogram of Case II was calculated as shown in Fig. 4.6.2 (a). Comparing Figs. 4.6.2 (a) and (b), the output spectrum is slightly red shifted by Raman shift of the segment separated in Case IV. Also, unlike the case II spectrogram that maintains coherent S shape due to absence of DS, the Case IV spectrogram is covered with a large number of DS and the S shape is blunted.

#### 4.6.3. Coherence collapse by DS dynamics on SCG in active FAND–PCFs

As mentioned earlier, since the DS undergoes asymmetric phase change in the center, the phases of the pulses covered by

many DS are not continuous and the temporal coherence is reduced [99]. This results in a decrease in the coherence peak width in the temporal autocorrelation of the SC pulse (see Fig. 4.6.3) [99]. On the other hand, DS not only reduces temporal coherence, but also generates at random location for each shot, which increases shot-to-shot fluctuation of the SC spectrum. Figure 4.6.4 (a) shows the spectrally averaged coherence  $\langle |g_{12}^{(1)}| \rangle$ , for the gain coefficients in a range of  $0 \sim 30$ –dB/m. This was calculated for 500 pairs of ensembles, using one-photon-per-mode noise and spontaneous Raman noise as noise sources [12, 100]. The spontaneous Raman noise is expressed as the following equation [12, 100]:

$$\begin{aligned} \langle \Gamma_r(Z, \Omega) \Gamma_r^*(Z', \Omega') \rangle &= \frac{2f_r \hbar \omega_0}{\gamma} |\text{Im}[h_r(\Omega)]| \left[ n_{th}(|\Omega|) + U(-\Omega) \right] \\ &\quad \times \delta(Z - Z') \delta(\Omega - \Omega') \end{aligned} \quad (4.6.1)$$

where  $\Omega = \omega - \omega_0$ ,  $n_{th}$  is the thermal Bose distribution, and  $U$  is Heaviside step function. As shown in Fig. 4.6.4 (a), the coherence remains high around below 10–dB/m gain coefficient. In Fig. 4.6.4 (b), only 20–dB BW remains nearly constant at gain less than about 10–dB/m, so only AESD is amplified. Figure 4.6.4 (c) and (d) shows the  $|g_{12}^{(1)}(\omega)|$  spectrum and ensemble-averaged SC spectrum with respect to the gain coefficient respectively. For about below 10– dB/m gain coefficient, the spectral BW of  $|g_{12}^{(1)}(\omega)|$  nearly matches the BW of SC spectrum, and it can be seen from Fig. 4.6.4 (c) that it has perfect coherence over a wide frequency range, and the spectral BW is nearly constant for gain coefficients below 10–

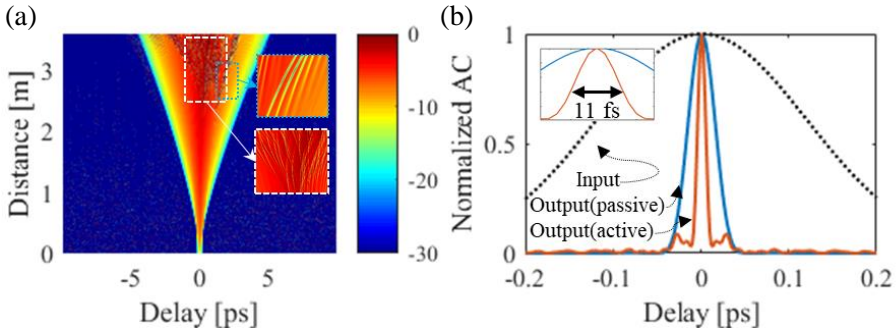


Fig. 4.6.3. (a) Temporal evolution of SCG with 20-dB/m gain coefficient and one-photon-per-mode noise. (b) Normalized autocorrelation traces for the input and two output pulses: passive and active FAND–PCFs.

dB/m. However, at gain coefficients above 10-dB/m, I can see a sudden increase in 20-dB BW, with a sharp decrease in coherence. As shown in Fig. 4.6.4 (c), as the coherence decreases from the middle part of the spectrum, the coherence of the spectral red frequency part decreases gradually as the gain increases. At the same time, I can see in Fig. 4.6.4 (d) that the region of the spectrum is further extended toward the red frequency. In fact, the reason for the coherence reduction after the gain coefficient 10-dB/m is because the DS generation process is noise sensitive. Particularly, since the RIOS is a wave corresponding to continuous energy transfer, noise applied to all frequency bands may affect the seeding of the RIOS. Since the noise-seeded RIOS has a different fluctuation for every shot, the DS generated from the RIOS is also sensitive to noise. In addition, noise is also amplified by the optical gain, so the effect of noise on RIOS and DS will increase proportional to the optical gain. This can be confirmed from the

comparison of two following cases: when no noise was applied, the coherent spectrum and temporal intensity was shown without any DS generation at 20–dB/m of gain coefficient (see Figs. 4.4.1 (e) and (f)). On the other hand, when noise was applied, DS is generated and coherence collapses at a gain coefficient of 20–dB/m as indicated in Figs. 4.6.4 (a)–(d). Furthermore, from the gain coefficient above 16 dB/m, the coherence is completely close to zero except for part of the spectrum in the blue frequency side. Thus, comparing the SCG characteristics corresponding to gain coefficient around 10 dB/m, it is as if there is a specific threshold value in the gain coefficient, which is similar to the abrupt phase transition phenomenon where the sudden change of dynamics occurs around the threshold (e.g. laser threshold). Starting from this threshold point, the behavior of the optical gain in the FAND–SCG changes. From the gain coefficient above 10 dB/m, the coherent FAND–SCG, where only the AESD is amplified while maintaining the spectral BW, does not occur. Rather, the coherence undergoes sudden decrease, and the BW further extends towards red frequency, and incoherent FAND–SCG occurs with DS generation and amplified AESD simultaneously. In particular, in the 20–dB BW graph of Fig. 4.6.4 (b), the sudden change of slope at the threshold point that changes from the coherent FAND–SCG to the incoherent FAND–SCG manifests phase transition phenomenon. Also, in Fig. 4.6.4 (a), it is notable to see that  $\langle \|g_{12}^{(1)}(\omega)\| \rangle$  follows the

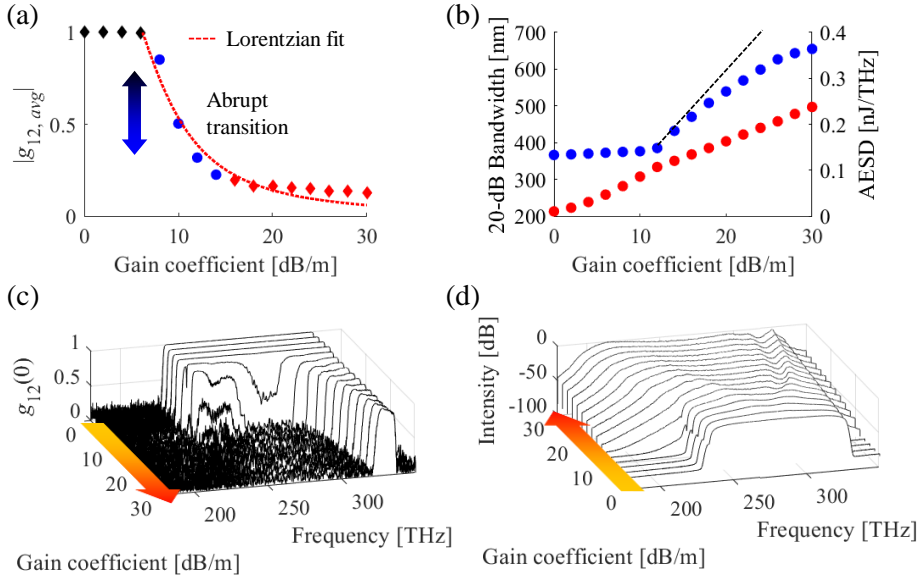


Fig. 4.6.4. (a) Spectrally averaged coherence value, (b) 20-dB BW, and AESD of SC pulses generated via an active FAND-PCF with respect to gain coefficient. (c) Output coherence spectra and (d) ensemble-averaged output spectral intensities corresponding to (a) and (b), respectively.

Lorentzian distribution. This is same with the  $\langle |g_{12}^{(1)}(\omega)| \rangle$  of the noise-like-pulse with respect to the nonlinear phase, which also follows the Lorentzian distribution in a quasi-mode-locked regime of the fiber ring cavity with optical gain [53, 101]. Since noise-like pulses are caused by BS dynamics under the influence of high nonlinearity and gain material, they may share some similarities with this phenomenon. Since noise-like pulses are caused by BS dynamics under the influence of high nonlinearity and gain material, they may share some similarities with this phenomenon.

Figure 4.6.5 (a)–(c) shows  $\langle |g_{12}^{(1)}(\omega)| \rangle$ , 20-dB BW, and AESD with respect to fiber length and gain coefficient. Considering Fig.

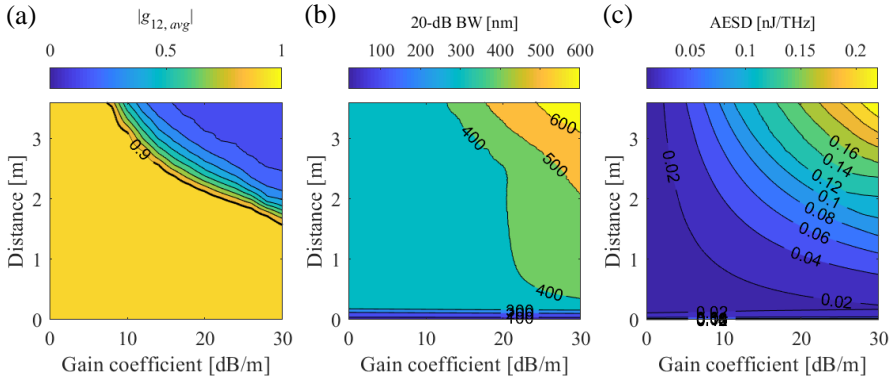


Fig. 4.6.5. (a) Spectrally averaged coherence value, (b) 20-dB BW, and (c) AESD of SC pulses generated via an active FAND–PCF for various fiber lengths and gain coefficients.

4.6.5 (a)–(c), I can notice the parameter range of fiber length and gain coefficient that provide high AESD or wide 20-dB BW while maintaining high coherence above 0.9 [90]. Following the line of  $\langle |g_{12}^{(1)}(\omega)| \rangle = 0.9$  in Fig. 4.6.5 (a), it can be seen that when the gain coefficient is low, the 20-dB BW is narrow, the AESD is low, whereas the gain coefficient is high, the 20-dB BW is widened and the AESD is raised. This suggests that coherence, 20-dB BW, and AESD can partially be adjusted by just adjusting the fiber length and pump power. In other words, compared to the SCG of the conventional passive FAND–PCF that only depends on width of the seed pulse and peak power to control BW and coherence [90], active FAND–PCF offers additional element (i.e. pump power) to control SCG, which makes the applications of SCG engineering easier.

# Chapter 5

## Concluding remarks

In this dissertation, SCG and related soliton dynamics in gain-embedded HNL-PCFs have been numerically and theoretically analyzed in AD and FAND.

For a numerical simulation of SCG in gain-embedded HNL-PCFs in which ultrafast pulses evolve to SC radiation under the complex interplay of group velocity dispersion, Kerr nonlinearity, and optical gain effect, a rigorous numerical model based on semiclassical quantum mechanical model has been established. In particular, I have derived MBE for Yb ions with four-level structure. The MBE can describe ultrafast interaction of Yb ions and femtosecond ultrafast pulses within the dipole relaxation time of Yb ions.

I have numerically analyzed SCG in an active HNL-PCF with AD having a negative slope excited by sub-ps ultrafast input pulses, based on the GCGLE derived from the NLSE-MBE model capable of dealing with ultrafast solitons' nonlinear interactions with gain ions within their dipole relaxation time.

I have first investigated optical gain effects on the SCG process, analyzing spectro-temporal characteristics of the HNL-PCF for two distinct cases with and without optical gain, and verified that distributed amplification of SC radiation via excited gain ions substantially improves the AESD without incurring degradation of the SFM of the corresponding SC spectrum. I have also figured out that during the SCG process, a multitude of solitons and QSSs with different group velocities are generated and intricately collide, and these collisions also produce high-frequency DWs particularly phase-matched with QSSs. I note that in the case of the active HNL-PCF, amplification of the pulse remnant is possible even after soliton fission, because distributed gain ions continually supply energy to SC radiation, which in turn leads to generation of a multitude of additional solitons (i.e., a soliton cluster). In fact, the high nonlinearity combined with high gain creates the soliton cluster and the corresponding high-frequency DWs, so that the energy spectra of them are more densely and evenly distributed across the wide BW of SC radiation than in the case of the passive HNL-PCF. I have also verified that the active HNL-PCF as an all-in-one structure capable of combining high nonlinearity and high gain exhibits much superior performance to the passive HNL-PCF from the viewpoint of AESD and SFM of the resultant SC radiation, even when an auxiliary lumped fiber amplifier is inserted before or after the passive HNL-PCF. In other words, the continual amplification of SC radiation distributed along the highly nonlinear fiber offers a

great advantage in power-scaling of SC radiation, firmly keeping good AESD and SFM characteristics.

In addition, I would like to compare the characteristic features of the HNL–PCF with AD with those of the HNL–PCF with FAND previously studied [37]. The common feature of them is that when high nonlinearity is combined with high gain distributed in the fiber, optical gain effects lead to substantially improved AESD without incurring significant degradation of SFM, regardless of their dispersion properties. However, the individual physical mechanisms and dynamics behind the results are largely different. Whilst in the case of the HNL–PCF with FAND the energy spectrum of the SC radiation is extended by coherent processes, such as SPM and optical wave breaking, in the case of the HNL–PCF with AD it is obtained by incoherent processes, such as modulation instability, soliton fission, and Raman scattering. Another distinct feature between them is that whilst the overall BW of the resultant SC radiation does not expand with the distributed gain effects in the case of HNL–PCF with FAND when it is used as a boost amplifier for the SC radiation, it does expand a bit in the case of the HNL–PCF with AD. This is due to the fact that in the latter case, the first ejected soliton undergoes a considerable amount of amplification by the distributed gain effects whereas in the former case the SC radiation tends to preserve its original temporal shape throughout the whole fiber length [9].

This study observed DS generation in SCG through Yb–doped

FAND-PCF, and found that DS was due to high gain and RIOS caused by IRS. Furthermore, DS has been shown to reduce coherence while causing further spectral broadening. When the peak power of the SC pulse reaches a certain threshold by the optical gain, the blue-shifted SPM peak also reaches a certain threshold, and RIOS occurs due to the strong IRS effect at the corresponding spectral peak. As the dips in RIOS evolved into the DS in the ND region and the background intensity was amplified by the optical gain, the blackness of the DS gradually increased, resulting in the eruptive generation of DSs. This DS was further red-shifted with RIOS to cause further spectral expansion. On the other hand, since the RIOS is a kind of wave that can be seeded by noise, the fluctuation of the RIOS and the generation position of the DS vary slightly with each shot due to the noise, which results in an increase in shot-to-shot fluctuation and a coherence collapse of FAND-SCG at high gain coefficients above a certain threshold. In particular, the dynamics rapidly changing before and after the threshold are similar to the abrupt phase transition, and further statistical studies are required. In addition, this study suggests that SCG characteristics such as coherence, 20-dB BW, and AESD can be engineered by adjusting optical gain or pump power. This makes the SCG engineering of the characteristics required for the application of SC light more convenient. For example, low coherence ultrafast SC pulses generated by increasing pump power can be used in applications such as optical coherence tomography

[102] or optical ghost imaging [103], and high coherence ultrafast SC pulses generated by lowering the pump power may be used in applications requiring small fluctuation of light sources such as beam combination [104].

Finally, I believe that the numerical study of SCG in active FAND–PCF will lay the foundation for the development of SCG technology in active highly nonlinear PCF, and I hope that it will be helpful for further study of soliton dynamics in open systems such as gain–embedded nonlinear medium.

## Appendix A

# Derivation of Maxwell–Bloch equation in a two–level system

### A.1. Derivation of Maxwell–Bloch equation for two–level systems

In this appendix, Maxwell–Bloch equation is derived, and the saturation energy is discussed. If the lossless system is assumed, then the system has a unitary Hamiltonian. However, in practice, the system is not unitary, but lossy. In Maxwell–Bloch equation,  $T_2$  makes the transition dipole moment decay to zero and the phase information be lost. More rigorously speaking,  $T_2$  is the decay time of the phase information and the loss of the phase information within  $T_2$  time is called ‘decoherence’. Furthermore, phase information can also be lost by vertical decay in the Bloch sphere. The vertical decay means the energy level decay, which is related with spontaneous emission in laser physics. The vertical decay time

## Appendix A. Derivation of Maxwell–Bloch equation in a two–level system

is called  $T_1$  time and this is the well-known the spontaneous decay time. Thus, in order to incorporate such decay phenomena into the Schrödinger equation, one needs to write the equation of motion in terms of density matrix rather than wavefunctions. In Schrödinger picture, the equation of motion in terms of the density matrix is given by

$$\dot{\rho} = \frac{i}{\hbar} [H, \rho], \text{ where } H = H_0 + H_I \quad (\text{A.1.1})$$

$H_0$  is the fundamental Hamiltonian of ions and  $H_I$  is the light–matter interaction Hamiltonian. Equation (A.1.1) can be expanded as following:

$$\dot{\rho}_{22} = -\gamma_{21}\rho_{22} + i\frac{\mu\tilde{E}}{\hbar}(\rho_{12} - \rho_{21}) \quad (\text{A.1.2})$$

$$\dot{\rho}_{11} = -\dot{\rho}_{22} \quad (\text{A.1.3})$$

$$\dot{\rho}_{12} = -\gamma_{12}\rho_{12} + i\alpha_{12}\rho_{12} + \frac{i}{\hbar}\mu\tilde{E}(\rho_{22} - \rho_{11}) \quad (\text{A.1.4})$$

Here, the dot on the top of the density matrix components denotes the time–derivative with respect to ‘real time’ rather than ‘fast time’ in a co–moving frame. It should be noted that if  $\rho_{12}$  rapidly decays to a steady state due to the presence of  $T_2$ , Eq. (A.1.2) and (A.1.4) become the form of the well–known rate equations for the two–level atoms.

The normalized population inversion  $n$  is defined as  $n = \rho_{22} - \rho_{11}$  in a two–level system. The transition dipole moment is defined as  $\tilde{p} = \mu(\rho_{12} + \rho_{21})$ . The equation for  $\tilde{p}$  is derived as following:

## Appendix A. Derivation of Maxwell–Bloch equation in a two–level system

$$\begin{aligned}\dot{\tilde{p}} &= \mu(\dot{\rho}_{12} + \dot{\rho}_{21}) , \\ &= -\gamma_{\perp}\tilde{p} - \omega_{12}\tilde{q} ,\end{aligned}\quad (\text{A.1.5})$$

where  $\tilde{q}$  is the quadrature component of  $\tilde{p}$ . The quadrature component  $\tilde{q}$  is necessary not to loss imaginary term of  $\rho_{12}$ , which can be defined as  $\tilde{q}=i\mu(\rho_{21}-\rho_{12})$ . To make Eq. (A.1.5) be complete, the equation for the quadrature component is also required.

$$\begin{aligned}\dot{\tilde{q}} &= i\mu(\dot{\rho}_{21} - \dot{\rho}_{12}) \\ &= -\gamma_{\perp}\tilde{q} + \omega_{12}\tilde{p} + \frac{2\mu^2\tilde{E}}{\hbar}(\rho_{22} - \rho_{11})\end{aligned}\quad (\text{A.1.6})$$

From the quadrature ODE system, Eq. (A.1.5) and (A.1.6) can be reduced to a single ODE.

$$\ddot{\tilde{p}} + 2\gamma_{\perp}\dot{\tilde{p}} + (\omega_{12}^2 + \gamma_{\perp}^2)\tilde{p} = -\frac{2\omega_{12}}{\hbar}\mu^2\tilde{E}n \quad (\text{A.1.7})$$

It should be noted that the transition dipole moment  $\tilde{p}$  is the real part of  $\rho_{12}$ . For the sake of simplicity, the time harmonic term is factored out such that  $\tilde{p}=pe^{-i\omega_0t}+\text{c.c}$ , where  $\omega_0$  is a center frequency of an optical wave which interacts to the atoms. Then, applying SVEA, Eq. (A.1.7) can be reduced as

$$\dot{p} = -(\gamma_{\perp} - i\Delta_a)p - \frac{i\mu^2}{\hbar}En , \quad (\text{A.1.8})$$

In the above derivation, the rotating wave approximation is utilized with  $\tilde{E}=Ee^{-i\omega_0t}+E^*e^{i\omega_0t}$ .

From Eq. (A.1.2) and (A1.3), the equation for  $n$  is simply obtained:

$$\begin{aligned}\dot{n} &= \dot{\rho}_{22} - \dot{\rho}_{11} = 2\dot{\rho}_{22} \\ &= -\gamma_{21}(n+1) + \frac{2\tilde{E}}{\hbar}\frac{\dot{\tilde{p}} + \gamma_{\perp}\tilde{p}}{\omega_{12}}\end{aligned}\quad (\text{A.1.9})$$

## Appendix A. Derivation of Maxwell–Bloch equation in a two–level system

In this derivation, this condition  $\dot{\tilde{p}} \gg \gamma_{\perp} \tilde{p}$  should be satisfied. Unless the condition is satisfied, the coherent interaction of light and atoms cannot be considered and Maxwell–Bloch equation will give the same result with the rate equations. Considering this condition, Eq. (A.1.9) is finally derived as following:

$$\dot{n} = -\gamma_{12}(n+1) + \frac{2i(Ep^* - E^* p)}{\hbar} \quad (\text{A.1.10})$$

In Eq. (A.1.10), ‘1’ in the first term indicates the spontaneous decay of atoms and the second term is driving term. Consequently, Bloch equations Eq. (A.1.2)–(A.1.4) are simplified as following;

$$\dot{p} = -(\gamma_{\perp} - i\Delta_a)p - \frac{i\mu^2}{\hbar}En \quad (\text{A.1.11})$$

$$\dot{n} = -\gamma_{12}(n+1) + \frac{2i(Ep^* - E^* p)}{\hbar} \quad (\text{A.1.12})$$

Now, the corresponding Maxwell equation can be derived. From the well-known Maxwell equation,

$$\frac{\partial A}{\partial z} + \frac{1}{v} \frac{\partial A}{\partial t} = \frac{1}{2icn\epsilon_0\omega_0} \frac{\partial^2}{\partial t^2} \langle \tilde{P} \rangle_{-i\omega_0 t} e^{-i(k_0 z - \omega_0 t)} \quad (\text{A.1.13})$$

where  $\langle \bullet \rangle_{-i\omega_0 t}$  implies that the component of the positive time–evolution part of the term inside the bracket.

Decomposing the polarization vector to the positive and negative evolution part as  $\tilde{P} = Pe^{-i\omega_0 t} + P^* e^{i\omega_0 t}$  and assuming SVEA, the propagation equation is given as following:

$$\begin{aligned} \frac{\partial A}{\partial z} + \frac{1}{v} \frac{\partial A}{\partial t} &= \frac{1}{2icn\epsilon_0\omega_0} \left[ (\ddot{P} - 2i\omega_0 \dot{P} - \omega_0^2 P) e^{-i\omega_0 t} \right] e^{-i(k_0 z - \omega_0 t)} \\ &= i \frac{\omega_0}{2cn\epsilon_0} Pe^{-ik_0 z} = i\gamma_Q Pe^{-ik_0 z} \end{aligned} \quad (\text{A.1.14})$$

## Appendix A. Derivation of Maxwell–Bloch equation in a two–level system

Macroscopic coupling coefficient is given by  $\gamma_\varrho = \frac{\omega_0}{2nc\epsilon_0}$  and the microscopic equation of Eq. (A.1.11) and (A.1.12) can be coupled via the following relationship of the transition dipole moment and the polarization vector:  $\tilde{P} = N_{tot}\tilde{p}$  and  $P = N_{tot}p$ . This relationship implies that the quantum behavior is represented via ensemble average of quantum behavior of each atom. Thus,  $p$  itself represents the ensemble averaged quantum behavior of atomic ensemble located at a certain spatial–temporal coordinate  $(z,t)$ . For the sake of simplicity, one can use co–moving frame with group velocity of optical pulses (i.e.  $(Z,T)=(z,t-z/v)$ ). Transforming the coordinate system, Maxwell–Bloch equations is reduced as

$$\frac{\partial A}{\partial Z} = i\gamma_\varrho \bar{P} \quad (\text{Macroscopic}), \quad (\text{A.1.15})$$

$$\frac{\partial \bar{p}}{\partial T} = -\left(\frac{1}{T_2} - i\Delta_a\right)\bar{p} - \frac{i\mu^2}{\hbar} An \quad (\text{Microscopic}), \quad (\text{A.1.16})$$

$$\frac{\partial n}{\partial T} = -\frac{1}{T_1}(n+1) + \frac{2i(A\bar{p}^* - A^*\bar{p})}{\hbar} \quad (\text{Microscopic}), \quad (\text{A.1.17})$$

In Eq. (A.1.15)–(A.1.17),  $\bar{P}$  and  $\bar{p}$  are phase–compensated parameters by amount of phase change by spatial evolution  $\exp(i k_0 Z)$ . The real polarization vector is expressed as  $\tilde{P} = \bar{P} \exp(i(k_0 z - \omega_0 t)) + \text{c.c.}$ . Eq. (A.1.15)–(A.1.17) are called the Maxwell–Bloch equations which describes light–atom interaction in semi–classical picture. The Bloch vector is obtained by

## Appendix A. Derivation of Maxwell–Bloch equation in a two–level system

$$\begin{bmatrix} 2\text{Re}\left(\rho_{21}e^{i\omega_0 t}\right) \\ -2\text{Im}\left(\rho_{21}e^{i\omega_0 t}\right) \\ n \end{bmatrix} = \begin{bmatrix} (\tilde{p}\cos\omega_0 t + \tilde{q}\sin\omega_0 t)/\mu \\ (-\tilde{p}\sin\omega_0 t + \tilde{q}\cos\omega_0 t)/\mu \\ n \end{bmatrix}. \quad (\text{A.1.18})$$

# Bibliography

1. G. P. Agrawal, *Nonlinear fiber optics*, Nonlinear Science at the Dawn of the 21st Century (Springer, 2000), pp. 195–211.
2. N. Sing-Kapany, "Fiber optics: Principles and applications," (1967).
3. W. G. French, J. B. MacChesney, P. O'connor, and G. Tasker, "BSTJ brief: Optical waveguides with very low losses," The Bell Syst. Tech. J. **53**, 951–954 (1974).
4. G. Agrawal, *Applications of nonlinear fiber optics* (Elsevier, 2001).
5. R. H. Stolen, E. Ippen, and A. Tynes, "Raman oscillation in glass optical waveguide," Appl. Phys. Lett. **20**, 62–64 (1972).
6. E. Ippen and R. Stolen, "Stimulated Brillouin scattering in optical fibers," Appl. Phys. Lett. **21**, 539–541 (1972).
7. A. Hasegawa and F. Tappert, "Transmission of stationary nonlinear optical pulses in dispersive dielectric fibers. II. Normal dispersion," Appl. Phys. Lett. **23**, 171–172 (1973).
8. L. F. Mollenauer, R. H. Stolen, and J. P. Gordon, "Experimental observation of picosecond pulse narrowing and solitons in optical fibers," Phys. Rev. Lett. **45**, 1095 (1980).
9. J. Chen, J. W. Sickler, E. P. Ippen, and F. X. Kärtner, "High repetition rate, low jitter, low intensity noise, fundamentally mode-locked 167 fs soliton Er-fiber laser," Opt. Lett. **32**, 1566–1568 (2007).
10. P. Grelu and N. Akhmediev, "Dissipative solitons for mode-locked lasers," Nat. Photon. **6**, 84 (2012).
11. F. Leo, L. Gelens, P. Emplit, M. Haelterman, and S. Coen, "Dynamics of one-dimensional Kerr cavity solitons," Opt. Express **21**, 9180–9191 (2013).
12. J. M. Dudley, G. Genty, and S. Coen, "Supercontinuum

- generation in photonic crystal fiber," Rev. Mod. Phys. **78**, 1135 (2006).
- 13. FOSCO., retrieved <https://www.fiberoptics4sale.com/blogs/archive-posts/95052294-optical-fiber-attenuation>.
  - 14. A. Yariv, *Optical electronics* (Saunders College Publ., 1991).
  - 15. R. P. Photonics, retrieved <https://www.rp-photonics.com/>.
  - 16. G. R. Fowles, *Introduction to modern optics* (Courier Corporation, 1989).
  - 17. E. Hecht, *Optics* (Pearson, 2015).
  - 18. B. E. Saleh and M. C. Teich, *Fundamentals of photonics* (John Wiley & Sons, 2019).
  - 19. W. Emkey and C. Jack, "Analysis and evaluation of graded-index fiber lenses," J. Light. Technol. **5**, 1156–1164 (1987).
  - 20. Thorlabs, retrieved <https://www.thorlabs.com/catalogpages/obsolete/2017/DCF38.pdf>.
  - 21. W. Belardi and J. C. Knight, "Hollow antiresonant fibers with low bending loss," Opt. Express **22**, 10091–10096 (2014).
  - 22. Wikipedia, retrieved [https://en.wikipedia.org/wiki/Photonic-crystal\\_fiber](https://en.wikipedia.org/wiki/Photonic-crystal_fiber).
  - 23. NKT Photonics, retrieved <https://www.nktphotonics.com/lasers-fibers/technology/photonic-crystal-fibers/>.
  - 24. D. J. Richardson, J. Nilsson, and W. A. Clarkson, "High power fiber lasers: current status and future perspectives," J. Opt. Soc. Am. B **27**, B63–B92 (2010).
  - 25. Y. Kwon, K. Park, D. Lee, H. Chang, S. Lee, L. A. Vazquez-Zuniga, Y. S. Lee, D. H. Kim, H. T. Kim, and Y. Jeong, "Current Status and Prospects of High-Power Fiber Laser Technology," Korean J. Opt. Photon. **27**, 1–17 (2016).
  - 26. C. Jauregui, J. Limpert, and A. Tünnermann, "High-power fibre lasers," Nat. Photon. **7**, 861 (2013).
  - 27. Todiamtools, retrieved <http://www.todiamtools.com/>.
  - 28. M. F. Ferreira, E. Castro-Camus, D. J. Ottaway, J. M. López-Higuera, X. Feng, W. Jin, Y. Jeong, N. Picqué, L. Tong, and B. M. Reinhard, "Roadmap on optical sensors," J. Opt. **19**, 083001 (2017).

29. Z. Liu, Z. M. Ziegler, L. G. Wright, and F. W. Wise, "Megawatt peak power from a Mamyshev oscillator," *Optica* **4**, 649–654 (2017).
30. D. Huang, E. A. Swanson, C. P. Lin, J. S. Schuman, W. G. Stinson, W. Chang, M. R. Hee, T. Flotte, K. Gregory, and C. A. Puliafito, "Optical coherence tomography," *Science* **254**, 1178–1181 (1991).
31. R. J. De Young and N. P. Barnes, "Profiling atmospheric water vapor using a fiber laser lidar system," *Appl. Opt.* **49**, 562–567 (2010).
32. R. W. Boyd, *Nonlinear optics* (Elsevier, 2003).
33. Y. Kwon, L. A. Vazquez-Zuniga, K. Park, S. Lee, H. Chang, and Y. Jeong, "Combinatorial study of supercontinuum generation dynamics in photonic crystal fibers pumped by ultrafast fiber lasers," *IEEE J. Quantum Electron.* **52**, 1–11 (2016).
34. D. V. Skryabin and A. V. Gorbach, "Colloquium: Looking at a soliton through the prism of optical supercontinuum," *Rev. Mod. Phys.* **82**, 1287–1299 (2010).
35. C. Milian, D. Skryabin, and A. Ferrando, "Continuum generation by dark solitons," *Opt. Lett.* **34**, 2096–2098 (2009).
36. T. Morioka, S. Kawanishi, K. Mori, and M. Saruwatari, "Nearly penalty-free,< 4 ps supercontinuum Gbit/s pulse generation over 1535–1560 nm," *Electron. Lett.* **30**, 790–791 (1994).
37. Y. Kwon, K. Park, S. Hong, and Y. Jeong, "Numerical study on the supercontinuum generation in an active highly nonlinear photonic crystal fiber with flattened all-normal dispersion," *IEEE J. Quantum Electron.* **53**, 1–8 (2017).
38. H. Chen, S.-P. Chen, Z.-F. Jiang, and J. Hou, "Enhanced supercontinuum generation in nonlinear Ytterbium-doped fiber amplifier by seeding at short wavelength," *IEEE J. Quantum Electron.* **51**, 1–7 (2015).
39. L. A. Vazquez-Zuniga, X. Feng, Y. Kwon, H. Kim, J. Shi, W.

- Loh, and Y. Jeong, "W-type highly erbium-doped active soft-glass fibre with high nonlinearity," *Electron. Lett.* **52**, 1047–1048 (2016).
40. Y. S. Kivshar and B. Luther-Davies, "Dark optical solitons: physics and applications," *Phys. Rep.* **298**, 81–197 (1998).
41. Y. Kodama and A. Hasegawa, "Nonlinear pulse propagation in a monomode dielectric guide," *IEEE J. Quantum Electron.* **23**, 510–524 (1987).
42. A. Weiner, "Dark optical solitons," in *Optical Solitons: Theory and Experiment* (1992), p. 378.
43. L. Susskind and A. Friedman, *Quantum mechanics: The theoretical minimum* (Basic Books, 2014).
44. M. O. Scully and M. S. Zubairy, "Quantum optics," (AAAPT, 1999).
45. A. Einstein, "The Quantum Theory of Radiation," *Physikalische Zeitschrift* **18**(1917).
46. M. Fox, *Quantum optics: an introduction* (OUP Oxford, 2006), Vol. 15.
47. G. J. d. Valcárcel, E. Roldán, and F. Prati, "Semiclassical theory of amplification and lasing," *Rev. Mex. Fis. E* **52**, 198–214 (2006).
48. J. K. Ranka, R. S. Windeler, and A. J. Stentz, "Visible continuum generation in air-silica microstructure optical fibers with anomalous dispersion at 800 nm," *Opt. Lett.* **25**, 25–27 (2000).
49. K. Shi, P. Li, S. Yin, and Z. Liu, "Chromatic confocal microscopy using supercontinuum light," *Opt. Express* **12**, 2096–2101 (2004).
50. C. F. Kaminski, R. S. Watt, A. D. Elder, J. H. Frank, and J. Hult, "Supercontinuum radiation for applications in chemical sensing and microscopy," *Appl. Phys. B* **92**, 367 (2008).
51. N. M. Israelsen, C. R. Petersen, A. Barh, D. Jain, M. Jensen, G. Hannesschläger, P. Tidemand-Lichtenberg, C. Pedersen, A. Podoleanu, and O. Bang, "Real-time high-resolution mid-infrared optical coherence tomography," *Light Sci. Appl.* **8**,

- 11 (2019).
52. A. Labruyère, A. Tonello, V. Couderc, G. Huss, and P. Leproux, "Compact supercontinuum sources and their biomedical applications," *Opt. Fiber Technol.* **18**, 375–378 (2012).
53. Y. Kwon, L. A. Vazquez-Zuniga, S. Lee, H. Kim, and Y. Jeong, "Numerical study on multi-pulse dynamics and shot-to-shot coherence property in quasi-mode-locked regimes of a highly-pumped anomalous dispersion fiber ring cavity," *Opt. Express* **25**, 4456–4469 (2017).
54. C. Lei, A. Jin, R. Song, Z. Chen, and J. Hou, "Theoretical and experimental research of supercontinuum generation in an ytterbium-doped fiber amplifier," *Opt. Express* **24**, 9237–9250 (2016).
55. C. Lei, R. Song, Z. Chen, D. Pu, and J. Hou, "Supercontinuum generation in an ytterbium-doped fiber amplifier with cascaded double-clad passive fiber tapers," *IEEE Photon. J.* **9**, 1–10 (2017).
56. C. Louot, B. M. Shalaby, E. Capitaine, S. Hilaire, P. Leproux, D. Pagnoux, and V. Couderc, "Supercontinuum generation in an ytterbium-doped photonic crystal fiber for CARS spectroscopy," *IEEE Photon. Technol. Lett.* **28**, 2011–2014 (2016).
57. T. Schreiber, J. Limpert, H. Zellmer, A. Tünnermann, and K. P. Hansen, "High average power supercontinuum generation in photonic crystal fibers," *Opt. Commun.* **228**, 71–78 (2003).
58. M. Tao, T. Yu, Z. Wang, H. Chen, Y. Shen, G. Feng, and X. Ye, "Super-flat supercontinuum generation from a Tm-doped fiber amplifier," *Sci. Rep.* **6**, 23759 (2016).
59. F. R. Arteaga-Sierra, A. Antikainen, and G. P. Agrawal, "Dynamics of soliton cascades in fiber amplifiers," *Opt. Lett.* **41**, 5198–5201 (2016).
60. Z. Huang, J. Wang, H. Lin, D. Xu, R. Zhang, Y. Deng, and X. Wei, "Combined numerical model of laser rate equation and Ginzburg-Landau equation for ytterbium-doped fiber

- amplifier," J. Opt. Soc. Am. B **29**, 1418–1423 (2012).
61. J. T. Manassah and B. Gross, "Propagation of femtosecond pulses in a fiber amplifier," Opt. Commun. **122**, 71–82 (1995).
62. C.-W. C. Sien Chi, "Femtosecond soliton propagation in erbium-doped fiber amplifiers: the equivalence of two different models," Opt. Commun. **106**, 193–196 (1994).
63. K. Park, H. Kim, M. Yeo, and Y. Jeong, "Quantum-coherent supercontinuum generation in active highly nonlinear photonic crystal fibers," in *2018 10th International Conference on Advanced Infocomm Technology (ICAIT)*, (IEEE, 2018), 204–208.
64. K. Park, J. Na, J. Kim, and Y. Jeong, "Numerical study on supercontinuum generation in an active highly nonlinear photonic crystal fiber with anomalous dispersion," IEEE J. Quantum Electron. (2020) (Under consideration for publication).
65. M. Horowitz, C. R. Menyuk, and S. Keren, "Modeling the saturation induced by broad-band pulses amplified in an erbium-doped fiber amplifier," IEEE Photon. Technol. Lett. **11**, 1235–1237 (1999).
66. S. Chi, C.-W. Chang, and S. Wen, "Femtosecond soliton propagation in erbium-doped fiber amplifiers: the equivalence of two different models," Opt. Commun. **106**, 193–196 (1994).
67. L. W. Liou and G. P. Agrawal, "Solitons in fiber amplifiers beyond the parabolic-gain and rate-equation approximations," Opt. Commun. **124**, 500–504 (1996).
68. R. Poozesh, K. Madanipour, and P. Parvin, "High SNR watt-level single frequency Yb-doped fiber laser based on a saturable absorber filter in a cladding-pumped ring cavity," J. Light. Technol. **36**, 4880–4886 (2018).
69. J. Hult, "A fourth-order Runge-Kutta in the interaction picture method for simulating supercontinuum generation in optical fibers," J. Light. Technol. **25**, 3770–3775 (2007).

70. A. V. Gorbach and D. V. Skryabin, "Light trapping in gravity-like potentials and expansion of supercontinuum spectra in photonic-crystal fibres," *Nat. Photonics* **1**, 653 (2007).
71. R. Driben, B. A. Malomed, A. V. Yulin, and D. V. Skryabin, "Newton's cradles in optics: From N-soliton fission to soliton chains," *Phys. Rev. A* **87**, 063808 (2013).
72. R. Driben, A. V. Yulin, A. Efimov, and B. A. Malomed, "Trapping of light in solitonic cavities and its role in the supercontinuum generation," *Opt. Express* **21**, 19091–19096 (2013).
73. D. R. Solli, C. Ropers, P. Koonath, and B. Jalali, "Optical rogue waves," *Nature* **450**, 1054 (2007).
74. R. Driben and I. Babushkin, "Accelerated rogue waves generated by soliton fusion at the advanced stage of supercontinuum formation in photonic-crystal fibers," *Opt. Lett.* **37**, 5157–5159 (2012).
75. S. Lee, K. Park, H. Kim, L. A. Vazquez-Zuniga, J. Kim, and Y. Jeong, "Intermittent burst of a super rogue wave in the breathing multi-soliton regime of an anomalous fiber ring cavity," *Opt. Express* **26**, 11447–11457 (2018).
76. T. G. Philbin, C. Kuklewicz, S. Robertson, S. Hill, F. König, and U. Leonhardt, "Fiber-optical analog of the event horizon," *Science* **319**, 1367–1370 (2008).
77. S. Kivistö, R. Herda, and O. G. Okhotnikov, "All-fiber supercontinuum source based on a mode-locked ytterbium laser with dispersion compensation by linearly chirped Bragg grating," *Opt. Express* **16**, 265–270 (2008).
78. J. H. V. Price, W. Belardi, T. M. Monro, A. Malinowski, A. Piper, and D. J. Richardson, "Soliton transmission and supercontinuum generation in holey fiber, using a diode pumped Ytterbium fiber source," *Opt. Express* **10**, 382–387 (2002).
79. C.-H. Yeh, C.-C. Lee, and S. Chi, "120-nm bandwidth erbium-doped fiber amplifier in parallel configuration," *IEEE Photon. Technol. Lett.* **16**, 1637–1639 (2004).

80. G. P. Agrawal, "Nonlinear fiber optics," in *Nonlinear Science at the Dawn of the 21st Century* (Springer, 2000), pp. 195–211.
81. D. Jain, R. Sidharthan, P. M. Moselund, S. Yoo, D. Ho, and O. Bang, "Record power, ultra–broadband supercontinuum source based on highly GeO<sub>2</sub> doped silica fiber," *Opt. Express* **24**, 26667–26677 (2016).
82. D. Solli, C. Ropers, P. Koonath, and B. Jalali, "Optical rogue waves," *Nature* **450**, 1054 (2007).
83. R. Driben, B. Malomed, A. Yulin, and D. Skryabin, "Newton's cradles in optics: From N–soliton fission to soliton chains," *Phys. Rev. A* **87**, 063808 (2013).
84. T. Marest, C. M. Arabí, M. Conforti, A. Mussot, C. Milian, D. V. Skryabin, and A. Kudlinski, "Collision between a dark soliton and a linear wave in an optical fiber," *Opt. Express* **26**, 23480–23491 (2018).
85. C. Milián, T. Marest, A. Kudlinski, and D. V. Skryabin, "Spectral wings of the fiber supercontinuum and the dark–bright soliton interaction," *Opt. Express* **25**, 10494–10499 (2017).
86. T. Marest, C. M. Arabí, M. Conforti, A. Mussot, C. Milián, D. V. Skryabin, and A. Kudlinski, "Emission of dispersive waves from a train of dark solitons in optical fibers," *Opt. Lett.* **41**, 2454–2457 (2016).
87. C. Finot, J. M. Dudley, and G. Millot, "Generation of dark solitons by interaction between similaritons in Raman fiber amplifiers," *Opt. Fiber Technol.* **12**, 217–226 (2006).
88. L. E. Hooper, P. J. Mosley, A. C. Muir, W. J. Wadsworth, and J. C. Knight, "Coherent supercontinuum generation in photonic crystal fiber with all–normal group velocity dispersion," *Opt. Express* **19**, 4902–4907 (2011).
89. I. A. Sukhoivanov, S. O. Iakushev, O. V. Shulika, J. A. Andrade–Lucio, A. Díez, and M. Andrés, "Supercontinuum generation at 800 nm in all–normal dispersion photonic crystal fiber," *Opt. Express* **22**, 30234–30250 (2014).

---

## Bibliography

90. A. M. Heidt, J. S. Feehan, J. H. V. Price, and T. Feurer, "Limits of coherent supercontinuum generation in normal dispersion fibers," *J. Opt. Soc. Am. B* **34**, 764–775 (2017).
91. R. I. Woodward and E. J. R. Kelleher, "Dark solitons in laser radiation build-up dynamics," *Phys. Rev. E* **93**, 032221 (2016).
92. Y. S. Kivshar, "Dark-soliton dynamics and shock waves induced by the stimulated Raman effect in optical fibers," *Phys. Rev. A* **42**, 1757 (1990).
93. D. Christodoulides and M. Carvalho, "Optical shock waves in nonlinear dispersive amplifying media," *Opt. Lett.* **19**, 251–253 (1994).
94. E. Gromov and V. Tyutin, "Kink Waves in an Extended Nonlinear Schrödinger Equation with Allowance for Stimulated Scattering and Nonlinear Dispersion," *Radiophys. Quantum Electron.* **57**, 279 (2014).
95. S. Coen, D. A. Wardle, and J. D. Harvey, "Observation of non-phase-matched parametric amplification in resonant nonlinear optics," *Phys. Rev. Lett.* **89**, 273901 (2002).
96. R. N. Thurston and A. M. Weiner, "Collisions of dark solitons in optical fibers," *J. Opt. Soc. Am. B* **8**, 471–477 (1991).
97. A. Weiner, R. Thurston, W. Tomlinson, J. Heritage, D. Leaird, E. Kirschner, and R. Hawkins, "Temporal and spectral self-shifts of dark optical solitons," *Opt. Lett.* **14**, 868–870 (1989).
98. W. Zhao and E. Bourkoff, "Generation, propagation, and amplification of dark solitons," *J. Opt. Soc. Am. B* **9**, 1134–1144 (1992).
99. K. Park, H. Kim, H. Chang, and Y. Jeong, "Incoherent Supercontinuum Light Source via an Active Highly-Nonlinear Photonic Crystal Fiber with All-Normal Dispersion for Laser-Based Sensing Applications," in *Fourier Transform Spectroscopy*, (Optical Society of America, 2019), JW3A. 9.
100. P. D. Drummond and M. Hillery, *The quantum theory of nonlinear optics* (Cambridge University Press, 2014).

101. S. Lee, L. A. Vazquez-Zuniga, H. Kim, Y. Kwon, K. Park, H. Kim, and Y. Jeong, "Experimental spatio-temporal analysis on the shot-to-shot coherence and wave-packet formation in quasi-mode-locked regimes in an anomalous dispersion fiber ring cavity," *Opt. Express* **25**, 28385–28397 (2017).
102. W. J. Brown, S. Kim, and A. Wax, "Noise characterization of supercontinuum sources for low-coherence interferometry applications," *J. Opt. Soc. Am. A* **31**, 2703–2710 (2014).
103. C. Amiot, P. Ryczkowski, A. T. Friberg, J. M. Dudley, and G. Genty, "Supercontinuum spectral-domain ghost imaging," *Opt. Lett.* **43**, 5025–5028 (2018).
104. S. Demmler, J. Rothhardt, A. M. Heidt, A. Hartung, E. G. Rohwer, H. Bartelt, J. Limpert, and A. Tünnermann, "Generation of high quality, 1.3 cycle pulses by active phase control of an octave spanning supercontinuum," *Opt. Express* **19**, 20151–20158 (2011).

# 국 문 초 록

## 광학적 이득이 포함된 비선형 매질에서의 초연속체 광원 생성과 비선형 펄스 역학에 대한 이론적 연구

서울대학교 대학원  
전기정보공학부  
박 경 윤

본 논문에서, 광학적 이득이 포함된 고-비선형 광 결정 광섬유에서의 초연속체 생성과 관련된 솔리톤 역학을 수치적 및 이론적으로 분석하였다. 특히, 고-비선형 광 결정 광섬유의 전-정상 분산 및 비정상 분산에서의 밝은 솔리톤과 어두운 솔리톤 역학 현상을 조사하였고, 이러한 솔리톤 역학이 초연속체 생성에 미치는 영향을 자세히 분석하였다.

논문의 첫 번째 챕터에서는, 광섬유 광학과 광섬유 레이저, 그리고 광학적 솔리톤 및 초연속체 생성과 같은 비선형 광학 현상을 개괄적으로 소개하였다. 이어 두 번째 챕터에서는, 초고속 광 펄스와 이득 이온 사이의 초고속 상호 작용을 수치적으로 모델링하였다. 특히, 초고속 광 펄스가 겪는 비선형 광학 현상은 비선형 슈뢰딩거 방정식으로 모델링하였으며, 웨토 초 영역에서 이득 이온과 광 펄스의 빠른 상호작용을 모델링하기 위하여 멕스웰-블로흐 방정식을 유도하였다.

특히, 광섬유에 도핑이 되는 이온인 어븀 그리고 이터븀에 대한 맥스웰-블로흐 방정식을 각각 유도하였다. 또한, 일정한 주기를 가지고 반복적으로 입력이 되는 펄스에 의한 이득 이온의 이득 포화 작용을 맥스웰-블로흐 방정식으로부터 유도하여, 해당 작용을 유효 포화 에너지라는 단일 상수로 표현하였다. 이는 세 번째 챕터에서 맥스웰-블로흐 방정식과 비선형 슈뢰딩거 방정식을 결합시키는 열쇠가 된다.

세 번째 챕터에서는, 초고속 광 펄스와 광학적 이득의 상호작용에 의한 초연속체 현상을 모델링하고, 광학적 이득이 초연속체 및 솔리톤 역학에 미치는 영향을 조사하였다. 일반적으로 실제로 피코 초 펄스와 이득 이온의 상호 작용은 종종 잘 알려진 비율식 (rate equation)과 비선형 슈뢰딩거 방정식으로 모델링 되지만, 비정상 분산 영역에서 초연속체 생성 과정 중에 필연적으로 발생하는 100-fs 이하 초고속 펄스와 이득 이온의 상호 작용은 비율식으로 모델링 될 수 없다. 따라서, 본 논문에서는 두 번째 챕터에서 유도한 이터븀 이온에서의 맥스웰-블로흐 방정식과 비선형 슈뢰딩거 방정식을 결합한, 일반화된 긴즈버그-란다우 방정식 모델을 사용하였다. 긴즈버그-란다우 방정식에 기초하여, 피코 초 미만 펄스 영역에서 비정상 분산을 갖는 활동성 광결정 광섬유에서의 초연속체 생성을 수치해석적으로 조사하였다. 이득 효과는 ‘단계적 솔리톤 방출’, ‘솔리톤-준솔리톤 충돌’, 및 ‘고주파수의 분산광 생성’과 같은, 수동성 광결정 광섬유의 초연속체에서 발견되지 않은 새로운 솔리톤 역학 현상을 야기하였다. 이득에 의해 새로이 발현된 솔리톤 역학은, 초연속체가 평탄성을 잃지 않고 광대역 스펙트럼 성분이 균등하게 증폭시키는데 기여한다.

논문의 네 번째 챕터에서는, 전-정상 분산의 특성을 갖는 이득 광결정 광섬유에서의 초연속체 생성을 분석하였다. 일반적으로 전-정상

분산의 조건에서는 어두운 솔리톤이 자발적으로 생기지 않는다. 하지만, 일정 임계점 이상의 높은 이득을 인가한다면, 자발적으로 어두운 솔리톤이 생성될 수 있다는 사실을 본 수치 해석을 통해 확인하였다. 이득 및 라만 산란 파라미터를 조절하며 비교적 수치 해석을 수행한 결과, 어두운 솔리톤은 광학적 이득과 라만 산란이 동시에 존재하는 경우에만 생성된다는 사실을 확인했다. 높은 광학적 이득은 펠스의 첨두 출력을 상승시키고, 상승된 첨두 출력은 자기-위상 변조에 의해 생성된 청-주파수 쪽 첨두 스펙트럼 파워를 상승시킨다. 첨두 스펙트럼 파워가 일정 문턱 값을 넘어서게 된다면, 청-주파수 첨두 스펙트럼으로부터 라만-유도 진동 구조 (RIOS)가 발생한다. 발생한 RIOS는 시간이 지남에 따라 점점 더 증폭되며, 진동 구조로부터 어두운 솔리톤이 발생한다. 이러한 어두운 솔리톤은 서로 반발적으로 충돌하며 복잡한 역학적 양상을 보인다. 이러한 복잡한 어두운 솔리톤 역학은 초연속체 스펙트럼의 대역폭 및 간섭성에 영향을 준다. 어두운 솔리톤에 의해 초연속체 스펙트럼의 간섭성은 점진적으로 감소하며, 동시에 적-주파수 한계선 너머로 추가적인 스펙트럼의 확장이 발생한다. 이는 곧 펌프 파워와 같은 광학적 이득 파라미터를 조절함으로써 초연속체의 대역폭, 파워, 그리고 간섭성을 조절할 수 있음을 의미한다. 이는 파워 및 간섭성-제어 가능한 초연속체 생성 시스템 개발의 핵심 원리로 적용될 수 있다.

결론적으로, 광학적 이득이 포함된 광 결정 광섬유에서 초연속체를 생성할 때, 광학적 이득을 조절함으로써 초연속체의 파워 스케일링을 할 수 있으며, 동시에 대역폭 및 간섭성 특성을 제어할 수 있다는 사실을 본 연구를 통해 규명하였다. 이는 곧 입력 초연속체의 특성을 조절할 수 있는 기존의 파라미터인 펠스 폭과 첨두 출력 이외에 펌프 파워라는

추가적인 제어 파라미터의 획득을 의미한다. 펄스 폭이나 첨두 출력을 증가시키면 초연속체 스펙트럼의 파워보다는 대역폭이 증가하는 경향이 컸던 반면, 이득을 증가시키면 스펙트럼의 대역폭보다는 파워가 증가하는 경향이 크기 때문에 초연속체의 파워 스케일링에 용이하다. 이에 더하여, 전-정상 분산 영역에서는 이득에 따라 shot-to-shot 간섭성이 달라지기 때문에, 단순히 펌프 파워만을 조절하여 저-간섭성에서부터 고-간섭성 초연속체 광원을 모두 생성할 수 있다. 따라서, 본 연구의 결과는 다양한 광 응용 분야에서 요구하는 특성의 초연속체 광원을 맞춤형으로 생성할 수 있는 종합적 초연속체 광원 생성 시스템 개발의 기반 원리로서 응용될 수 있다. 또한, 본 연구에서 관찰된 솔리톤 역학은 기존의 닫힌 계 솔리톤 역학이 아닌 에너지가 출입하는 열린 계에서의 솔리톤 역학으로, 닫힌 계에서는 볼 수 없었던 흥미로운 현상들이 다수 관찰되었다. 열린 계에서의 집단적 솔리톤 상호작용은 아직 활발히 연구되지 않은 새로운 비선형 광학 연구 분야이다. 이에, 본 논문을 통해 보고되는 연구 성과가 앞으로 이득이 결합된 비선형 매질에서의 솔리톤 역학 및 응용에 관한 후속 연구에 도움이 될 것을 희망한다.

**키워드:** 광섬유 레이저, 비선형 광섬유 광학, 광학적 솔리톤, 초연속체, 극초단 펄스 광학, 양자광학

**학번:** 2013-20789

# 감사의 글

본 학위 논문의 작성에 도움을 주신 분들께 감사의 인사를 전합니다.

정윤찬 지도교수님께 먼저 감사의 말씀을 전합니다. 그 동안 지도교수님을 통해 많은 것을 보고 배웠습니다. 그 중에서도 가장 가슴 깊게 남은 것은, 포기하지 않는 끈기와 스스로 만족할 때까지 정성을 다하는 지도교수님의 연구자로서의 자세입니다. 이는 박사 과정에서 얻은 가장 큰 자산 중 하나라고 생각합니다. 그리고 영국 사우스햄프턴 파견 연구와 다수의 국제 학회 참석 등, 견문을 넓힐 수 있는 많은 기회를 만들어 주셨습니다. 마지막으로, 광섬유 레이저 및 비선형 광학이라는 흥미로운 연구 분야로 저를 이끌어 주시고 연구에 대해 아낌없이 조언해주신 점에 깊이 감사드립니다.

박사 논문 심사의 심사위원으로 참석해주시고 아낌없이 조언해주신 이병호 교수님, 박남규 교수님, 그리고 홍용택 교수님께 감사드립니다. 그리고 심사를 위해 새벽부터 먼 길을 달려와 주신 김현태 교수님께 감사드립니다.

Luis Alonso Vazquez-Zuniga, 김현태, 이승종, 권영철, 김진섭, 홍승수, 조훈민, 이동영, 정병선 선배님에게 감사의 인사를 전합니다. 선배님들의 아낌없는 도움과 조언, 그리고 선배님들이 이루어 놓으신 연구 성과 덕분에 본 학위 논문이 쓰일 수 있었습니다. 뛰어난 학식으로 연구에 대해 함께 논의해준, 이동열, 김한솔, 안해찬, 나정균에게 감사드립니다. 그리고, 부족한 선배를 잘 따라주었던 한민곤, 장한별, 이승수, 손장원, 김주환, 강현구, 양혁진, 여민수, 김병호, 이채영, 차혜선 후배님에게도 감사를 전합니다.

박산성, 정연수, 한상도, 김동영, 이준호, 안진엽, 서정윤, 이원지를

포함한 포항공과대학교 08학번 2분반 동기들, 권영흠, 박찬영을 비롯한 포항공과대학교 SLEST 후배들, 이준수, 김종원, 조규원, 배상집을 비롯한 울산 신정고등학교 친구들, 그리고 어느덧 18년 지기의 해바라기 모임의 친구들, 구영모, 권익환, 김도연, 성기완에게도 감사의 말씀을 전합니다. 소중한 친구와의 대화를 통해 새로운 관점과 지혜를 얻을 때도 있었으며, 그대들의 진심 어린 조언에 많은 위로를 받았습니다.

저를 양자광학과 레이저의 길로 인도해주시고, 학문과 지식을 사랑하는 학자의 열정을 몸소 보여주신 포항공과대학교 권오대 명예교수님, 저를 늘 아껴 주셨던 조경숙 은사님, 그리고 저에게 많은 기회를 주셨던 많은 선생님들에게도 감사의 뜻을 전합니다.

마지막으로, 누구보다 가까이에서 부족한 저를 믿어주고 아껴준 어머니, 동생 박경모, 할머니, 그리고 소중한 연인 강나영에게 깊은 감사의 뜻을 전하고자 합니다. 어머니, 홀로 가정을 이끌어 가기 위해 쉬는 날 하루 없이 이른 아침부터 늦은 밤까지 홀로 일하신지 16년이 넘어갑니다. 못 가정에서는 일찍 취직을 권유할 수도 있을 법한 가정 형편에서도, 어머니께서는 걱정되는 마음을 견디시며 원하는 공부를 더 하고 싶다는 저의 어리광과 같은 바람을 지지해 주셨습니다. 사랑하는 동생 박경모, 형제일 뿐만 아니라 삶에서 소중한 친구이며 상담자로서 늘 함께 해주어 고맙습니다. 형이 공부하느라 늘 울산 밖에 있을 동안, 어머니 곁에서 일을 묵묵히 도와주었기에 형이 공부를 이어갈 수 있었습니다. 오늘의 박사 학위는 어머니와 동생의 헌신이 없었으면 불가능했을 것입니다. 하늘에 계시는 아버지께서도 우리 가족을 자랑스러워 하시리라 생각이 듭니다. 그리고, 박사 학위를 준비하였던 지난 3년 동안 늘 곁에서 응원해주고, 기쁜 날에는 나보다 더

기뻐해 주고, 지친 날에는 따뜻하게 위로해 준 연인 강나영에게 사랑하는 마음을 담아 감사의 뜻을 전합니다.

감사의 글에 전부 신지는 못했지만 수 많은 분들의 도움으로 본 학위 논문이 마무리될 수 있었습니다. 이 모든 분들의 평온을 기도하며, 라인홀트 니버의 ‘평온을 비는 기도’를 인용하면서 감사의 글을 마칩니다.

*“God, give us grace to accept with serenity the things that cannot be changed,  
courage to change the things that should be changed,  
and the wisdom to distinguish the one from the other.”*

-2020년 2월, 박경운 올림